Title
Multimodal Assessment of Structure and Function in Inherited Retinal Degenerations

Author
Foote, Katharina

Publication Date
2019

Peer reviewed|Thesis/dissertation

Multimodal Assessment of Structure and Function in Inherited Retinal Degenerations

By

Katharina Gwinear Foote

A dissertation submitted in partial satisfaction of the

requirements for the degree of

Doctor of Philosophy

in

Vision Science

in the

Graduate Division

of the

University of California, Berkeley

Committee in charge:

Professor Austin Roorda, Chair
Professor Susana Chung
Professor David Schaffer

Summer 2019

Multimodal Assessment of Structure and Function in Inherited Retinal Degenerations

by Katharina Gwinear Foote

Abstract
Multimodal Assessment of Structure and Function in Inherited Retinal Degenerations
by
Katharina Gwinear Foote
Doctor of Philosophy in Vision Science
University of California, Berkeley
Professor Austin Roorda, Chair

Inherited retinal degenerations (IRDs) affect approximately 1:4,000 people worldwide and are currently the leading cause of vision loss of people between the ages of 15-45. The mechanisms of degeneration in many IRDs remain unclear. It is vital to establish relationships between retinal structural and functional measures in order to better understand the relationship between the genetic mutations and the phenotypes they cause in these diseases. For example, retinitis pigmentosa (RP), the most prevalent IRD, and choroideremia (CHM), an X-linked degeneration that affects choroidal, RPE and photoreceptor cells, both progress over time due to rod, then cone, photoreceptor loss. Greater understanding of disease progression may clarify the underlying mechanisms of retinal degenerations. Furthermore, the development of novel outcome measures could accelerate clinical trials of treatments designed to treat these relentless, sight-threatening diseases. The experiments and research described in this document use multimodal state-of-the-art, novel, high-resolution techniques in addition to standard technologies used in the clinical setting to study the relationship between structure and function of the retina including rod and cone photoreceptors, retinal pigment epithelium, choriocapillaris and other retinal layers affected in the eyes of patients with retinal degeneration.

Table of Contents

List of Figures

Chapter 1

Chapter 2

Chapter 3

Chapter 4

Chapter 5

List of Tables

Chapter 1

Chapter 2

Chapter 3

Chapter 4

Chapter 5

List of Abbreviations

ACHM	Achromatopsia
AD	Autosomal dominant
AO	Adaptive optics
AOM	Acousto-optic modulator
AOMP	Adaptive optics microperimetry
AOSLO	Adaptive optics scanning laser ophthalmoscopy
AR	Autosomal recessive
Arcmin	Arcminutes
BCVA	Best-corrected visual acuity
BM	Bruch's membrane
CC	Choriocapillaris
CD	Cone dystrophy
Cd/m^2	Candela per square meter
CHM	Choroideremia
CI	Confidence interval
CRD	Cone-rod dystrophy
CSNB	Congenital stationary night blindness
CV	Choroidal vessels
dB	Decibel
DS	Diopter sphere
DVA	Decreased visual acuity
ELM	External limiting membrane
ETDRS	Early Treatment of Diabetic Retinopathy Study
EZ	Ellipsoid zone
FAF	Fundus autofluorescence
FDA	Food and Drug Administration
FPS	Frames per second
FV	Flow void
GCL	Ganglion cell layer
ICC	Interclass correlation coefficient
ILM	Internal limiting membrane
INL	Inner nuclear layer
IPL	Inner plexiform layer
iPSCs	Induced pluripotent stem cells
IR	Infrared
IRD	Inherited retinal degeneration
IS	Inner segment
IS/OS	Inner segment/outer segment junction
IZ	Interdigitation zone
LCA	Leber congenital amaruosis
LCD	Liquid crystal display
LE	Left eye
MAR	Mean angle of resolution

MP1	Microperimeter
NB	Night blindness
NIR	Near-infrared
NIR-AF	Near-infrared autofluorescence
NIR-REF	Near-infrared reflectance
OCT	Optical coherence tomography
OCTA	Optical coherence tomography angiography
ONL	Outer nuclear layer
OPL	Outer plexiform layer
OS	Outer segment
PMT	Photo-multiplier tube
PRL	Preferred retinal locus
PSF	Point spread function
RD	Retinal degeneration
RE	Right eye
REP-1	Rab escort protein-1
RGC	Retinal ganglion cell
RHO	Rhodopsin
RNFL	Retinal nerve fiber layer
ROI	Region of interest
RP	Retinitis pigmentosa
RPE	Retinal pigment epithelium
RPGR	Retinitis pigmentosa GTPase regulator
RVF	Reduced visual field
SD	Standard deviation
SD-OCT	Spectral domain-optical coherence tomography
SE	Study eye
SITA	Swedish interactive threshold algorithm
SLO	Scanning laser ophthalmoscopy
S-MAIA	Scotopic – Macular Integrity Assessment
SS-OCT	Swept-source optical coherence tomography
STGD1	Stargardt disease
SW-AF	Short-wavelength autofluorescence
Td	Trolands
USH2A	Usherin
VA	Visual acuity
WFS	Wavefront sensor
XL	X-linked

Acknowledgements

The efforts in this work would not have been possible without the support and collaboration of numerous individuals. It is with profound gratitude that I experienced a graduate education with not only one mentor, but two. I am exceptionally grateful to have had the opportunity to work under the mentorship of Austin Roorda, who provided immeasurable support to all of my projects, and ultimately, manuscripts. I am equally indebted to Jacque Duncan, who supported, encouraged, and guided me through the rigor and joy of clinical research. Dr. Duncan not only enlightened me to a world of excellence in translational work, but also to a stature of everlasting enthusiasm and passion for applied research that encourages me every day.

The Roorda lab members were exceedingly helpful and I recognize and thank them for their collaboration and support; Ram Sabesan, Will Tuten, Kavitha Ratnam, Ally Boehm, Brian Schmidt, Sanam Mozaffari, Ethan Bensinger, Francesco LaRocca, Volker Jaedicke, and Yiyi Wang. I am also grateful to the Duncan team, who helped greatly with all of my projects; Panagiota Loumou, Mary Lew, Arshia Mian, Tom Hernandez, Travis Porco, Nic Rinella, Janette Tang, and Jessica Wong. A special thank you - to Nicolas Bensaid and Swati Bhargava who worked tirelessly to improve the imaging system used to conduct a majority of the work in this document. And, a colossal thank you - to Pavan Tiruveedhula, for his endless technical software and hardware support, and for an uplifting and patient presence in the lab.

I am extremely appreciative of my qualifying exam committee who took the time to facilitate the shape of the projects in this dissertation, and provide expert feedback; Susana Chung, John Flannery, Christine Wildsoet, and David Schaffer.

Chapter 4 of this document would not have been possible without the collaborative efforts of the Wang Lab. I am especially thankful to Ruikang Wang, Qinqin Zhang, and Hao Zhou for all of their diligence and assistance with image processing and analysis.

Prior to graduate school, I was fortunate to study under the mentorship of Jay Neitz and Maureen Neitz, who introduced me to human and non-human primate research. I would not be here today without their support, advice, and encouragement to pursue a graduate degree. In addition, my very first mentor in vision science necessitates infinite thanks - Steve Buck, who acquainted me with the intricacies of color psychophysics, experimentation, and insight to the world.

Finally, none of this would be attainable without the support and encouragement from my friends and family close and afar. I thank my parents, who spurred on an early interest in scientific experimentation with the sensory systems. I am grateful to Esther; sister, friend, and mentor, for always being present, understanding, and for lighting the road ahead. And lastly, to Andrea, who taught me love, language, and perseverance.

CHAPTER 1: Introduction

1.1 Optics and anatomy of the eye

The eye is one of the most vital sensory organs. An intricate system, the eye relies on the correct genetic code to express functional proteins in ocular structures and to provide a complete visual experience. When there is light in the environment, photons enter the eye. The photons first pass through the cornea, a transparent tissue which contributes two thirds of the total refractive power of the eye. From the cornea, light enters through the pupil, the aperture controlled by the iris, which is made up of smooth muscle which contracts and dilates to control the pupil size and maximize light delivery based on environmental conditions. Light then passes through the pupil to the crystalline lens, a fibrous, flexible structure, which contributes the remaining one third of refractive power. The pupil (as well as eye irregularities or aberrations), governs the depth of focus. The ciliary muscles control the lens shape and dictate the focusing power of the lens, thereby regulating its accommodation, or position of best focus.

This mechanism allows the eye to see near and far; specifically, the ciliary body pulls or pushes on the lens to make it more or less curved, changing how much the light bends. Assuming the eye is emmetropic (having no refractive error), the relaxed lens will focus light to the back of the eye onto the retina, where images appear sharp and clear. If the eye is too short (hyperopic) or too long (myopic), or the lens power is too small or large, refractive lenses can be used to focus the light correctly onto the retina (Kolb 2007).

Once light reaches the retina, it passes first through the transparent layers of neural tissue which serve to eventually transport signals to the brain. But first, the light stimulates the rod and cone photoreceptors, the light sensing cells of the eye. The retinal pigment epithelium (RPE) layer acts to support and nourish the adjacent photoreceptor cells and to transport metabolic waste from the photoreceptors across the support structure, Bruch's membrane, to the choroid. Directly adjoining Bruch's membrane, the choriocapillaris resides as a vascular network of fenestrated capillaries, and fundamental component of the retina's metabolism.

Santiago Ramón y Cajal (1852 – 1934), pathologist, histologist, Nobel laureate, and father of neuroscience, pioneered investigations of brain structures including the retina (Figure 1.1) and created hundreds of skilled illustrations that still function today as educational tools. Figure 1.1 depicts an early sketch from Cajal that shows the intricacies of the retinal layers, highlighting the rods and cones, and their differing shapes.

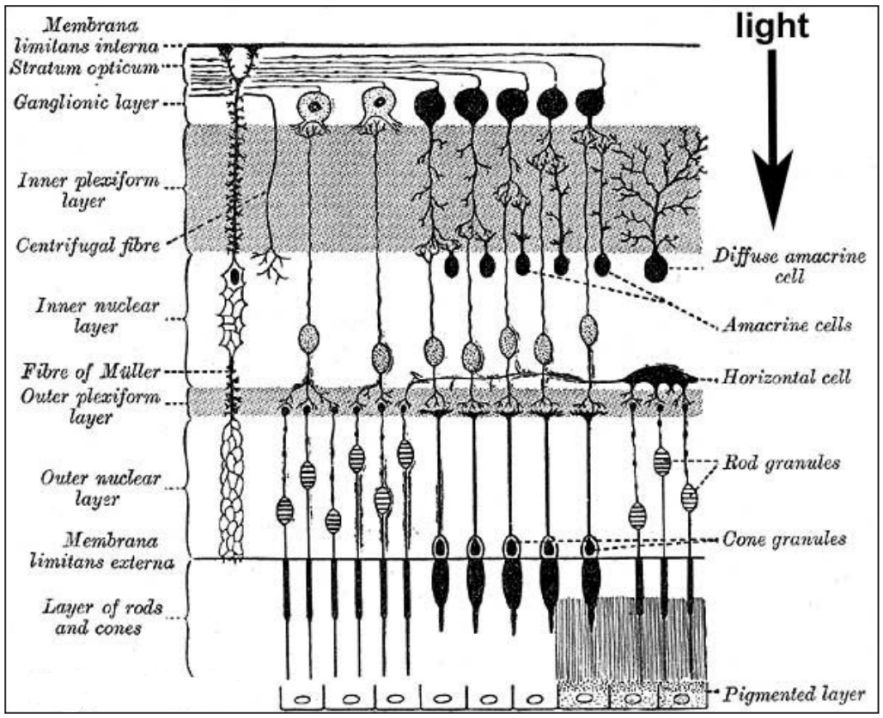

Figure 1.1. Historic illustration by Ramón y Cajal, depicting the structure of the retina, showing the pathway from light entering from above, through all the retinal layers (image available at https://nei.nih.gov/intramural/lrcmb/LRCMB_image).

Light focuses particularly onto the fovea, the center of the field of vision where acuity is best, and cones are the densest. The average healthy retina is composed of about 4.6 million cones and 92 million rods. Highest cone density is found close to the center of the fovea, and falls off with increasing eccentricity. There exists a rod-free zone of 1.25 degrees (0.35 mm) horizontal diameter, and rod density peaks at ~18 degrees eccentricity (Curcio et al., 1990, Kolb 2012). The rod cells serve scotopic vision, to allow for vision in dimly lit conditions, while the cones provide photopic vision in high light levels to provide color vision and high acuity vision (Lamb 2016).

Degeneration of the RPE, choriocapillaris, and most of all, the photoreceptors causes vision loss and over time. In rod-cone degenerations, the rods are the cells primarily affected, causing patients to experience night blindness and mid-peripheral visual field loss, followed by tunnel vision due to rod loss in the mid-periphery. Later, cones degenerate as well, followed by degeneration of RPE and choroidal vessels.

1.2 Inherited retinal degenerations

Inherited retinal degenerations (IRDs) are the leading cause of vision loss in developed countries, and all together have an estimated prevalence of 1:4000 (Hartong et al., 2006; Cremers et al., 2018). IRDs are caused by mutations in over 270 identified genes (RetNet. available at: https://sph.uth.edu/retnet/ Accessed July 5, 2019). IRDs represent a

heterogeneous group of diseases (Figure 1.2) that can cause relentless, progressive, photoreceptor cell death, leading to debilitating vision loss and blindness as a result of genetic mutations (Duncan et al., 2018). IRDs include stationary forms, such as congenital stationary night blindness (CSNB) and achromatopsia (ACHM), and progressive forms, including retinitis pigmentosa (RP), cone-rod dystrophy (CRD), Stargardt disease (STGD1), and choroideremia (CHM). IRDs are further classified as having primarily dysfunctional rods or cones, and many of them overlap, affecting both rods and cones. Depending on the mutation type and the affected gene, the rate of degeneration can be different. In general, in RP and CHM, rods degenerate first, followed by cones; and in CRD and STGD1, the reverse pattern occurs. If a patient is diagnosed late in the disease process, a clear diagnosis based on symptoms can be difficult, due to both rod and cone death. CHM is caused by mutations in a single gene, *CHM*. Most IRDs however, have many different genes with many different mutations all causing relatively similar phenotypes. Leber congenital amaurosis (LCA), is a severe, early onset IRD in which the cones, rods and retinal pigment epithelium (RPE) all degenerate to different degrees depending on the responsible gene.

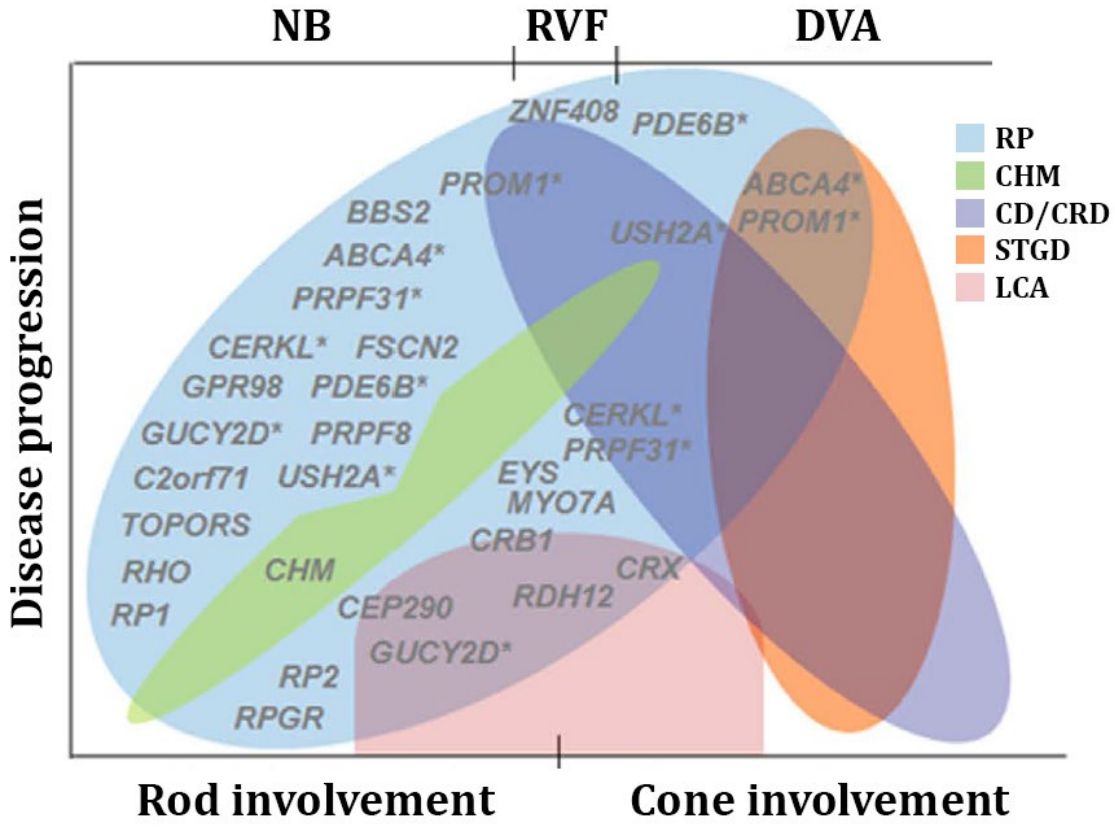

Figure 1.2. Breakdown of genotyope-phenotype correlations. Color coded overlapping phenotypes show different forms of nonsyndromic IRD: RP (Retinitis pigmentosa), CHM (Choroideremia), CD/CRD (Cone dystrophy/Cone-rod dystrophy), STGD (Stargardt disease) and LCA (Leber congenital amaurosis). Phenotypes and primary symptom displayed according to gene name positions (NB: Night blindness; RVF: Reduced visual field; DVA:

Decreased visual acuity). * indicate genes represented > 1 time due to the high heterogeneity. (Adapted from Figure 2A of Bravo-Gil et al., 2017, page 5).

Treatment development has been limited to date in altering disease progression. Only few treatments involving neurotrophic factor therapy and gene therapy (Berson et al., 1993; Berson et al., 2004; Edwards et al., 2016; MacLaren et al., 2014) have shown safety and modest efficacy. In 2017, the first specific gene replacement therapy, for degeneration associated with biallelic *RPE65* mutations (Russell et al., 2017), was approved by the US Food and Drug Administration (FDA) (Bennett et al., 2016; Cideciyan et al., 2008; Jacobson et al., 2012; Weleber et al., 2016). Phase 1 and 2 studies of gene replacement for patients with mutations in the *CHM* gene which cause choroideremia, a progressive degeneration (Edwards et al., 2016) have shown great promise and suggest that similar techniques could be used to treat other forms of IRD besides *RPE65* –related retinal degeneration (Hohman 2017).

This dissertation focuses on RP and CHM. RP, the most common IRD (Zhang 2016), refers to a heterogeneous group of inherited diseases ensuing from mutations in at least 87 genes identified so far (https://www.omim.org/phenotypicSeries/PS268000) causing progressive and relentless vision loss due to degeneration of rods, then cones. RP can be transmitted by autosomal dominant (30%–40%), autosomal recessive (50%–60%), or X-linked (5%–15%) inheritance (Hartong et al., 2006; Zhang 2016). RP mostly presents with no other systemic diseases other than the affected ocular condition.

RP is the leading cause of hereditary blindness in developed nations, and it has worldwide prevalence of 1:4,000, although this may be an underestimation for individual populations (Zhang 2016). RP presents first with symptoms of night blindness and constricted peripheral visual fields. As the disease progresses, patients experience reduced visual acuity and eventual blindness because the rod and cone photoreceptor cells die.

There is variable disease expression in patients with different mutations in the same gene, and even in patients within the same family. Nevertheless, there are general characteristic changes to the fundus, most prominently, bone spicule pigmentary change in the midperiphery due to loss of photoreceptors, pigment clumping, and migration of the RPE cells into the retina (Zhang 2016). Retinal vessel attenuation is thought to be due to a reduction of metabolic demand from ganglion cell death following photoreceptor death (Verbakel et al., 2018), possibly from a reduction or lack of tropic factors resulting from photoreceptor death, leading to inner retinal layer reduced metabolism (Stone et al., 1992). Alternately, it could be due to the loss of the photoreceptors themselves, who when alive, consume oxygen, and whose death could lead the inner retina to be in a hyperoxic state, causing vasoconstriction and reduced retinal vessel blood flow (Grunwald et al., 1996; Padnick-Silver et al., 2006; Penn et al., 2000; Yu and Cringle, 2005). The other main presentation of RP as the disease progresses is a waxy pallor of the optic disc, caused likely from glial cell formation in and around the optic disc, causing increased reflectance of light (Hwang et al., 2012; Szamier, 1981).

Given the variability in disease progression even in patients with the same mutation type, and the association of both rod and cone photoreceptor death, RP is an important disease to investigate. Since there is not one established machine that has every capability, a multimodal approach is needed, ideally imaging rods and cones since they are the cells primarily affected. Therefore, the main objective of the current work is to better understand the structure/function and genotype/phenotype relationship in IRDs by measuring loss of rod and cone photoreceptors.

CHM has an estimated prevalence of 1:50,000 (Sahel et al., 2015) and is caused by mutations affecting the single CHM gene which encodes for the Rab Escort Protein-1, REP-1 on chromosome Xq 21.2 (Cremers et a., 1990). REP-1 is typically thought to be involved in regulation of proteins affecting phagocytosis, intracellular trafficking, and organelle formation (Coussa et al., 2012). The exact disease mechanism has not yet been fully elucidated, but recent evidence suggests REP-1 to have a systemic role in fatty acid metabolism, however how this affects the retina is still unknown (Aleman et al., 2017; Zhang et al., 2015).

Since CHM is X-linked (XL) recessive in inheritance, an affected male will transmit the pathogenic variant to female offspring, but not to male offspring. Carrier females have a fifty percent chance of transmitting the pathogenic variant to offspring; male offspring would be affected, females would likely be carriers and usually unaffected. Thus, since CHM is inherited in an XL manner, it most typically affects males, although symptomatic females have been described (Syed et al., 2013). Similar to RP, CHM presents with night blindness, and peripheral visual field loss, often in the second decade of life.

However, in patients with CHM, central vision often remains preserved until late in life. CHM has a characteristic scalloped mid-peripheral chorioretinal degeneration (MacDonald et al., 2015). These patchy areas progress further to greater depigmentation or loss of the RPE and choriocapillaris. Yet, deeper choroidal vessels often remain preserved.

1.3 Adaptive optics scanning laser ophthalmoscopy

The eye, even a healthy, emmetropic eye, is not a perfectly shaped sphere. On the contrary, it has many imperfections, particularly the main optical surfaces of the eye; the lens and the cornea. Hermann von Helmholtz (1821-1894), a famous physician and physicist who made significant contributions in many fields, including vision science, first described imperfections or aberrations of the eye (Helmholtz, 1924). There are numerous aberrations in the eye and the optics are not ideal, nevertheless, sight occurs, and part of this is due to the circuitry of the retina, neural tissues, cortex, and eye movements which compensate for the many optical imperfections. To the natural eye, lower order aberrations can be corrected for with a refractive lens. However, higher order aberrations, while not noticeable in daily life, are present in even emmetropic eyes, and are noticeable during high resolution imaging. When imaging the eye, in general these imperfections, or aberrations cause decreased image quality.

In order to overcome this limitation, Adaptive Optics Scanning Laser Ophthalmoscopy (AOSLO) was adapted from its use in astronomy where was first used to view stars and galaxies through the aberrations of the atmosphere (Beckers 1993). In the eye, AOSLO overcomes shortcomings of the uncorrected eye, by measuring and compensating for aberrations (Roorda et al., 2002). The AOSLO system uses a supercontinnum laser with bandpass filters in order to provide a multiwavelength output. AOSLO makes use of a wavefront sensor (WFS), often of 910 nm or another infrared (IR) wavelength to measure optical aberrations, and uses adaptive optics (AO) via a deformable mirror to compensate and correct for the aberrations. Image resolution increases with increasing system apertures, but as a pupil increases in size, as do the aberrations from increasing light scatter. As the beam diameter of light from an optical system increases, the point spread function (PSF), halo response of an imaging system to a point of light, also expands. Thus, ocular aberrations expand the PSF, causing a reduction in resolution. Although the correction ability of AO varies depending on the eye, overall optimal resolution is gained through AO which forces the PSF to concentrate to a small enough point (Zhang and Roorda 2006).

By using a multiwavelength AOSLO, it becomes possible to confine a stimulus probe of one wavelength (for example, 543 nm, which would equally stimulate L and M cones) and target the stimulus to desired locations on the retina (Harmening et al., 2014). Imaging eyes with an infrared light source (840 nm), the returning light is then guided to a confocal pinhole, collected continuously into a photo-multiplier tube (PMT), and extracted into a live video stream. A combination of the PMT's voltage output and the signals from the scanning mirrors is used to render a live 512 x 512 pixel video with an acquisition rate of 30 frames per second (FPS). In real time, by registering the video stream to a chosen reference image, and by using a strip based cross correlation method (Arathorn et al., 2007), image stabilization can occur. From there, an acousto-optic modulator (AOM) is used to control when stimuli would be projected to the retina pixel-by-pixel by modulating the raster scan with its high-speed switch. The axial resolution of the system is approximately 2.5 μm lateral and <100 μm axial (Roorda et al., 2002).

The field of high resolution imaging continues to advance, and the combination of high-resolution eye tracking with adaptive optics has allowed for the capability to compensate for natural eye movements (Arathorn et al., 2007; Harmening et al., 2014). This technological advance opened up the field to allow for the stimulation of individual cones repeatedly and track them over days, months, and years, which has many applications from testing color perception (Schmidt et al., 2018), to tracking cone photoreceptors in patients with retinal disease over time (Scoles et al., 2017). In other words, stimuli can be delivered onto a stabilized retina with accuracy of about 0.26 arcmin (1.3 μm) (Arathorn et al., 2007), in order to test retinal function with high accuracy.

AOSLO is the most well suited non-invasive technology to deploy in order to visualize photoreceptors in vivo. AOSLO is capable of yielding images of cone photoreceptors characterized by light waveguided by intact inner and outer segments in contact with RPE cells (Choi et al., 2006; Duncan et al., 2007; Rha et al., 2010; Wolfing et al., 2006; Miller et al., 1996). Furthermore, AOLSO technology has progressed to not only being able to image confocal light scattered from wave-guiding outer segments of photoreceptors, but also able

to capture nonconfocal split-detector light revealing photoreceptor inner segments (Scoles et al., 2014). This development has potential to improve identification of remnant photoreceptors that might be amenable to therapeutic intervention in clinical trials.

Non-confocal split detection capacity allows the scattered light from cone inner segments to be observed even if there is no intact outer segment. Both confocal and non-confocal split detection imaging can be acquired simultaneously, in order to visualize the backscatter of wave guided light from the outer segments and inner segments of cones respectively.

This ability to use a combination confocal/nonconfocal system becomes particularly important when imaging outside of the central fovea. Beyond the fovea, the distribution of rods increases, and rods appear interspersed with the cones, make it hard to distinguish the cones in images (Curcio et al., 1990). Therefore, using split detector imaging in combination with confocal imaging helps to disambiguate the cones and rods from non-waveguiding structures (Sun et al., 2016). Figure 1.3 shows the combination system at UCSF.

Quantification of AOSLO structure is discussed in Chapters 2-5 and is typically performed through cone counting, either with cone spacing or cone density measures (Cooper et al., 2016). When cones are more ambiguous in AOSLO images, cone spacing (Duncan et al., 2007) is typically deployed. However, if all cones in a region of interest (ROI) are present, cone density is a reliable method to use (Cooper et al., 2016).

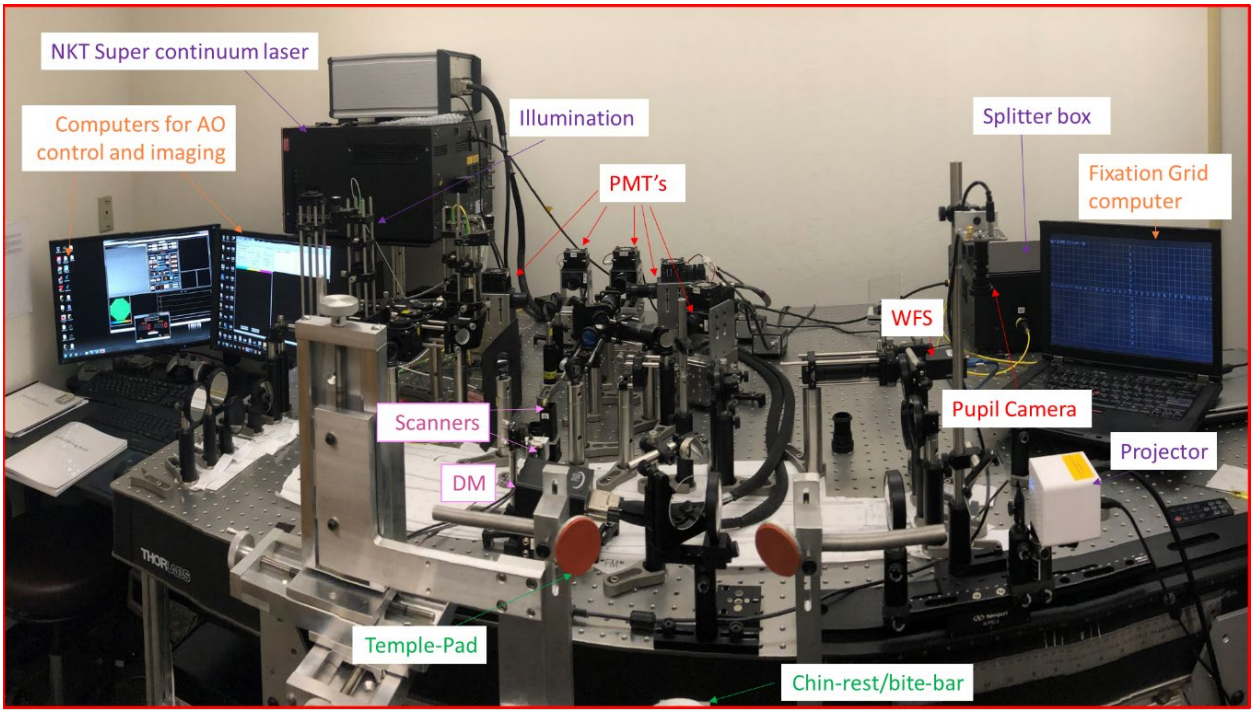

Figure 1.3. AOSLO system at the University of California, San Francisco (UCSF). Photography credit to Swati Bhargava, Optical Engineer (University of California, Berkeley).

With this AOSLO apparatus in combination with microperimetry techniques, it is possible to not only image cone structure, but also measure functional responses to light. Using AOSLO microperimetry (AOMP), light can be delivered to cone photoreceptors with high resolution (Tuten et al., 2012; Harmening et al., 2014). The combination of AOSLO with the psychophysics technique of delivering light and collecting responses from patients makes functional testing in RP patients feasible. AOMP has not previously been used in patients with RP to examine cone photoreceptor function where the outer segments are degenerating. Chapter 5 will describe AOMP used in patients with RP. In patients with RP, AOMP has the potential to identify cones that are partially degenerated but may be amenable to treatments directed towards photoreceptor rescue, and AOMP could also demonstrate improvement in visual function after treatment in such regions.

1.4 Multimodal retinal imaging for inherited retinal degenerations

Advances in genetics have allowed the identification of the genetic mutation in about two thirds of patients with IRDs (Consugar et al., 2015; Wang et al., 2014). Improved understanding the genetics of IRDs allowed more progress toward development of therapies, such as the use of induced pluripotent stem cells (iPSCs) as a disease model, as well as gene therapy validation (Tucker et al., 2011; Duong et al., 2018). Despite all of these advances in genetics and biological engineering, it remains vital to track disease progression for natural history studies, to assess structure and function of the retina in response to treatments that are being engineered, and to help select patients that are the best candidates for clinical trials (Sundaram et al., 2014). Furthermore, therapies are most effective when administered early, in the case of RP, when photoreceptors are still present, and high-resolution retinal imaging approaches can demonstrate photoreceptors amenable to treatment.

However, currently, clinical trial outcome measures do not often include high-resolution imaging or microperimetry techniques. Common clinical measures such as visual acuity tend to decline gradually over decades, and monitoring patients for years would be necessary to demonstrate a potential treatment safe and effective (Berson et al., 2007; Berson et al., 1993; Birch et al., 1999; Fishman et al., 2005; Grover et al., 1997; Sandberg et al., 2008). While the maintenance of visual acuity is vital, using it as an outcome measure for disease progression can be imprecise and influenced by issues that may not directly reflect photoreceptor degeneration (Talcott et al., 2011; Ratnam et al., 2013; Foote et al., 2018).

Thus, in order to expedite the process of IRD treatment development and ultimately prevent blindness, there is a critical need to use instrumentation that is more precise, objective and sensitive to measuring photoreceptor structure and function. Since there is no one imaging system that has all the necessary capabilities, a multimodal approach becomes indispensable.

To assess structure and function in RP and CHM, high-resolution instrumentation is vital. The use of AOSLO systems for capturing both confocal light from wave-guiding photoreceptors and nonconfocally wave-guided light to visualize cone inner segments is

fundamental for photoreceptor structure assessment, and AOMP provides high-resolution functional assessment. Although AOSLO and AOMP are not yet widely available, they provide valuable insight into understanding the structure and function of photoreceptors in IRD, and could have potential to provide sensitive outcome measures for clinical trials for patients with IRD (Talcott et al., 2011).

Standard, widely available clinical systems such as optical coherence tomography (OCT) and swept-source OCT (SS-OCT) are also vital for study of IRDs. These systems provide in-vivo, noninvasive, objective structural evaluation of the retina (Figure 1.4) including the internal limiting membrane (ILM), retinal nerve fiber layer (RNFL), ganglion cell layer (GCL), inner plexiform layer (IPL), inner nuclear layer (INL), outer plexiform layer (OPL), outer nuclear layer (ONL), external limiting membrane (ELM), inner segment/outer segment (IS/OS) junction or interdigitation zone (IZ) / ellipsoid zone (EZ), retinal pigment epithelium (RPE), Bruch's membrane (BM), choriocapillaris (CC), and choroidal vessels (CV). With greater penetration depth, SS-OCT facilitates angiography imaging (OCTA) (Gao et al., 2016), which could prove invaluable in research into how the retinal and choroidal vasculature are affected in IRDs, particularly CHM where choroidal irregularities are prevalent features (Duncan et al., 2018). Previous work has described the correlation between visual field and structural OCT abnormalities (Birch et al., 2013; Birch et al., 2011; Hood et al., 2009; Hood et al., 2011), indicating OCT may provide an objective measure of photoreceptor degeneration.

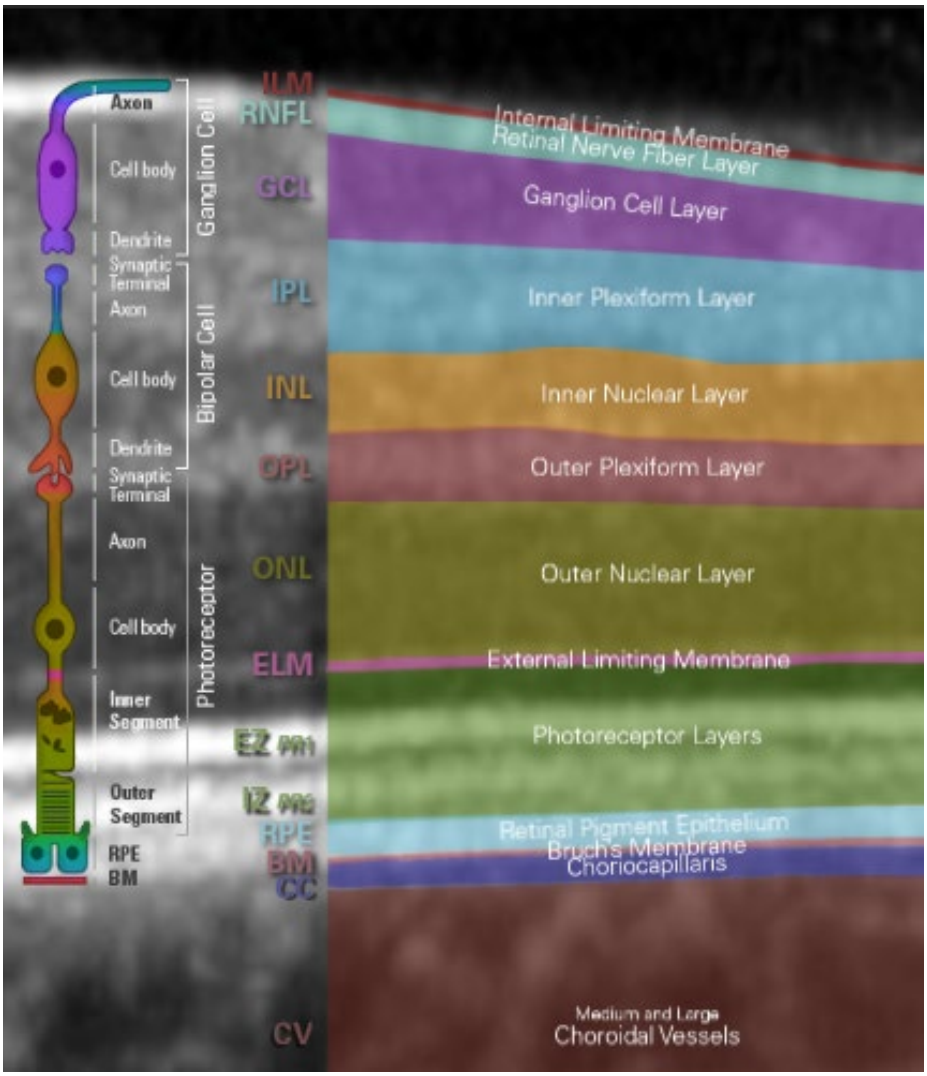

Figure 1.4 Retinal layers as shown from an OCT B-scan image, including schematic of the corresponding retinal cells. © 2019 Heidelberg Engineering, all rights reserved. Image available from: https://www.heidelbergengineering.com/int/news/retinal-layers-interactive-learning-module-20226231/

Fundus autofluorescence (FAF), is a non-invasive, in vivo imaging method to image bisretinoid constituents present in photoreceptor outer segments and RPE cells which can be excited from an external light source and then imaged (Sparrow et al., 2012). FAF images can be acquired using in vivo confocal scanning laser ophthalmoscopy (SLO) with short-wavelength (SW-AF) excitation. FAF has the capacity to expose lipofuscin fluorophores that accumulate in normal and diseased RPE cells from lysosomes filled with lipid residues (Sparrow 2018). When lipofuscin accumulates in RPE cells as a result of aging or disease, RPE cells appear hyperfluorescent on FAF images (Schmitz-Valckenberg 2008), and reduced FAF indicates RPE cell death. FAF imaging has been shown to be vital in studies concerned with IRD, and CHM especially (Jolly et al., 2016).

Visual acuity (VA) will always be a gold standard measure of vision (Ferris et al., 1982), and was used as a functional measure in Chapter 2. This dissertation also describes the use of AOSLO to deliver visual stimuli to the fovea after correcting for optical aberrations, and AOSLO-mediated VA was correlated with VA measured using standard clinical methods.

Systems that can measure retinal sensitivity with high accuracy and precision outside the fovea are also vital to study IRDs. AOMP ensures that a stimulus is delivered onto the desired retinal location through use of AOSLO eye-tracking which is high speed and image based (Wang et al., 2015). Functional results from a custom-built AOSLO/AOMP system were compared with data from a standard clinical fundus-guided microperimeter. In Chapter 3, use of the clinical microperimeter (MP1, Nidek Technologies, Fremont, CA, USA) is discussed. In more recent years, a new more modern, and easier to operate microperimeter, the fundus-guided Scotopic – Macular Integrity Assessment (S-MAIA, Centervue Inc., Fremont, CA) has come to the market, and in Chapters 4 and 5 this methodology was deployed.

1.5 Summary

To test macular cone structure and function in patients with IRD, structural measures using systems such as AOSLO, SD-OCT and FAF, combined with functional measures including VA, AOMP, and clinical fundus-guided microperimetry using either the MP1 or S-MAIA system, can provide information about photoreceptor health in IRD patients. Such structural and functional research in patients with IRD is vital because unfortunately, there are currently no cures for the majority of patients (Boughman et al., 1980; Bunker et al., 1984; Hartong et al., 2006), and development of novel treatments remains challenging. This dissertation discusses the use of multimodal imaging modalities for inherited retinal degenerations.

CHAPTER 2: Relationship between foveal cone structure and visual acuity measured with Adaptive Optics Scanning Laser Ophthalmoscopy in retinal degeneration

2.1 Abstract

Purpose: To evaluate foveal function in patients with inherited retinal degenerations (IRD) by measuring visual acuity (VA) after correction of higher-order aberrations.

Methods: Adaptive Optics Scanning Laser Ophthalmoscopy (AOSLO) was used to image cones in 4 normal subjects and 15 patients with IRD. The 840 nm scanning laser delivered an "E" optotype to measure AOSLO-mediated VA (AOSLO-VA). Cone spacing was measured at the preferred retinal locus by 2 independent graders and the percentage of cones below the average density of 47 age-similar normal subjects was computed. Cone spacing was correlated with best-corrected VA measured with the Early Treatment of Diabetic Retinopathy Study protocol (ETDRS-VA), AOSLO-VA and foveal sensitivity.

Results: ETDRS-VA significantly correlated with AOSLO-VA (ρ = 0.79, 95% CI: 0.5 to 0.9). Cone spacing correlated with AOSLO-VA (ρ = 0.54, 95% CI: 0.02 to 0.7), and negatively correlated with ETDRS letters read (ρ = -0.64, 95% CI: -0.8 to -0.2). AOSLO-VA remained ≥ 20/20 until cones decreased to 40.2% (95% CI: 31.1 to 45.5) below normal. Similarly, ETDRS-VA remained ≥ 20/20 until cones were 42.0% (95% CI: 36.5 to 46.1) below normal. Cone spacing Z-scores negatively correlated with foveal sensitivity (ρ = -0.79, 95% CI: -0.9 to -0.4) and foveal sensitivity was ≥ 35 dB until cones were 43.1% (95% CI: 39.3 to 46.6) below average.

Conclusion: VA and foveal cone spacing were weakly correlated until cones were reduced by 40-43% below normal. The relationship suggests that VA is an insensitive measure of foveal cone survival; cone spacing may be a more sensitive measure of cone loss.

2.2 Introduction

The fovea is the most important retinal region for human vision, yet its structure and function remain difficult to evaluate clinically. Cone photoreceptors at the fovea are difficult to resolve, even with adaptive optics, owing to their tight packing (Curcio et al., 1990) and the limits in resolution imposed by diffraction (Rossi and Roorda 2010). Decline in visual performance at the fovea (measured as visual acuity (VA) and foveal sensitivity) may remain undetected even after extensive cone loss (Geller et al., 1992; Ratnam et al., 2013). Our previous study of patients with inherited retinal degenerations (IRD) showed that, despite a significant correlation between VA and foveal sensitivity with foveal cone spacing, the relationship was both noisy and non-linear (Ratnam et al., 2013). As such, standardized ETDRS Snellen acuity measures did not drop below normal levels (<20/25) and foveal sensitivities remained normal (≥35 dB) until, on average, foveal cone density was 62% and 52% below normal, respectively (Ratnam et al., 2013). While preservation of foveal function is a beneficial adaptation for human vision, it limits the prospects for using subjective functional tests like ETDRS to gauge foveal health. Functional deficits may only manifest after

irreversible structural changes have already occurred. Consequently, these same subjective functional tests cannot serve as sensitive methods to monitor the effects of treatments that aim to slow, stop or reverse retinal degeneration (Fishman et al., 2005).

Structural indicators of foveal retinal health are also fraught with problems, even those that use adaptive optics. The small size of foveal cones makes them difficult to count, especially in images of patients who present additional challenges to imaging, including disease-associated cataracts, age-related cataracts, fixation instability, and lack of experience as a subject in advanced imaging systems. Even if foveal cones can be counted and tracked over time, not all visible cones may be functional. Finally, the lack of visible cones in an image does not necessarily imply a lack of function (Bruce et al., 2015; Tu et al., 2017).

The need for improved tests of retinal function is widely recognized, not only for improved measures of VA (Arditi and Cagenello 1993; Fishman et al., 1994; Grover et al., 1997; Vanden Bosch and Wall 1997) but also perimetry (Kim et al., 2007; Ross et al., 1984; Seiple et al., 2004), cone directionality (Stiles-Crawford effect) (Bailey et al., 1991; Birch et al., 1982), foveal thresholds (Alexander et al., 1986), and contrast sensitivity (Akeo et al., 2002; Lindberg et al., 1981; Wolkstein et al., 1980). In our previous report (Ratnam et al., 2013), we proposed several reasons why VA was not a sensitive indicator of early cone loss. First, because foveal cones generally over-sample the retinal image, VA may be limited by a ceiling effect imposed by the eye's optics and higher-level neural factors (Rossi et al., 2007). Second, fixational eye movements have been shown to improve acuity, even at the finest level (Ratnam et al., 2017; Rucci et al., 2007).

To address the optical limitations described above, we have developed Adaptive Optics Scanning Laser Ophthalmoscopy (AOSLO) mediated functional testing capabilities. Adaptive optics removes blur in the retinal image caused by the eye's aberrations (Liang and Williams 1997).

If the lack of sensitivity to early cone loss that we reported in the previous study is due to an optical ceiling effect, then AOSLO-mediated acuity ought to yield a stronger correlation. Indeed, visual performance, including VA, is improved in young, healthy individuals using adaptive optics (Rossi et al., 2007; Marcos et al., 2008; Yoon and Williams 2002), although the benefit is less evident in myopic subjects (Rossi et al., 2007) and is improved with practice (Rossi and Roorda 2010). In the current study, we used AOSLO-mediated acuity (without eye-motion correction) to test VA as a function of cone spacing in a cohort of patients with IRD. We included additional structural (OCT measures of cone outer segment length) and functional (foveal sensitivity) tests. If correcting the eye's aberrations improves the correlation between VA and cone spacing, then the addition of AOSLO-mediated acuity to AOSLO imaging could enhance our ability to evaluate the fovea in health and disease.

2.3 Methods

2.3.1 Study design

Research procedures followed the tenets of the Declaration of Helsinki. Informed consent was obtained from all subjects. The study protocol was approved by the institutional review boards of the University of California, San Francisco and the University of California, Berkeley.

2.3.2 Subjects

Seven eyes of 4 normal healthy subjects with normal eye examinations from unrelated families (1 female, 3 male) with an average age of 50.25 years (SD 7.85) were used as controls; normal subjects did not undergo genetic testing. Twenty two eyes from 15 patients (5 female and 10 male) with an average age of 40.73 years (SD 11.39) with IRD from 15 unrelated families were clinically characterized (Table 2.1). Patients were excluded if they had conditions that could affect visual acuity, including cataract, amblyopia, and cystoid macular edema involving the fovea. Seven participants were enrolled in a clinical trial of an experimental treatment that was administered to only one eye; with the fellow eye receiving a sham treatment. Sham treated eyes from these seven patients were used as the study eyes for this manuscript. For one subject (40037) with autosomal recessive RP (ARRP) the eye with better visual acuity was chosen as the study eye. All eyes selected for this study had unambiguous cones within 0.5 degrees of the preferred retinal locus (PRL) and steady fixation. Genetic testing was performed on patients with X-linked RP, autosomal dominant RP and Usher syndrome type 2 through the eyeGENE research consortium (Sullivan et al., 2013), on patients with autosomal recessive RP through a research protocol (Biswas et al., 2017) or using a next-generation sequencing panel on a fee-for-service basis (retinal dystrophy panel of 181 genes, Blueprint Genetics, San Francisco, CA, USA), and Usher syndrome type 3 on a fee-for-service basis by the Carver nonprofit genetic testing laboratory (Ratnam et al., 2013).

Table 2.1. Clinical characteristics of healthy normal subjects and patients with IRD. dB, decibels; ETDRS, early treatment of diabetic retinopathy study (Ferris et al., 1982); AOSLO, adaptive optics scanning laser ophthalmoscopy; OS, outer segment; ROI, region of interest; M, male; F, female; RE, right eye; LE, left eye; SE, study eye; DS, diopter sphere; SD, standard deviation; RP, retinitis pigmentosa; AR, autosomal recessive; AD, autosomal dominant; XL, X-linked; for AOSLO and ETDRS acuity, mean angle of resolution (MAR) was converted to a fraction in Table 2.1 for easier comparison between the acuity measures.

AOSLO ID	Sex	Age	Diagnosis/Mutation	Eye	Refractive Error	Axial Length, mm	Foveal Threshold, dB	ETDRS, letters read	ETDRS Acuity	AOSLO Acuity	OS Thickness, µm	Cone Spacing, arcmin	ROI Eccentricity, degrees	Cone Spacing, Z-score
Healthy controls														
10033	M	59	Normal	RE	+0.75+0.25x135	23.96	34	95	20/13	20/14	44.74	0.83	0.21	1.07
				LE	+0.25+0.50x165	24.07	36	95	20/13	20/18	51.45	0.80	0.08	1.34
40051	M	50	Normal	RE	+0.25+0.50x180	23.74	37	94	20/13	20/20	53.95	0.85	0.12	1.67
40053	F	40	Normal	RE	-0.75+0.25x165	23.74	37	89	20/16	20/16	58.71	0.78	0.16	0.86
				LE	plano+0.25x165	24.03	37	92	20/13	20/17	57.76	0.79	0.24	0.64
40055	M	52	Normal	RE	-0.25DS	23.93	36	96	20/13	20/16	64.20	0.80	0.21	0.83
				LE	-0.75DS	23.84	35	91	20/16	20/16	64.27	0.81	0.17	1.06
Mean		**50.25**				**23.90**	**36**	**93.14**	**20/13.86**	**20/16.71**	**56.44**	**0.81**	**0.17**	**1.07**
SD		**7.85**				**0.13**	**1.15**	**2.54**	**1.08**	**1.10**	**7.03**	**0.02**	**0.06**	**0.35**
Inherited retinal degenerations														
30007	F	30	Usher syndrome type 3: homozygous CLRN1 mutations c.144T>G, p.Asn48Lys (pathogenic)	SE	-0.75+0.50x025	22.68	34	86	20/20	20/20	42.04	0.91	0.12	2.15
30015	M	43	Simplex RP/PRPH2 c.634A>G, p.Ser212Gly (likely pathogenic)	SE	-2.75DS	23.95	38	84	20/20	20/21	38.72	0.81	0.05	1.58
40031	M	49	RP simplex	SE	-1.00+0.75x045	24.83	34	80	20/25	20/39	35.53	0.95	0.21	2.14
40032	M	33	ARRP: compound heterozygous RPE65 mutations (c.1451G>A, p.Gly484Asp and c.746A>G, p.Tyr249Cys) and homozygous ABCA4 mutations (c.5882G>A, p.Gly1961Glu)	SE	-3.00+4.00x090	23.65	35	83	20/25	20/32	22.20	0.90	0.09	2.25
40037	M	38	ARRP: compound heterozygous mutations in *CNGA1* c.94C>T, p.Arg32* (pathogenic) c.1511A>G, p.Asp504Gly (VUS)	RE	-0.25+0.25x090	23.06	35	90	20/16	20/14	58.65	0.88	0.16	1.75
40039	M	45	ARRP: USH2A: c.2276G>T, p.Cys759Phe and c.2296T>C, p.Cys766Arg (pathogenic)	RE	-0.50+0.50x175	23.31	41	91	20/20	20/11	46.63	0.82	0.21	1.01
				LE	plano+0.50x165	23.25	38	89	20/16	20/12	55.22	0.84	0.19	1.24
40041	F	43	ARRP: compound heterozygous mutations in *USH2A*: c.2276G>T, p.Cys759Phe and c.8682-3T>G, splice site mutation	RE	-11.25DS	26.73	40	84	20/20	20/22	49.18	0.84	0.23	1.08
				LE	-11.00+0.25x120	26.31	35	84	20/20	20/26	54.04	0.82	0.25	0.82
40064	M	21	XLRP: RPGR hemizygous c.1243_1244delAG, p.Arg415Glyfs*27 (pathogenic)	SE	-9.50+2.50x137	26.71	37	84	20/25	20/24	51.09	0.88	0.17	1.73
40067	M	44	XLRP: hemizygous mutation in *RPGR* c.2360_2362del, p.Gly787del	SE	-1.00+0.50x180	23.23	36	91	20/16	20/22	47.05	0.84	0.21	1.18
40070	F	41	Simplex RP, IFT140 c.634G>A, p.Gly212Arg (pathogenic) and c.1390G>T, p.Val464Leu (likely pathogenic); one inherited from each parent	SE	-1.75+0.50x085	24.59	36	87	20/20	20/10	42.36	0.85	0.14	1.55
40073	F	34	ADRP due to PRPF31 mutation *PRPF31* c.239-1 del	RE	-4.25+0.75x090	24.54	37	90	20/16	20/9	49.53	0.86	0.13	1.72
				LE	-4.25+0.75x090	24.83	38	93	20/16	20/12	46.21	0.86	0.12	1.71
40093	M	64	RP Simplex	RE	-2.00DS	23.86	29	69	20/40	20/32	50.28	0.95	0.12	2.55
				LE	-0.25+0.50x010	23.73	33	72	20/40	20/30	42.75	0.93	0.07	2.57
40094	M	61	RP Simplex	RE	-8.25+1.00x180	25.70	33	78	20/32	20/28	11.01	0.96	0.13	2.61
				LE	-8.25+1.25x180	25.57	32	76	20/32	20/29	24.30	0.92	0.18	2.02
40095	M	34	ADRP: *RHO* c. 810C>A, p. Ser270Arg	RE	-2.00+0.75x120	23.36	38	85	20/20	20/17	51.13	0.82	0.22	0.95
				LE	-2.00+0.75x090	23.38	36	89	20/16	20/14	60.65	0.78	0.06	1.32
40097	F	31	Usher syndrome type 2A with *USH2A* homozygous c.2299delG, p. Glu 767 Ser fs X 21	RE	-2.50+0.50x090	23.01	32	81	20/25	20/23	25.75	1.00	0.07	3.19
				LE	-2.75DS	23.03	31	77	20/32	20/23	26.55	0.92	0.11	2.27
Mean		**40.73**				**24.24**	**35.36**	**83.77**	**20/23.27**	**20/21.36**	**42.31**	**0.88**	**0.15**	**1.79**
SD		**11.39**				**1.26**	**2.97**	**6.39**	**1.60**	**1.71**	**13.04**	**0.06**	**0.06**	**0.63**

2.3.3 Clinical examination

A standard illuminated eye chart was used to measure best-corrected visual acuity (BCVA) according to the Early Treatment of Diabetic Retinopathy Study (ETDRS) protocol (Ferris et al., 1982). Although VA can be specified using different scales, a common measure is the minimal angle of resolution (MAR) (Ferris et al., 1982; Bailey et al., 1976), and in this study, measures of ETDRS were specified in MAR, computed into decimal form by dividing the denominator by the numerator of the VA fraction. We also displayed this data as the number of letters read on the ETDRS chart to retain consistency and comparability with the previous study (Ratnam et al., 2014).

2.3.4 Perimetry measurements

Automated perimetry (Humphrey Visual Field Analyzer HFA II 750-6116-12.6; Carl Zeiss Meditec, Inc., Dublin, CA) using a 10-2 Swedish interactive threshold algorithm (SITA) was used to measure foveal thresholds. A Goldmann III stimulus was presented on a white background (10.03 cd/m^2) with exposure duration of 200 ms. Foveal sensitivity was displayed in decibel scale (dB).

2.3.5 Cross sectional thickness measurements

Cross sectional measures of retinal thickness at the fovea were acquired from 20 degree horizontal and vertical spectral domain optical coherence tomography (SD-OCT; Spectralis HRA+OCT system [Heidelberg Engineering, Vista, CA, USA]) B-scans through the fovea. SD-OCT B-scans were segmented using custom software as previously described (Bailey et al., 2011; Hood et al., 2011; Hood et al., 2009; Wen et al., 2012; Wen et al., 2011) to calculate inner and outer segment thickness (Igor Pro 7, WaveMetrics, Lake Oswego, OR) at 0.1 degree locations along the scans (Aizawa et al., 2009).

2.3.6 AOSLO mediated visual acuity

Prior to AOSLO imaging, eyes were dilated with 1% tropicamide and 2.5% phenylephrine. High-resolution images of the cone mosaic within 0.5 degree of the PRL were obtained using AOSLO ("ROI Eccentricity", Table 2.1). The "E" optotype was introduced onto the retina by modulating the 840 nm scanning laser to project sharp, black letters against a red background (Rossi and Roorda 2010). The letter E was presented for 1 second (30 frames) during each trial oriented in one of four directions: left, right, up, or down. The subjects reported the orientation of the E using a keyboard. Two correct responses in succession elicited an E of decreased size (reduced by 1.4 times), whereas one incorrect response prompted the appearance of an E that increased in size (increased by 1.4 times) in the next trial. Following seven complete reversals, the experiment terminated. The value of the final threshold was calculated by averaging the stimulus size of the last four reversals. Each subject repeated the experiment 6 times and the average threshold per experiment was converted to generate a standard MAR acuity value. This one-up/two-down procedure usually converged to 70.7% correct performance (Garcia-Perez 1998). AOSLO-VA measures required an additional 15-20 minutes per eye to complete these repetitions.

2.3.7 AOSLO image procurement and cone spacing and density analysis

Montages of the macular region of the AOSLO images were created as described (Duncan et al., 2007). To identify the PRL, a 10-15 second video was recorded as the subject observed a small circular fixation target delivered through modulation of the AOSLO scanning raster, the location of which was directly recorded in the AOSLO video. Using custom image analysis tools created with MATLAB (The MathWorks, Inc., Natick, MA), the mean and standard deviation (SD) of locations of fixation points in both horizontal and vertical directions were documented. To quantify cone spacing measures, a density recovery profile method

(Rodieck 1991) was used as described previously (Duncan et al., 2007). We chose this method to estimate cone spacing because it allows for reliable estimates of cone spacing in mosaics where not every cone is visible and it remains a meaningful and robust metric even when the cones are no longer close-packed into a hexagonal lattice. Other measures of cone spacing, such as nearest neighbor distance or row-to-row spacing, are linearly related and so whatever correlations are found with one metric will be essentially the same for the others. Cone locations were measured as eccentricity in degrees from the PRL. Cone spacing was measured as close as possible to the PRL center by 2 independent graders within a standardized 0.1 degree^2 (42×42 pixel) box (Figure 2.1); the interclass correlation coefficient (ICC) for the 2 graders was 0.49 (95% CI 0.3 to 0.7). Given the small number of subjects, the mean absolute deviation was compared to the mean of all cone spacing measures. The overall mean absolute difference was 0.05 with a corresponding overall mean measurement cone spacing value of 0.87. The mean absolute difference divided by the mean measurement value was about 6% of the average cone spacing value. The measure calculated by each grader was averaged to derive the mean cone spacing at each ROI for correlation analyses.

Due to the increase in photoreceptor density approaching the foveal center (mean eccentricity, 0.16 degree; maximum eccentricity, 0.24 degree), where abrupt changes in cone spacing would impact the results, cone spacing measures were converted to Z-scores (standard deviations from normal spacing), which are expected to be more uniform across the foveal region. Z-scores were based on mean cone spacing at the measured eccentricity calculated from a larger normal data set (Zayit-Soudry et al., 2015) composed of 10 controls (4 male, 6 female) between ages 25-58 (average 45.2 years, SD 10.3 years); normal Z-scores were between -2 and 2.

2.3.8 Data analysis and statistics

All cone spacing measurements were correlated with ETDRS VA, AOSLO-mediated VA, and foveal sensitivity. Correlations between parameters were assessed using the Spearman rank correlation coefficient ρ, and a bootstrap analysis clustered by patient to account for the fact that one eye was used in some subjects and both eyes were used in others was used to derive the 95% confidence interval (CI) values. Statistical significance was determined using the 95% CIs. The percentage of cones below average was computed to indicate the difference in cone density from the average of 47 normal subjects, as described in our previous study (Ratnam et al., 2013) The percentage of cone loss needed to reach performance scores below specified thresholds for example, below a MAR of 1.0 (20/20 VA) are indicated by the red and blue lines on Figures 2.4B, 2.5B, 2.6B and were computed from a quadratic curve fitting which was then bootstrapped to obtain the 95% bias-corrected/accelerated confidence intervals.

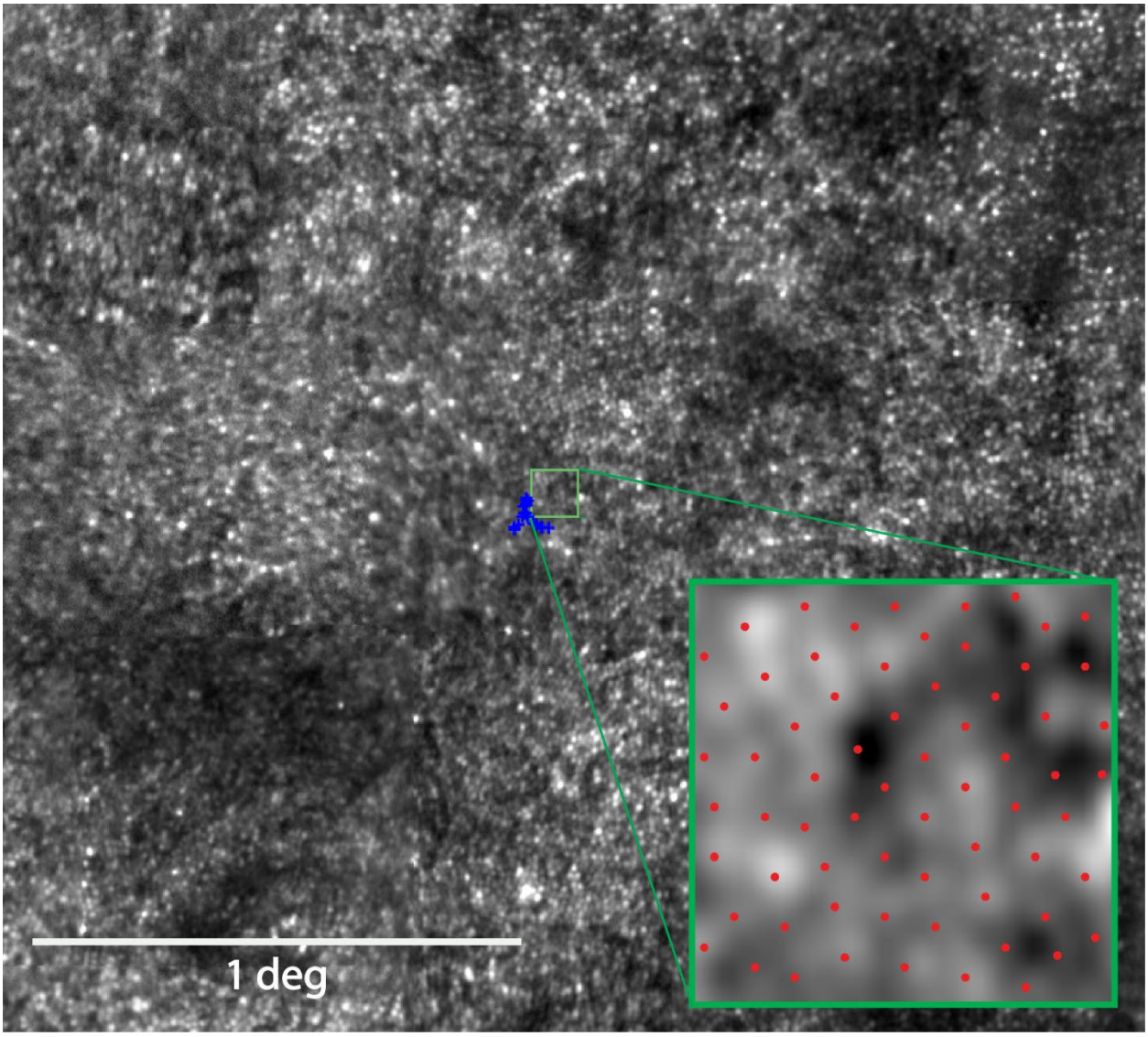

Figure 2.1: AOSLO image of 43 year old male with retinitis pigmentosa simplex (30015). The blue crosses indicate the fixation locus and its centroid was used to determine the preferred retinal locus (PRL) for fixation. The green box outlines the region of interest (ROI) selected for cone spacing analysis. Inset: Magnified view of the ROI with red dots indicating the selected cone locations.

2.4 Results

ETDRS-VA was not significantly correlated with AOSLO-VA in normal subjects (ρ = -0.33, 95% CI: -1.0 to 0.3), but it was significantly correlated in IRD patients (ρ = 0.79, 95% CI: 0.5 to 0.9) (Figure 2.2). Similarly, ETDRS Letters Read correlated negatively with AOSLO-VA (Figure 2.3); the correlation was not significant in normal subjects (ρ = -0.02, 95% CI: -0.9 to 1.0), but was significant in IRD patients (ρ = -0.84, 95% CI: -0.9 to -0.6).

The cone spacing Z-scores and AOSLO-VA relationship was significant in IRD patients (ρ = 0.54, 95% CI: 0.02 to 0.7), but not in normal subjects (ρ = 0.37, 95% CI: -0.8 to 1.0). Cone spacing Z-scores were also significantly correlated with ETDRS Letters Read in IRD patients (ρ = -0.64, 95% CI: -0.8 to -0.2), but not in normal subjects (ρ = 0.16, 95% CI: -1.0 to 0.8). The similarity in correlation of AOSLO-VA and ETDRS with Z-scores suggests that correcting the optical aberrations in this cohort of subjects did not give rise to improved structure/function relationships.

Figure 2.4B plots AOSLO-VA vs. percentage of cones below average. The analysis shows that cone density decreased to 40.2% below normal (95% CI: 31.1 to 45.5) before AOSLO-VA dropped below 20/20, and decreased to 48.9% fewer cones than normal (95% CI: 44.5 to 58.6) before AOSLO-VA dropped below 20/25. Figure 2.5B plots are similar to 2.4B but with ETDRS-VA rather than AOSLO-VA. The cone density thresholds associated with acuity below 20/20 and 20/25 were 42.0% (95% CI: 36.5 to 46.1) and 49.5% fewer than normal (95% CI: 46.2 to 59.7), respectively.

Cone spacing Z-scores were significantly correlated with foveal sensitivity in IRD patients (ρ = -0.79, 95% CI: -0.9 to -0.4), but not in normal subjects (ρ = -0.19, 95% CI: -0.8 to 1.0). A percent of cones below average of 43.1% (95% CI: 39.3 to 46.6) or more would be needed to detect a drop in foveal sensitivity below 35 dB (Figure 2.6B).

Finally, when cone spacing Z-scores were analyzed with cross-sectional measures of OS thickness, a significant correlation was seen in IRD patients alone (ρ = -0.61, 95% CI: -0.8 to -0.2), but not in normal subjects (ρ = -0.54, 95% CI: -0.9 to 1.0).

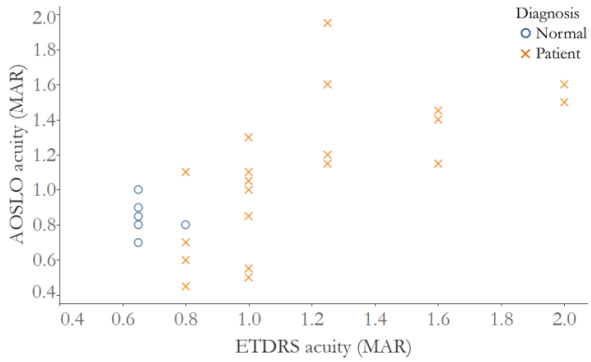

Figure 2.2. Visual acuity measured after correction with AOSLO is significantly correlated with visual acuity measured using ETDRS charts. Correlation of ETDRS MAR acuity and AOSLO acuity, normal subjects: ρ = -0.33, 95% CI: -1.0 to 0.3; IRD patients: ρ = 0.79, 95% CI: 0.5 to 0.9.

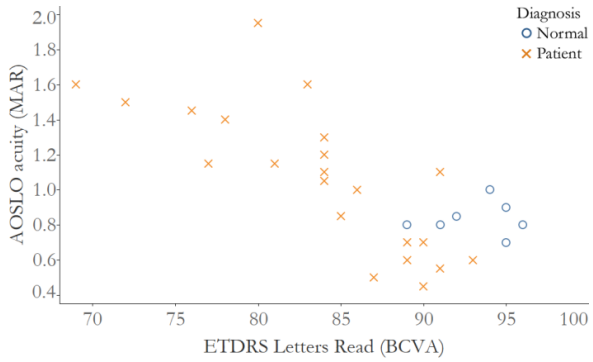

Figure 2.3. Visual acuity measured after correction with AOSLO is significantly correlated with visual acuity measured with numbers of letters read using ETDRS charts. Correlation of ETDRS Letters Read acuity and AOSLO acuity, normal subjects: ρ = -0.02, 95% CI: -0.9 to 1.0; IRD patients: ρ = -0.84, 95% CI: -0.9 to -0.6.

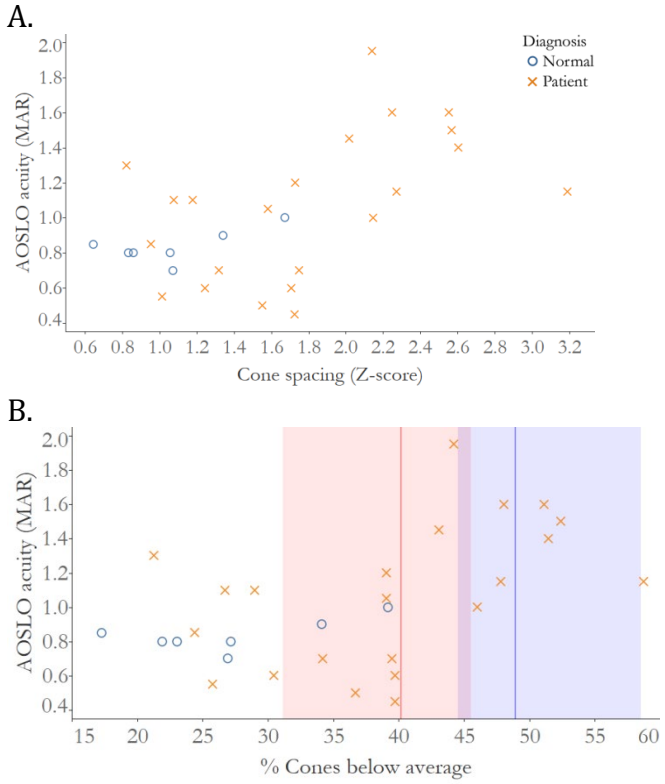

Figure 2.4. Visual acuity measured after correction with AOSLO is significantly correlated with cone loss measured as increased cone spacing Z-score. A. Correlation of cone spacing Z-scores and AOSLO acuity, normal subjects: ρ = 0.37, 95% CI: -0.8 to 1.0; IRD patients: ρ = 0.54, 95% CI: 0.02 to 0.7. B. Correlation of % cones below average and AOSLO acuity; red line: threshold percent cone loss where vision drops below normal MAR >1.00 (20/20 VA): 40.2%, red shading: 95% CI: 31.1 to 45.5; blue line: threshold percent cone loss where vision drops below normal MAR >1.25 (20/25 VA): 48.9%, blue shading: 95% CI: 44.5 to 58.6.

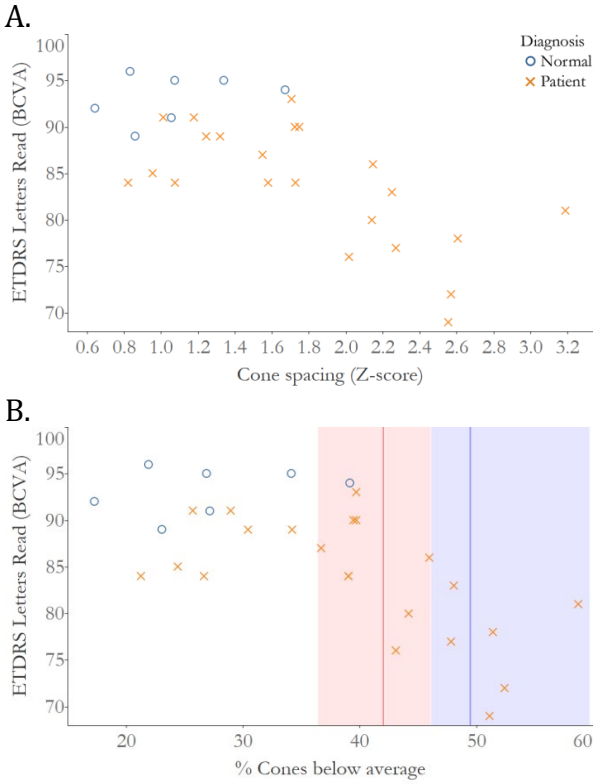

Figure 2.5. Visual acuity measured using standardized eye charts according to the ETDRS protocol is significantly correlated with cone loss measured as increased cone spacing Z-score. A. Correlation of cone spacing Z-scores and ETDRS acuity, normal subjects: ρ = 0.16, 95% CI: -1.0 to 0.8; IRD patients: ρ = -0.64, 95% CI: -0.8 to -0.2. B. Correlation of % cones below average and ETDRS acuity, red line: threshold percent cone loss where vision drops below normal <85 letters (20/20 VA): 42.0%, red shading: 95% CI: 36.5 to 46.1; blue line: threshold percent cone loss where vision drops below normal <80 Letters (20/25 VA): 49.5%, blue shading: 95% CI: 46.2 to 59.7.

A.

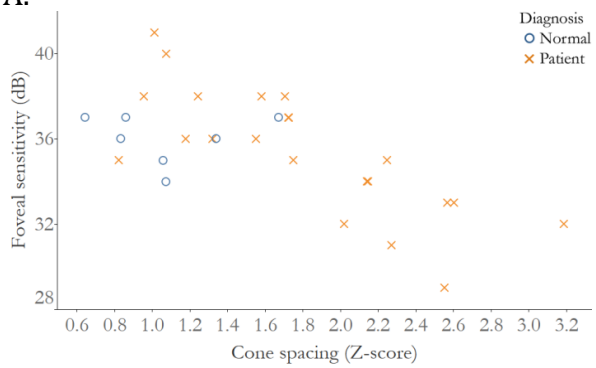

B.

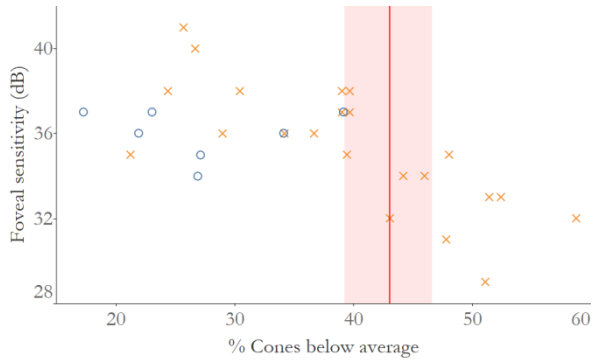

Figure 2.6. Foveal sensitivity is significantly correlated with cone loss measured as increased cone spacing Z-score. A. Correlation of cone spacing Z-scores and foveal sensitivity, normal subjects: ρ = -0.19, 95% CI: -0.8 to 1.0; IRD patients ρ = -0.79, 95% CI: -0.9 to -0.4. B. Correlation of % cones below average and foveal sensitivity; red line: threshold percent cone where vision drops below normal foveal sensitivity (<35dB): 43.1%, red shading: 95% CI: 39.3 to 46.6.

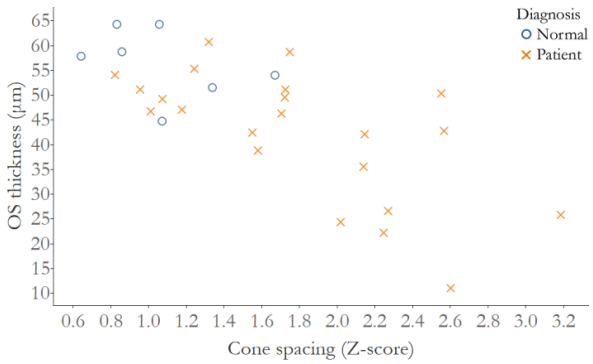

Figure 2.7. OS thickness is significantly correlated with cone loss measured as increased cone spacing Z-score. Correlation of cone spacing Z-scores and OS thickness, normal subjects: ρ = -0.54, 95% CI: -0.9 to 1.0; IRD patients: ρ = -0.61, 95% CI: -0.8 to -0.2.

2.5 Discussion

The present study revealed significant correlations between measures of cone structure with measures of visual function at or near the fovea. As cone spacing increased, there was a significant decline in VA. Additionally, ETDRS-VA and AOSLO-VA were similarly correlated with cone spacing Z-scores measured near the foveal center. In both cases, the relationship was noisy and nonlinear. Furthermore, a similar reduction in cone density of about 40% below normal was required before clinically measurable changes in either measure of acuity were observed. Despite correcting for optical imperfections, AOSLO-VA did not result in significant improvement in this structure/function relationship.

One notable finding was that for all normal subjects, and just under half of the IRD subjects, AOSLO-VA was worse than ETDRS-VA. We offer four possible explanations for this.

First, ETDRS-VA and AOSLO-VA not only employed different methods (letters read on an acuity chart vs. a 4-alternative-forced-choice tumbling E staircase procedure) but also converged to different thresholds (82% (Ferris et al., 1982) vs. 70.7% (Garcia-Perez 1998) correct). This is an unlikely explanation because, if anything, the lower threshold for the AOSLO-VA ought to have yielded slightly better performance, but it did not.

Second, AOSLO-VA was administered using 840 nm light with more than 20 times lower luminance (~ 4 cd/m^2) than the standard light box used to measure ETDRS-VA (85 cd/m^2). AOSLO-VA measures better than clinical measures of VA were achieved using nearly identical measurement conditions and a similar system in earlier reports (Rossi and Roorda 2010). The subjects in the earlier reports, however, were healthy, younger, emmetropic, and had extensive experience using the AOSLO system.

Third, a possible interpretation for the lack of improvements in VA with aberration correction could be that the receptive fields in our subjects (both normals and IRD subjects) comprise more than single cones. Eliminating the aberrations would confer little benefit if this were the case - which is what we found - and a random loss of cones within larger receptive field would only have minimal effects on the sampling resolution until many cones were lost - which is also what we found. However, we have every reason to believe that there are at least two midget ganglion cells per foveal cone in our healthy normals and that cone spacing imposes the retinal limit on foveal visual acuity. Measurement of the limits of human spatial vision at the fovea in young healthy eyes confirms this (Rossi and Roorda 2010). It is very unlikely that this ratio would be any different in the slightly older normals we used for this study (average age of 50 years) and the comparable acuity of the less-advanced IRD patients suggests that this is true for them as well.

The most likely explanation arises from the facts that subjects in this study (i) were older, perhaps with subclinical lens opacities, (ii) were unfamiliar with the AOSLO-VA task, (iii) were not emmetropic (see Table 2.1), and (iv) had little or no experience being imaged in an AOSLO. Collectively, these facts probably explain why AOSLO-VA measures were slightly worse than ETDRS-VA. This final explanation is important because, until AOSLO-mediated functional tests become more widely available, robust and efficient, subjects will often have limited experience with the test.

IRD subjects seemed to benefit more from AO-correction than normal subjects, perhaps because the IRD subjects' aberrations were, on average, greater. Greater aberrations in retinitis pigmentosa patients have been reported (Rajagopalan et al., 2005) but the aberration of the eyes in our study was not recorded or analyzed before AO-correction.

2.5.1 Cone spacing compared with ETDRS and AOSLO acuities

In patients with IRD, both ETDRS and AOSLO-mediated acuities were correlated with cone spacing Z-scores. The significant correlations demonstrated that greater cone spacing -

indicating cone loss - corresponded to worse acuity performance. Normal subjects, however, did not demonstrate a statistically significant correlation between acuity and cone spacing. It is clear that factors outside of cone spacing and optics (see earlier discussion) govern acuity performance in the normal healthy eyes that were part of this study. There are no obvious advantages of AOSLO-mediated acuity over conventional measures for assessing foveal structure.

We consistently found that VA did not decrease until cone densities were about 40% lower than the average for normal eyes. The thresholds for ETDRS acuity were similar to a previous study, and the present study demonstrated a similar threshold for AOSLO-mediated VA (Ratnam et al., 2013). Despite differences in the actual reported thresholds, the 95% confidence intervals between studies overlap (compare Figures 2.4B, 2.5B in the present paper with figure 4 from Ratnam et al., 2013).

2.5.2 Cone spacing compared with foveal sensitivity

As with acuity, there was a significant relationship between foveal sensitivity and cone spacing Z-scores, but the data were noisy and nonlinear, and significant declines in foveal sensitivity were not observed reliably until cones were well below the normal average. The cone density threshold to detect foveal sensitivities below 35dB was similar between the current and our previous report (Ratnam et al., 2013). Although the thresholds were different (43% vs. 52% (Ratnam et al., 2013)), the 95% confidence intervals overlapped. However, the range of percent cone loss associated with reduced visual acuity and foveal sensitivity was narrower in the present study, refining the threshold to near 40-50% cone loss for all abnormal measures of foveal function. As reported in previous studies based on computer modeling (Geller et al., 1992), visual (grating) acuity is not directly associated to the mean density or spacing of photoreceptors at the fovea.

2.5.3 Cone spacing compared with outer segment thickness

For IRD, cone spacing Z-scores correlated negatively with OS thickness. As cones degenerate, the OS becomes thinner, due to decreased length of outer segments, which likely precedes cone loss with increased cone spacing during degeneration (Lazow et al., 2011; Milam et al., 1998). However, no correlation was observed in normal subjects, due to the absence of photoreceptor degeneration.

2.6 Summary

In conclusion, even after correcting high-order aberrations, the relationship between VA and foveal cone spacing was weak until cone densities were 40-50% lower than the normal average. The non-linear relationship and variability suggest that VA, whether measured by conventional methods or with optical correction through the AOSLO, remains an ineffective way to gauge early changes in foveal cone spacing or density, and that cone spacing may be a more sensitive measure of cone loss in early stages of degeneration. On a positive note, the fact that AOSLO imaging can detect structural changes in the cones well in advance of the

acuity loss means that there is a therapeutic window within which one can treat and monitor effectiveness in advance of any visual impact for the patient.

2.7 Acknowledgements

The work presented in this chapter was published as a peer-reviewed manuscript in *Investigative Ophthalmology & Visual Science* in May 2018. Citation:
Foote KG, Loumou P, Griffin S, Qin J, Ratnam K, Porco TC, Roorda A, Duncan JL. Relationship between foveal cone structure and visual acuity measured with adaptive optics scanning laser ophthalmoscopy in retinal degeneration. Investigative ophthalmology & visual science. 2018 Jul 2;59(8):3385-93.

Dr. Jacque Duncan (Department of Ophthalmology, University of California, San Francisco) provided instrumental contributions to the conception, design, implementation, and examination of this study. Dr. Austin Roorda (School of Optometry, University of California, Berkeley) provided vital support in design, analysis, and interpretation of the work in this study. The work that went into this project would not have been possible without co-author Panagiota Loumou who presented a preliminary version of this study first at the 2016 Association for Research in Vision and Ophthalmology (Seattle, Washington). Efforts in data collection and technical assistance were provided from co-authors Shane Griffin, Jia Qin, and Kavitha Ratnam. Co-author Travis Porco is recognized for his assistance with the data analysis. Pavan Tiruveedhula is thanked for the implementation and technical savvy and support of the hardware and software systems of the AOSLO system. Much appreciation and thanks are given to these collaborators for their contributions as well as permission to include the work in this chapter.

CHAPTER 3: Cone spacing correlates with retinal thickness and microperimetry in patients with inherited retinal degenerations

3.1 Abstract

Purpose: To determine whether high-resolution retinal imaging measures of macular structure correlate with visual function over 36 months in retinal degeneration (RD) patients and normal subjects.

Methods: Twenty-six eyes of 16 RD patients and 16 eyes of 8 normal subjects were studied at baseline; 15 eyes (14 RD) and 11 eyes (6 normal) were studied 36 months later. Adaptive Optics Scanning Laser Ophthalmoscopy (AOSLO) was used to identify regions of interest (ROIs) with unambiguous cones at baseline to measure cone spacing. AOSLO images were aligned with spectral-domain optical coherence tomography (SD-OCT) and fundus-guided microperimetry results to correlate structure and function at the ROIs. SD-OCT images were segmented to measure inner segment (IS) and outer segment (OS) thickness. Correlations between cone spacing, IS and OS thickness and sensitivity were assessed using Spearman correlation coefficient ρ with bootstrap analyses clustered by person.

Results: Cone spacing (ρ=0.57, P<0.001) was significantly correlated with eccentricity in patients. Controlling for eccentricity, cone spacing Z-scores were inversely correlated with IS (ρ=-0.29, P=0.002) and OS thickness (ρ=-0.39, P<0.001) in RD patients only, and with sensitivity in normal subjects (ρ=-0.22, P<0.001) and RD patients (ρ<-0.38, P<0.001). After 36 months, cone spacing increased (P<0.001) and macular sensitivity decreased (P=0.007) compared to baseline in RD patients.

Conclusions: Cone spacing increased and macular sensitivity declined significantly in RD patients over 36 months. High resolution images of cone structure correlated with retinal sensitivity, and may be appropriate outcome measures for clinical trials in RD.

3.2 Introduction

Retinitis pigmentosa (RP) refers to a diverse group of hereditary retinal degenerative disorders that all cause progressive, diffuse, and relentless loss of photoreceptors, resulting in vision loss and, ultimately, blindness. RP is a leading cause of hereditary blindness in developed countries and affects 1 in 3,500 people worldwide (Hartong et al., 2006). RP manifests with nyctalopia, progressive visual field constriction, and eventual decline in visual acuity. Loss of visual function accompanies fundus findings including retinal pigment epithelium (RPE) changes, arteriolar attenuation, waxy optic disc pallor, and variable bone spicule pigmentation (Robson et al., 2008). RP can occur in isolation or as part of a syndrome that involves other organs, such as Usher syndrome, which is characterized by sensorineural hearing loss in addition to retinal degeneration (RD) (Hartong et al., 2006). Although RP is characterized clinically by degeneration and death first of rod, followed by cone, photoreceptors, RP is genetically heterogeneous and has been associated with mutations in

over 87 genes (https://www.omim.org/phenotypicSeries/PS268000), each of which may affect rod and cone survival differently.

Because photoreceptor death is slowly progressive over many years, it has been challenging to demonstrate that treatments and cures are safe and effective. Specific, reliable, precise, objective, and sensitive measures of photoreceptor health and survival are urgently needed to expedite development of treatments to prevent blindness, monitor disease progression and measure response to therapies.

Previous studies have shown that measures of visual function in RP correlate with the integrity of the photoreceptor layers imaged using spectral domain optical coherence tomography (SD-OCT) (Birch et al., 2015; Birch et al., 2013; Hood et al., 2011). However, current SD-OCT techniques lack sufficient resolution for examination of individual photoreceptors, raising the possibility that subtle changes in photoreceptor structure may be missed. In contrast, adaptive optics scanning laser ophthalmoscopy (AOSLO) has been used to visualize the retina with lateral resolution at the single cell level (Roorda and Duncan 2015; Roorda et al., 2002) to enable imaging of the cone mosaic and measurement of cone spacing and density, and has been used to study eyes with inherited retinal degenerations (Duncan et al., 2007; Sun et al., 2016; Wolfing et al., 2006). Cone density and spacing correlate with clinical measures of visual function including visual acuity and foveal sensitivity in RD (Chen et al., 2011; Ratnam et al., 2013) suggesting that the high-resolution measures of cone structure obtained with AOSLO may be useful in tracking disease progression (Talcott et al., 2011; Litts et al., 2017).

However, in eyes with RD, cone spacing and density have not always been found to correlate with cross-sectional measures of photoreceptor layer thickness obtained with SD-OCT (Battu et al., 2015; Chui et al., 2012; Menghini et al., 2014) possibly because rods contribute to measures of outer nuclear layer thickness outside the fovea, and some cones have diminished reflectivity (Bruce et al., 2015; Tu et al., 2017; Wang 2015), accounting for decreased cone density measures in regions with normal cross-sectional thickness. Confocal AOSLO images of photoreceptors are generated by light reflected at the photoreceptor inner segment/outer segment (IS/OS) and OS/RPE junctions (Miller et al., 1996), while the cell bodies of degenerating photoreceptors may persist in the outer nuclear layer (ONL) even after the IS and OS have degenerated (Milam et al., 1998). Thus, it is possible that areas with intact photoreceptor cell bodies but degenerating IS and OS with reduced visual function show no correlation between cone spacing or density and cross-sectional measures of ONL thickness from OCT scans.

Prior studies have demonstrated a correlation between cone spacing measures with AOSLO and visual function at the fovea in patients with retinal degenerations (Ratnam et al., 2013), and parafoveal cone density has been correlated with spatial contrast sensitivity (Hirota et al., 2017) and multifocal electroretinography (Choi et al., 2006) but the relationship between retinal structure and visual sensitivity measured using microperimetry to assess function at macular locations outside the central fovea has not been previously reported on a cellular level in RP.

The current study was designed to test the hypothesis that cone spacing measures from confocal AOSLO images correlate with typical clinical structural and functional measures, including spectral domain OCT and fundus-guided microperimetry. High-resolution measures of macular structure and function were analyzed in eyes imaged at baseline and again 36 months later in patients with RD and age-similar, visually normal subjects. Structural measures of outer retinal health, including cone spacing from *en face* high-resolution images acquired with AOSLO and thickness of the IS and OS layers on SD-OCT scans, were compared with functional measures of visual sensitivity from fundus-guided microperimetry at identical retinal locations in normal eyes and in eyes with RD. The results may help improve current measures of detection and progression of RD to monitor the outcome of therapeutic interventions over 36 months.

3.3 Methods

3.3.1 Study design

This study was approved by the Institutional Review Boards of the University of California, San Francisco and the University of California, Berkeley, and adhered to the tenets of the Declaration of Helsinki. All subjects provided written informed consent.

3.3.2 Clinical examination

Best-corrected visual acuity (BCVA) and refractive error were measured according to the Early Treatment of Diabetic Retinopathy (ETDRS) study protocol (Ferris et al., 1982). Axial length was measured using partial coherence interferometry (IOL Master, Carl Zeiss Meditec, Dublin, CA, USA). Genetic testing was performed in 2 patients (40032 and 30007, respectively) as previously described (Biswas et al., 2017; Ratnam et al., 2013). Twelve patients (30015, 40023, 40030, 40039, 40043, 40046, 40064, 40067, 40070, 40079, 40080 and 40082) were tested using next-generation sequencing of 181 genes in a retinal dystrophy panel that included copy number analysis (Blueprint Genetics, San Francisco, CA) through the genetic testing study of the Foundation Fighting Blindness My Retina Tracker® registry for inherited retinal degenerative diseases (NCT 0245940).

3.3.3 SD-OCT data collection and cross-sectional thickness measurements

Spectral-domain optical coherence tomography (SD-OCT; Spectralis HRA+OCT system, Heidelberg Engineering, Vista, CA, USA) images analyzed included 20° or 30° horizontal and vertical cross section B-scans through the fovea. SD-OCT images were segmented manually to measure inner and outer segment (IS and OS) length at locations corresponding to regions of interest (ROIs) using custom software to measure inner and outer segment thickness at locations 0.1 degree apart (Hood et al., 2011; Birch et al., 2011; Hood et al., 2009; Wen et al., 2012; Wen et al., 2011; Aizawa et al., 2009). Examples of segmented horizontal OCT B-scans for an RD patient (40039) are shown in Figure 3.5.

3.3.4 Microperimetry analysis

Fundus-guided microperimetry was obtained as formerly described (Birch et al., 2011) (Nidek MP1, NAVIS software, ver. 1.7; Nidek Technologies, Fremont, CA, USA) under light-adapted conditions (32 cd/m^2) with spot size V (104 arcmin diameter, 1.73 degrees) delivered for 200ms under a 4-2-1 threshold strategy. With this staircase algorithm, threshold estimates are measured such that if the subject responds affirmatively that they can see the stimulus, the subsequent stimulus appears 4 dB dimmer, until a reversal occurs (where the patient responds negatively that they cannot see the stimulus) and then the stimulus appears 2 dB brighter until a second reversal occurs. Following the second reversal, the stimulus is adjusted by 1 dB until the third reversal at which point the threshold estimate is produced. A 3 degree diameter red ring was used as fixation target and patients were instructed to look in the center of the red ring after correcting for refractive error and presbyopia to focus the stimuli on the retina for each patient (Microperimeter MP1 Operator's Manual, Nidek Technologies Srl 2003-2016, page 23). Fundus-guided perimetric sensitivity was determined at locations spaced 2 degrees apart along the horizontal and vertical meridians through the fovea in the central 10 degrees surrounding fixation. To ensure the light-adapted measurement isolated cone function, sensitivity was determined with a long-pass dichroic filter (605 nm; NT30-634; Edmund Optics, Barrington, NJ, USA).

3.3.5 AOSLO image acquisition and cone spacing analysis

High-resolution images were acquired with Adaptive Optics Scanning Laser Ophthalmoscopy (AOSLO) and processed as described previously (Duncan et al., 2007; Ratnam et al., 2013; Talcott et al., 2011). Regions of interest (ROIs) were selected at locations within 5.7 degrees of the fovea at which unambiguous cones were visualized in AOSLO images acquired at baseline to improve the likelihood that the cones could be monitored longitudinally. For each subject AOSLO images were aligned with the near-infrared (NIR) SLO fundus images acquired with the SD-OCT and the microperimeter (Adobe Illustrator, Adobe, Inc., San Jose, CA, USA) to permit direct comparisons between measures of retinal structure and function (figure 3.1). Eight to twelve ROIs that aligned with the horizontal and vertical SD-OCT scans acquired through the fovea were selected from each AOSLO montage. For the present study, a subset of ROIs that corresponded to regions tested using MP1 stimuli, located within 1 degree of the center of a given MP1 location, were chosen for analysis in the present study. The average distance from the center of the ROI to the center of the region stimulated with the MP1 stimulus was 0.37 degrees (standard deviation 0.29, range: 0 - 1 degree), so most of the ROIs were well within the size of the MP1 stimulus. Cone spacing, or average nearest neighbor distance, was measured by 1-5 graders using a density recovery profile method (Rodieck 1991) with custom-written software, as previously described (Duncan et al., 2007; Menghini et al., 2014). The distance from the foveal center to the center of each ROI was measured in degrees. Cone spacing was measured in arcminutes and converted into Z-scores representing the number of standard deviations from the mean of 27 normal subjects (Chen et al., 2011) to control for eccentricity. For subjects imaged more than once, precise alignment of follow up images with baseline images ensured the same locations were measured and images were analyzed in random order.

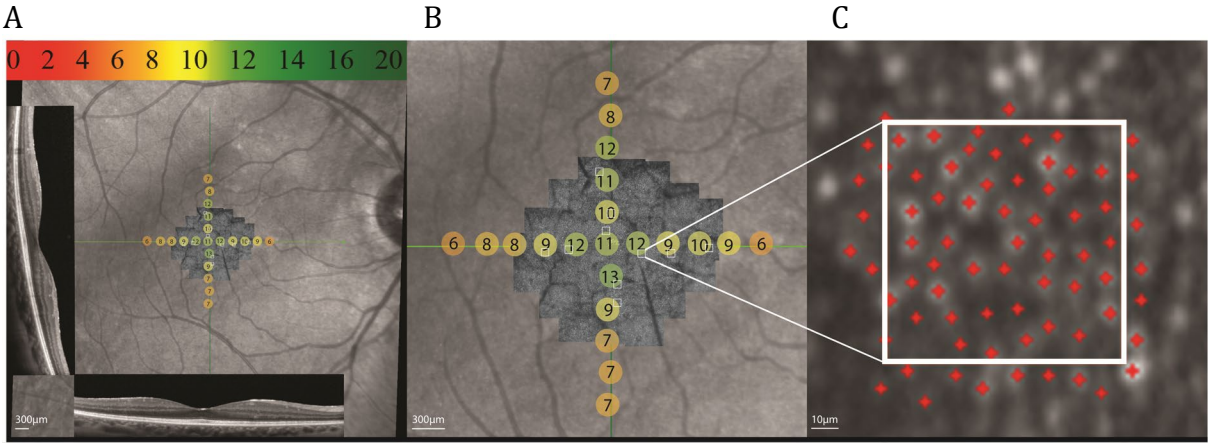

Figure 3.1. Adaptive optics scanning laser ophthalmoscopy (AOSLO) image, spectral domain-optical coherence tomography (SD-OCT) horizontal and vertical scans, and fundus-guided microperimetry map superimposed in patient 30015 OD. (A) Macular sensitivity values in color coded circles are shaded from green (normal) to red (stimulus not seen) based on the sensitivity measured at each location; color scale bar at top of panel; scale bar, 300µm. (B) Magnified view of (A); the regions of interest (ROIs) are outlined in white boxes; small white pixels indicate the patient's preferred retinal locus of fixation; scale bar, 300µm. (C) Magnified view of ROI N1. Red crosses indicate positions of cones used to assess cone spacing; scale bar, 10µm.

3.3.6 Comparisons for statistical analysis

For each patient, macular sensitivity and average IS and OS thickness at each ROI were compared to cone spacing Z-scores, controlling for visit year, using a Spearman correlation with bootstrap clustered by person to account for the fact that data from both eyes of some subjects were included. In addition, IS thickness and OS thickness were compared to sensitivity.

3.4 Results

3.4.1 Study subjects

Twenty-six eyes of 16 patients with RD and 16 eyes from 8 normal control subjects were studied at baseline (Table 3.1). Of those, 15 eyes of 14 patients with RD and 11 eyes from 6 visually-normal control subjects were studied longitudinally 36 months later (Table 3.2). Patient 40023 developed cystoid macular edema at 36 months which precluded reliable cone spacing measures at ROIs that were visible at baseline. RD patients 10048, 30007, 30015, 40030, 40032, 40043, 40046, 40064, 40067, 40070, 40079, 40080, 40082 participated in a clinical trial of an experimental treatment for RP which was administered to only one eye selected randomly for each subject after the baseline visit; treated eyes were excluded from analysis at 36 months and only the sham-treated eye was analyzed at the 36

month visit (labeled “study eye” in Table 3.1). One RD patient (40026) and 2 normal controls (10017 and 40048) left the study after completing the baseline visit but before completing the 36-month visit. The control subjects were age-similar (mean $\pm$ standard deviation = 46 $\pm$ 11.2 years) to, but slightly older than, the patients (mean $\pm$ standard deviation = 38 $\pm$ 10.5 years, t-test $P = 0.07$). The mean BCVA was better in the normal group (20/16) than in the patient group (20/20) (t-test $P < 0.0001$).

Table 3.1: Summary of clinical information for patients and normal control subjects in this study. AOSLO, adaptive optics scanning laser ophthalmoscopy; M, male; F, female; RP, retinitis pigmentosa; AD, autosomal dominant; AR, autosomal recessive; XL, X-linked; OD, right eye; OS, left eye; NGS, next generation sequencing genetic testing of 181 genes in retinal dystrophy panel; N/A, not available; * asterisk indicates study eye used (eye not specified to keep readers masked to the treated eye).

AOSLO ID	Sex	Age (years)	Diagnosis/Mutation	Eye	Baseline acuity	36 month acuity	Refractive error
10048	F	40	Multiplex RP/Unknown	OD	20/25	20/32*	-1.25+1.25x080
				OS	20/20		-1.25+1.25x120
30007	F	27	Usher syndrome type 3: homozygous *CLRN1* mutations c.144T>G, p.Asn48Lys (pathogenic)	OD	20/20	20/20*	-1.50+0.75x170
				OS	20/20		-0.75+0.50x030
30015	M	40	Simplex RP/*PRPH2* c.634A>G, p.Ser212Gly (likely pathogenic)	OD	20/20	20/20*	-2.75DS
				OS	20/20		-2.50DS
40023	M	34	Simplex RP/NGS: *PDE6B:* c.1624C>T, p.Arg542Trp and c.2140A>T, p.Met714Leu (both variants of uncertain significance)	OD	20/25	N/A	+0.50+1.25x118
				OS	20/25		plano+1.25x075
40026	F	28	Simplex RP/no genetic testing	OD	20/25	N/A	-1.25+0.25x075
				OS	20/20		-1.25+0.50x100
40030	F	40	Simplex RP/negative NGS	OD	20/16	20/13*	-3.75DS
				OS	20/16		-3.75DS
40032	M	30	ARRP: compound heterozygous *RPE65* mutations (c.1451G>A, p.Gly484Asp and c.746A>G, p.Tyr249Cys) and homozygous ABCA4 mutations (c.5882G>A, p.Gly1961Glu)	OD	20/25	20/25*	-3.75+4.00x092
				OS	20/20		5.00+4.25x080
40043	F	30	ARRP: compound heterozygous mutations in *USH2A* (c.2276G>T, p.Cys759Phe and deletion exons 12-16, c.(1971+1_1972-1)_(3316+1_3317-1)del) (pathogenic)	OD	20/20	20/20*	-1.75+1.00x090
				OS	20/20		-2.25+1.00x075
40046	M	62	Simplex RP/negative NGS	OD	20/20	20/20*	plano+0.50x082
				OS	20/25		plano+0.75x100
40039	M	45	ARRP: *USH2A*: c.2276G>T, p.Cys759Phe and c.2296T>C, p.Cys766Arg (pathogenic)	OD	20/20	20/20	-8.75+2.50x137
				OS	20/16	20/16	-7.25+1.25x040
40064	M	18	XLRP: *RPGR* hemizygous c.1243_1244delAG, p.Arg415Glyfs*27 (pathogenic)	study eye	20/25	20/25	-8.75+2.50x137
40067	M	42	Simplex RP, negative NGS	study eye	20/20	20/16	-0.50+0.00x000
40070	F	39	Simplex RP, *IFT140* c.634G>A, p.Gly212Arg (pathogenic) and c.1390G>T, p.Val464Leu (likely pathogenic); one inherited from each parent	study eye	20/16	20/20	-1.50+0.50x090
40079	M	53	ADRP: *PRPF31* c.1273 C>T, p.Gln425* (likely pathogenic)	study eye	20/16	20/20	-0.75+1.00x010
40080	M	30	XLRP: *RPGR* hemizygous c.28+5 G>A, splice donor site mutation 5bp from exon-intron boundary (likely pathogenic)	study eye	20/20	20/16	-4.25+0.50x090
40082	M	40	ARRP: *USH2A* c. 8522G>A, p.W2841 and c.11266 G>A, p.G3756S, (likely pathogenic);one inherited from each parent	study eye	20/25	20/25	-4.75+0.25x090
10017	F	31	Normal	OD	20/16	N/A	-0.25DS
				OS	20/16		-0.50DS
10023	M	57	Normal	OD	20/10	20/16	-1.00+1.00x025
				OS	20/13	N/A	-1.50+1.25x135
10033	M	57	Normal	OD	20/16	20/13	+0.25+0.50x135
				OS	20/16	20/13	+0.50+0.00x000
40048	M	51	Normal	OD	20/13	N/A	-0.50+0.50x075
				OS	20/16		-0.50+0.50x140
40053	F	37	Normal	OD	20/20	20/16	-0.75+0.25x168
				OS	20/13	20/16	-0.25+0.25x015
40054	F	24	Normal	OD	20/16	20/16	-0.25+0.00x000
				OS	20/16	20/16	-0.25+0.25x105
40055	M	50	Normal	OD	20/13	20/13	-0.25+0.00x000
				OS	20/16	20/13	-0.75+0.00x000
40061	M	50	Normal	OD	20/16	20/16	-1.50-1.75x015
				OS	20/16	20/13	-1.00+1.25x165

Table 3.2: Summary of clinical measures acquired on patients and normal subjects used in the current study. BL, baseline visit; 36mo, 36-month visit; OCT, optical coherence tomography; AOSLO, adaptive optics scanning laser ophthalmoscopy; MP1, fundus-guided microperimetry.

		OCT & AOSLO		MP1	
		BL	36mo	BL	36mo
Patients	# patients	16	14	9	9
	# eyes	26	15	13	10
Normals	# subjects	8	6	4	4
	# eyes	16	11	8	8

Due to a variety of causes, including patient drop out, relocation, or participation in a clinical treatment trial, not all eyes of all subjects studied with SD-OCT, AOSLO and MP1 at baseline were also imaged with these measures 36 months later. Similarly, not all subjects participated in the MP1 experiments, or the MP1 data was unreliable at both baseline and 36-month visits based on unstable fixation. Numbers of values for each of the analyzed measures are listed in Table 3.2.

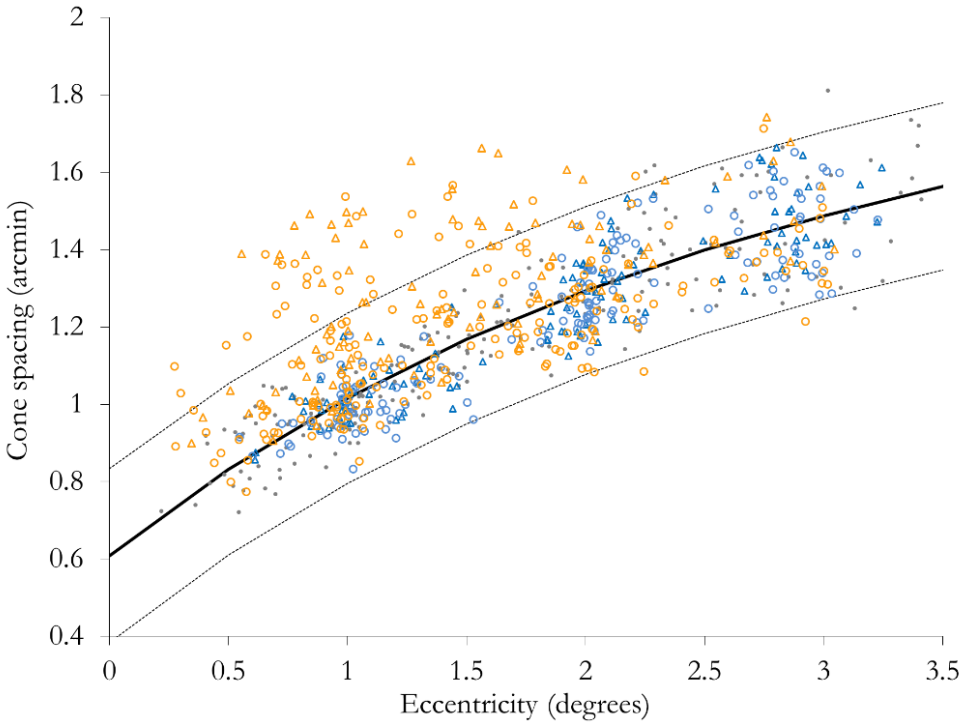

Figure 3.2. Cone spacing measures correlated with eccentricity as measured by distance from the fovea. The small black filled circles represent a normal data set composed of 27 controls (Chen et al., 2011). The dashed curved lines represent the 95% CI of this normal dataset, and the solid black line represents the mean. Normal subjects: *blue*; patients with RD: *orange*; circles: *baseline measures*; triangles: *36-month follow up measures.*

Figure 3. 2 presents eccentricity and cone spacing for all patients and normal subjects. Cone spacing measures and eccentricity were significantly correlated for patients (ρ = 0.57, 95%

confidence interval (CI): 0.37 to 0.79, P < 0.001) and normal subjects (ρ = 0.90, 95% CI: 0.87 to 0.92, P < 0.001). The average eccentricity of measurements was lower in patients (1.46 degrees) compared to normal subjects (1.87 degrees) (t-test *P* < 0.0001; figure 3.2). This is expected because retinal degeneration precluded measurement at greater eccentricities in some patients where cone loss extended within the region imaged using AOSLO.

3.4.2 Structural and functional correlations

Table 3.3: Summary of statistical analyses from this study. CI, confidence interval; Sig, statistical significance; Fig, figure; IS, inner segment; OS, outer segment; μm, microns; dB, decibels.

A. OCT thickness correlated with cone spacing

		Spearman's correlation ρ	95% CI	P-value	Fig.	Spearman's correlation ρ	95% CI	P-value	Fig.
		Cone spacing (arcmin)				Cone spacing (Z-scores)			
Normal subjects	IS thickness (μm)	-0.45	-0.56 to -0.32	<0.001	3A	-0.17	-0.31 to 0.011	0.068	3C
Patients		-0.50	-0.65 to -0.40	<0.001		-0.29	-0.61 to -0.090	0.002	
Normal subjects	OS thickness (μm)	-0.52	-0.67 to -0.36	<0.001	3B	-0.1	-0.30 to 0.12	0.36	3D
Patients		-0.59	-0.75 to -0.46	<0.001		-0.39	-0.81 to -0.19	<0.001	

B. OS and IS thickness correlated with sensitivity in normal eyes, but not RD patients

		Spearman's correlation ρ	95% CI	P-value	Fig.
		Sensitivity (dB)			
Normal subjects	IS thickness (μm)	0.18	0.006 to 0.43	0.047	4A
Patients		0.11	-0.25 to 0.38	0.60	
Normal subjects	OS thickness (μm)	0.36	0.27 to 0.61	<0.001	4B
Patients		0.30	-0.09 to 0.70	0.14	

C. Cone spacing correlated with sensitivity

		Spearman's correlation ρ	95% CI	P-value	Fig.
		Cone spacing (Z-scores)			
Normal subjects	Sensitivity (dB)	-0.22	-0.49 to -0.07	<0.001	4C
Patients		-0.38	-0.67 to -0.08	<0.001	

The correlations described below are summarized in Table 3.3. Cone spacing was significantly and negatively correlated with IS and OS thickness in patients and normal subjects (figures 3.3A-B, Table 3.3A). However, when cone spacing Z-scores were used to control for eccentricity, cone spacing Z-scores were not significantly correlated with IS or OS thickness in normal eyes, but cone spacing Z-scores were significantly and negatively correlated with IS and OS thickness in RD patients (Figure 3.3C-D, Table 3.3A).

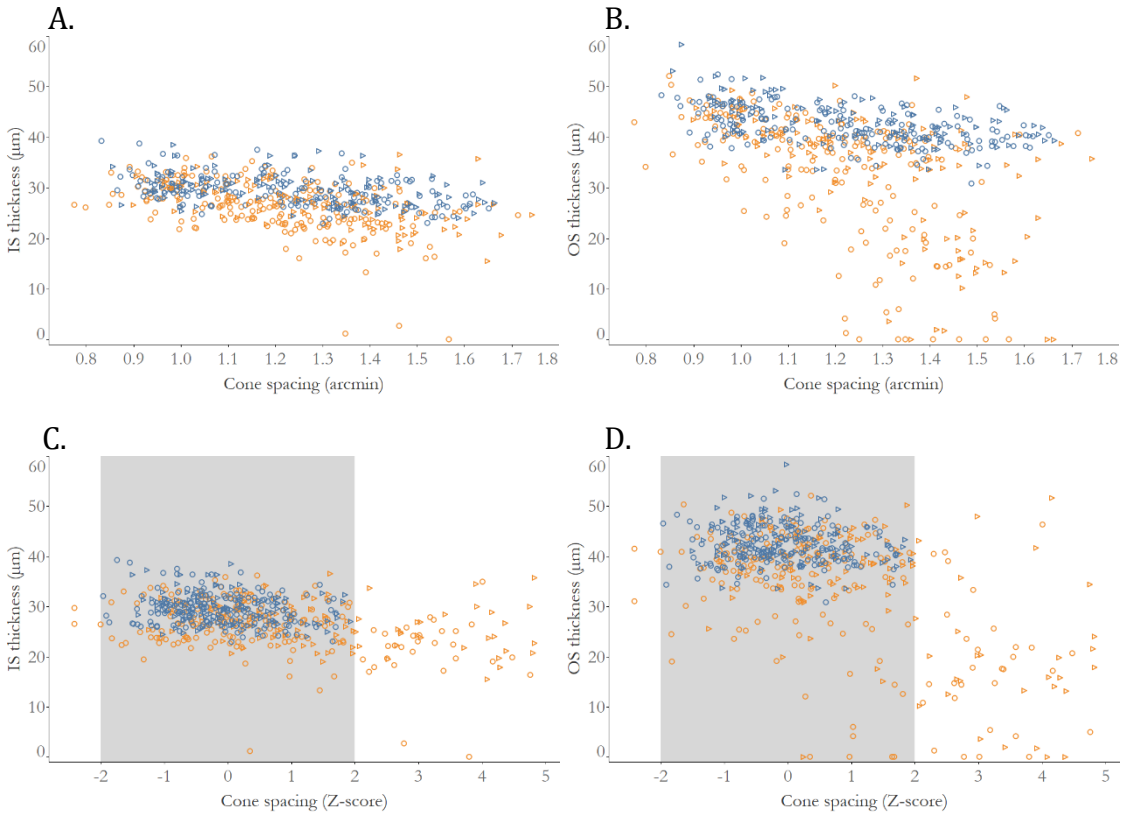

Figure 3.3: Outer retinal layer thickness correlated with cone spacing measures. (A) Inner segment (IS) thickness was significantly correlated with cone spacing in normal subjects and patients. (B) Outer segment (OS) thickness was significantly correlated with cone spacing in normal subjects and patients. (C) IS thickness was correlated with cone spacing Z-scores in patients, but not normal subjects. (D) OS thickness was correlated with cone spacing Z-scores in patients, but not normal subjects. Normal subjects: *blue*; patients with RD: *orange*; circles: *baseline measures*; triangles: *36-month follow up measures.* The gray bands on graphs C and D indicate the ±2 Z-score limits of normal subjects.

3.4.3 Functional correlations

Photoreceptor IS thickness and OS thickness were not significantly correlated with macular sensitivity in patients, but both were significantly correlated in normal subjects (figure 3.4A-B, table 3.3B); the correlation was positive, where reduced sensitivity correlated with decreased IS and OS thickness. Patients showed a trend in which reduced IS and OS thickness and sensitivity were observed; the small sample size and variability in sensitivity at regions with normal IS and OS thickness may have reduced the power to detect a significant correlation in patients. However, cone spacing Z-scores were significantly and negatively correlated with macular sensitivity in both normal subjects and patients (figure 3.4C, Table 3.3C), such that increased cone spacing Z-scores correlated with reduced sensitivity for both

normal subjects and patients. When cone spacing was greater than 2 standard deviations above the normal mean (Z-scores ±2), sensitivity was reduced (Figure 3.4C).

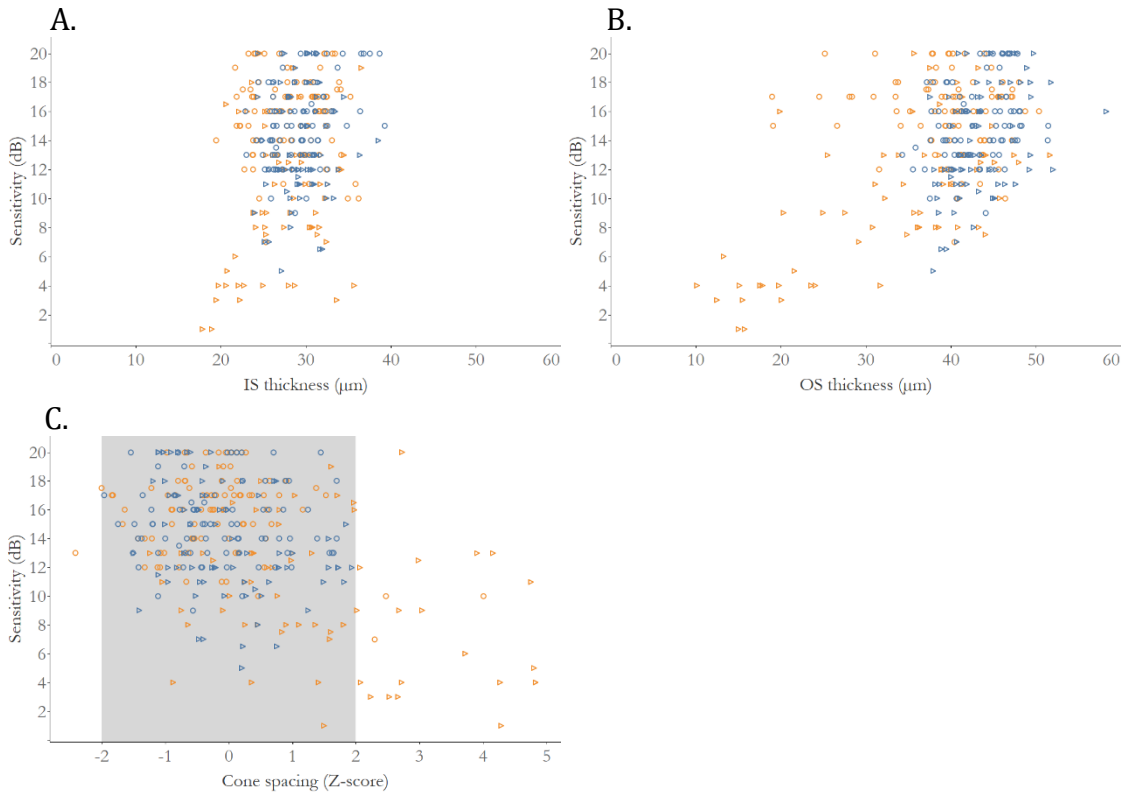

Figure 3.4: Correlation between outer retinal structure and macular function, measured as retinal sensitivity. (**A**) Retinal sensitivity was correlated with inner segment (IS) thickness in normal eyes, but not patients. (**B**) Retinal sensitivity was correlated with outer segment (OS) thickness in normal eyes, but not patients. (**C**) Retinal sensitivity was significantly correlated with cone spacing Z-scores in normal and patient eyes. Normal subjects: *blue*; patients with RD: *orange*; circles: *baseline measures*; triangles: *36-month follow up measures;* dB*: decibels*; the gray band in panel C indicates the ±2 Z-score limits of normal subjects.

3.4.4 Change from baseline to 36 months

Table 3.4: Summary of baseline vs. 36-month changes. The P-values for the comparisons were considered significant if less than 0.05.

	Mean difference	95% CI	P-value	Mean difference	95% CI	P-value	Mean difference	95% CI	P-value
	IS thickness (µm)			Cone spacing (arcminutes)			Sensitivity (dB)		
Normal subjects	0.78	-0.35 to 1.89	NA	0.014	-0.009 to 0.030	0.19	-1.4	-3.78 to 0.93	0.18
Patients	0.81	-0.36 to 2.04	0.17	0.1	0.059 to 0.14	<0.001	-3.74	-5.56 to -0.81	0.007
	OS thickness (µm)			Cone spacing (Z-scores)					
Normal subjects	0.66	-0.34 to 2.09	0.22	0.14	-0.06 to 0.27	0.14			
Patients	-0.66	-1.72 to 0.45	0.22	0.94	0.52 to 1.31	<0.001			

Comparing measures at baseline to 36 months, cone spacing increased significantly in patients by 0.10 arcminutes (95% CI: 0.059 to 0.14, $P < 0.001$), and cone spacing Z-scores increased significantly in patients by 0.94 (95% CI: 0.52 to 1.31, $P < 0.001$), but cone spacing did not change significantly in normal subjects. In addition, although there was no significant change in normal subjects, mean macular sensitivity decreased by -3.74 dB over 36 months (95% CI: -5.56 to -0.81, $P = 0.007$), indicating loss of macular function in RD patients. There was no significant change between baseline and 36 months in IS thickness or OS thickness in either patients or normal subjects. Baseline comparisons to measures at 36 months are summarized in Table 3.4.

A. B.

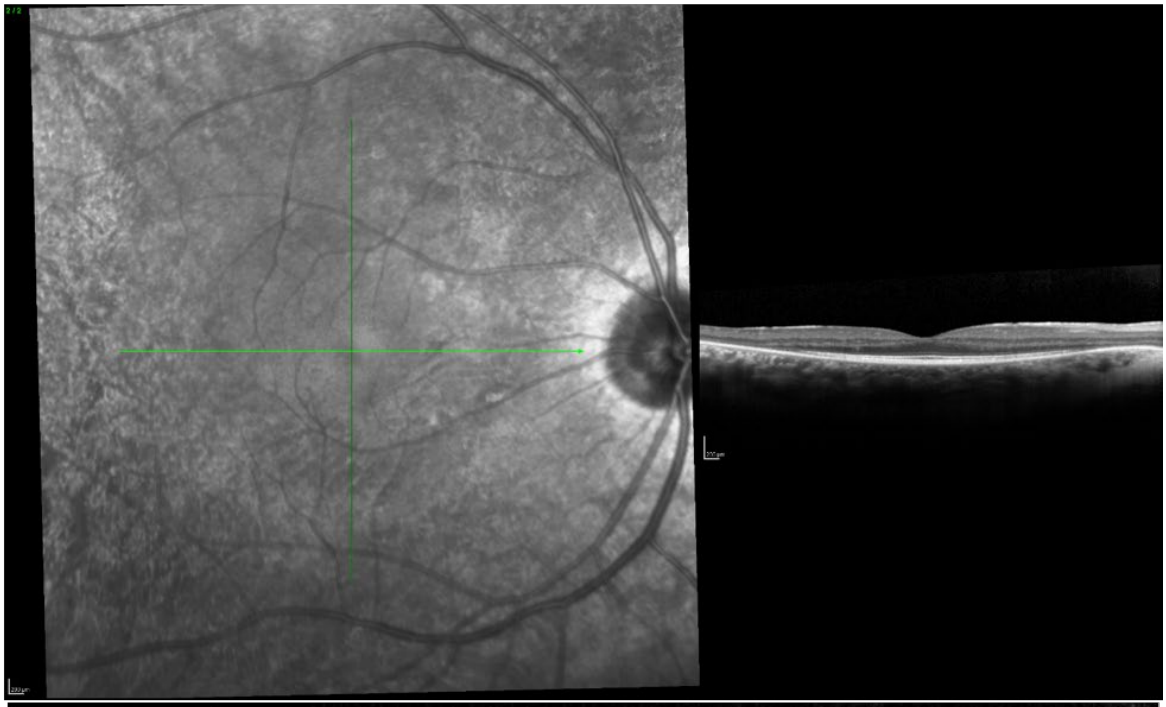

C.

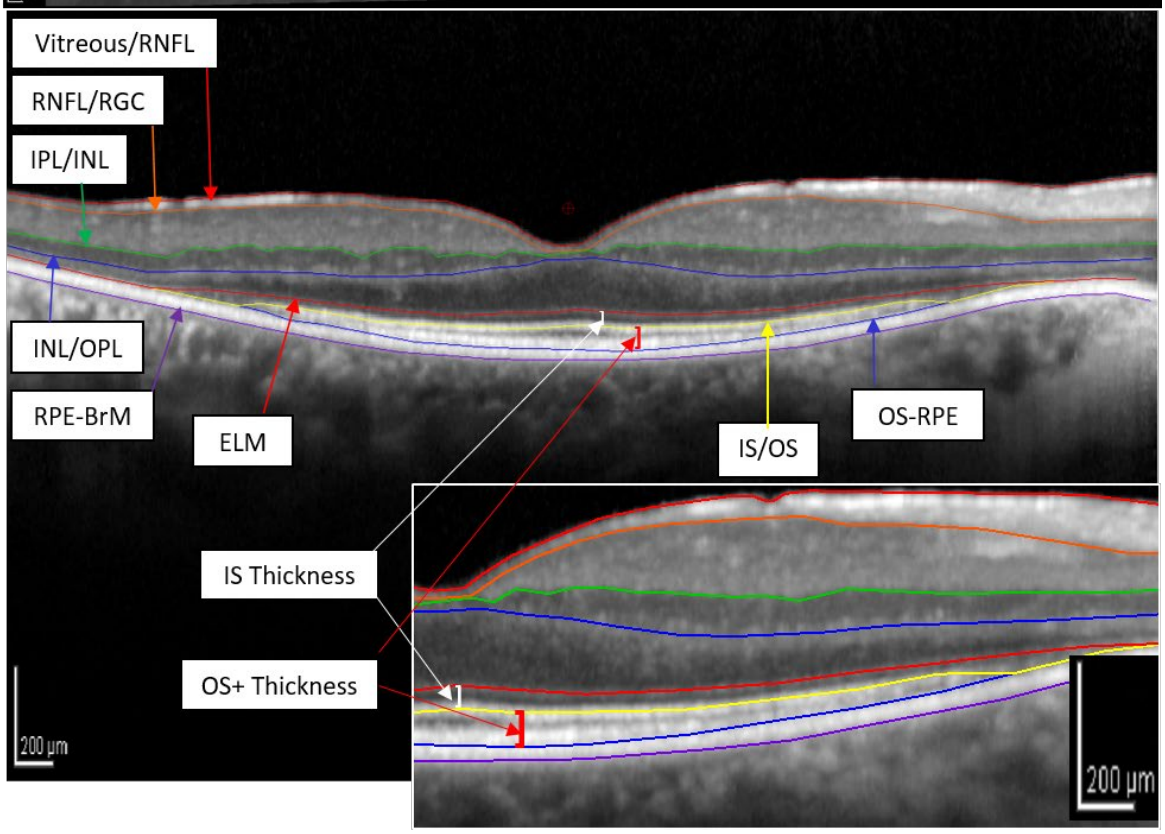
Vitreous/RNFL
RNFL/RGC
IPL/INL
INL/OPL
RPE-BrM
ELM
IS/OS
OS-RPE
IS Thickness
OS+ Thickness
200 µm
200 µm

Figure 3.5: Spectral Domain Optical Coherence Tomography Segmentation. A) Infrared fundus image of 40039, right eye, with light green line showing location of horizontal B-scan through fovea. B) Horizontal B-scan extends 20 degrees through the foveal center. C) The same scan as shown in (B) with interpolated boundaries based on manual segmentation of the retinal pigment epithelium -Bruch's membrane (RPE-BrM), outer segment-RPE (OS-RPE), inner segment/outer segment (IS/OS), external limiting membrane (ELM), inner nuclear layer-outer plexiform layer (INL/OPL), inner plexiform layer/inner nuclear layer (IPL/INL), retinal nerve fiber layer/retinal ganglion cell (RNFL/RGC), and vitreous/RNFL borders. IS thickness: black right bracket (]), OS+ thickness, red right bracket (]). The OS+ thickness layer includes the thickness of the outer segments and RPE cells.

3.5 Discussion

This study presents further evidence that structural cone measures using AOSLO images correlate with cross-sectional thickness measures of the IS and OS layers on SD-OCT (Makiyama et al., 2013; Wilk et al., 2014; Wilk et al., 2017). Both the IS and OS thickness were correlated with cone spacing measures in the present study of normal eyes and patients with RD; patients in the present study all had rod-cone dystrophy (RP or Usher syndrome type 3), so the results are most relevant for RP patients. However, the correlation of IS, OS and cone spacing with eccentricity from the fovea likely influenced the observed correlation between cone spacing and OCT measures, because IS and OS thickness was significantly correlated with cone spacing Z-score in patients, but not normal subjects, when eccentricity was accounted for using Z-scores. The negative correlation between cone spacing Z-scores and both IS and OS thickness indicates that cone spacing Z-scores increase while outer retinal layer thickness decreases. The difference in correlation strength between OS thickness and cone spacing Z-scores versus IS thickness and cone spacing Z-scores may be related to the sequence in which cone photoreceptors degenerate in patients with RP: OS are the earliest affected, then IS are lost, and the nuclei of cone photoreceptors in the outer nuclear layer are last to degenerate (Milam et al., 1998; Lazow et al., 2011). The variation in OS thickness in patients observed in figure 3.3B and 3.3D likely reflects inclusion of patients at different stages of degeneration, with some retaining longer photoreceptor OS while having normal cone spacing Z-scores, but many with shorter OS showing abnormal cone spacing normal Z-scores.

The correlation between IS and OS thickness and sensitivity was only significant in normal subjects. We anticipated that OS thickness would correlate with sensitivity since the OS contain the photoreceptor disc structures that are responsible for phototransduction. However, sensitivity in RD patients was variable, likely due at least in part to inclusion of a genetically heterogeneous population. Some of the mutations associated with RP in the present study such as *PRPH2* are associated with long OS (Duncan et al., 2011), while others such as *PDE6B* affect phototransduction (McLaughlin et al., 1993), or the retinoid cycle, such as *RPE65* (Cai et al., 2009), each of which may affect sensitivity of photoreceptors with different OS thickness differently. Analysis of macular function using fundus-guided microperimetry in a genetically homogeneous patient population may provide clearer insight into the relationship between structure and function in the macula of RD patients.

Macular sensitivity using similar experimental conditions to the present study reported large variability in sensitivity for both patients and normal subjects (Birch et al., 2011). The lack of significant correlations between sensitivity and IS or OS thickness in RD patients is likely due to the insensitivity of fundus-guided perimetric stimuli in detecting subtle changes in visual loss, due to the variability observed in microperimetric responses and coarse resolution of fundus-guided microperimetric visual function tests. In another study using fundus-guided microperimetry to study macular function in patients with X-linked RP, with a slightly different protocol using white stimuli which might have allowed for a mixed rod-cone response, variability was seen as well (Acton et al., 2013). In that study, mean sensitivity values across visual field spanned from 1-20 dB with a mean value of 13.1 [standard deviation (SD) 4.5] dB in patients, whereas the age-matched normal subject values ranged from 5-20 dB with an average of 14.6 [SD 3.3] dB (Acton et al., 2013). The current study used a red filter to deliver red stimuli to optimize cone responses and minimize rod activation since rods are relatively insensitive to longer wavelengths (Bowmaker et al., 1980). However, the use of a red filter might contribute to greater variability in threshold responses, because the task is more difficult. Another study using the same light-adapted test with red stimuli as used in the present study also reported a wide range of sensitivity values spanning across the central visual field (Birch et al., 2011).

The current study provides evidence of a correlation between cone spacing Z-scores and macular sensitivity in patients with RD. Although there is a wide range of sensitivity values among the ROIs with Z-scores less than 2, ROIs with Z-score greater than 2 show reduced sensitivity (figure 3.4C). This provides further evidence that substantial photoreceptor loss is required before it is possible to observe significant decreases in visual function. The current study is aligned with previous studies which showed that areas of greater photoreceptor loss show stronger correlations with functional measures, including contrast sensitivity with parafoveal cone density (Huang et al., 2014) and visual acuity with cone spacing Z-scores within 1 degree of the foveal center (Ratnam et al., 2013; Foote et al., 2018).

The present study demonstrated significantly increased cone spacing at 36 months compared to baseline in RD patients, measured both in arcminutes and as Z-scores to account for eccentricity. Cone spacing did not change significantly in normal eyes over this 36 month study. Although there was no significant change between baseline and 36 months in IS or OS length, macular sensitivity decreased significantly in patients, but not in normal eyes. Due to cone photoreceptor degeneration, particularly in the patients studied in the current manuscript with RP and Usher syndrome type 3, a decrease in sensitivity over a period of 36 months is expected and coincides with increased cone spacing or cone loss. Nevertheless, the current study was limited in the number of subjects with sensitivity data at both baseline and 36 months, and larger, prospective studies incorporating fundus-guided microperimetry may demonstrate macular sensitivity to be an even more sensitive outcome measure of disease progression (Birch et al., 2011). Some of the variability in sensitivity measures may be due to discrepancy in background luminance measurements of the liquid crystal display (LCD) used by the fundus-guided microperimetry system used in the present study (Springer et al., 2005), which has not been observed using other systems which use a super luminescent diode in place of the LCD (MAIA, CenterVue, Inc., Fremont, CA, USA) (Wong et al., 2016). In addition, fundus-guided microperimetry with commercially-available

systems does not have resolution commensurate with measures of retinal structure from SD-OCT or AOSLO images. Microperimetry with single cell resolution may improve evaluation of the earliest functional changes in photoreceptor survival. Adaptive Optics Microperimetry (AOMP) enables the precise delivery of visual stimuli to individual cone photoreceptors with a delivery error of 0.89 arcmin (Tuten et al., 2012) which is less than the cone-to-cone spacing Z-scores at all eccentricities beyond 1 degree, and is approximately 5.5 times better than tracking errors of the system used in the present study (Tuten et al., 2012). Future studies will use AOMP to investigate the relationship between cone spacing Z-scores, IS and OS thickness and visual sensitivity with this more precise measure of function.

3.6 Summary

In conclusion, objective measures of photoreceptor structure such as cross-sectional measures of IS and OS thickness, and cone spacing Z-scores, were significantly correlated with visual function in patients with retinal degeneration. Cone spacing increased and microperimetry decreased significantly over 36 months in RD patients. These correlations observed suggest that high resolution images of cone structure can be used to assess patients with RD longitudinally. Furthermore, these correlations between structural measures and visual function prove they may be appropriate outcome measures for clinical trials.

3.7 Acknowledgements

The efforts described in this chapter was published as a peer-reviewed manuscript in *Investigative Ophthalmology & Visual Science* in February 2019. Citation:
Foote KG, De la Huerta I, Gustafson K, Baldwin A, Zayit-Soudry S, Rinella N, Porco TC, Roorda A, Duncan JL. Cone Spacing Correlates With Retinal Thickness and Microperimetry in Patients With Inherited Retinal Degenerations. Investigative ophthalmology & visual science. 2019 Mar 1;60(4):1234-43.

Dr. Jacque Duncan (Department of Ophthalmology, University of California, San Francisco) provided instrumental contributions to the conception, design, implementation, interpretation, and analysis of this study. Dr. Austin Roorda (School of Optometry, University of California, Berkeley) provided vital support in examination and reporting of the work in this study. The work that went into this project would not have been possible without co-author Irina De la Huerta who presented a preliminary version of this study at the 2016 Association for Research in Vision and Ophthalmology (Seattle, Washington) conference. Assistance with data collection and processing was provided from co-authors Kevin Gustafson, Angela Baldwin, Shiri Zayit-Soudry, and Nicholas Rinella. Co-author Travis Porco is thanked for his assistance with the statistical analysis. Pavan Tiruveedhula is credited for the implementation and technical knowledge and support of the hardware and software systems of the AOSLO system. Much gratitude is given to these collaborators for their contributions as well as permission to include the work in this chapter.

CHAPTER 4: Cone structure persists beyond margins of short-wavelength autofluorescence in choroideremia

4.1 Abstract

Purpose: To study the relationship between structure and function of the choriocapillaris (CC), retinal pigment epithelium (RPE) and photoreceptors in patients with choroideremia (CHM).

Methods: 6 CHM patients (12 eyes) and 4 normal subjects (6 eyes) were studied with fundus-guided microperimetry, confocal and non-confocal adaptive optics scanning laser ophthalmoscopy (AOSLO), near-infrared and color fundus photos, short wavelength fundus autofluorescence (SW-AF) and swept-source optical coherence tomography (SS-OCT) and angiography (SS-OCTA) images. Cone spacing varies with eccentricity and was represented using Z-scores (standard deviations from the mean). CC flow voids were defined using a threshold of one standard deviation below the mean from a normal database.

Results: Cone spacing, expressed as Z-scores, was not significantly correlated with distance from the margin of preserved RPE, determined using either the SS-OCT or SW-AF scans. Cone spacing was significantly correlated with CC flow voids and retinal sensitivity. Flow voids were greater than normal in regions of preserved RPE and increased progressively from -2° inside the edge of the preserved area to +2° beyond the edge. Visual sensitivity decreased as CC flow voids increased approaching and beyond the edge of preserved structure.

Conclusions: In CHM, cone spacing correlated with CC flow voids, and was inversely correlated with retinal sensitivity, suggesting cone degeneration accompanied reduced CC perfusion. Using SS-OCT instead of SW-AF to identify the border of preserved outer retinal structure demonstrated functional cones beyond the border defined by SW-AF, which may underestimate regions of preserved outer retinal structure with cells that may be amenable to treatment.

4.2 Introduction

Choroideremia (CHM) is an X-linked inherited degenerative disease estimated to affect 1:50,000 and is caused by a mutation in the CHM (REP1) gene on chromosome Xq21 (Aleman et al., 2017). Patients present with progressive loss of night vision, peripheral visual field loss and eventual central vision loss. Although the pathogenic mechanism underlying degeneration in CHM is not clearly understood, it may be due to reduced function of proteins that play a role in organelle formation and vesicle trafficking (Coussa and Traboulsi 2012).

CHM leads to degeneration of the choriocapillaris (CC), retinal pigment epithelium (RPE), and photoreceptors, but the temporal relationship in which different cell types are affected remains unclear. Studies of induced pluripotent stem cells (iPSCs) derived from CHM patients and differentiated into RPE cells demonstrate abnormal trafficking of melanosome granules to the apical surface and abnormal phagocytosis, which may cause photoreceptor

degeneration (Duong et al., 2018). However, RPE cells studied in isolation may not accurately reflect cellular function *in vivo*. The lack of animal models of CHM makes clinical characterization of CHM patients especially valuable, and advances in fundus imaging modalities permit assessment of photoreceptors, RPE and choroidal structures with high-resolution (Aleman et al., 2017; Morgan et al., 2014; Syed et al., 2013). Structural studies using a combination of SD-OCT, confocal and non-confocal split-detector adaptive optics scanning laser ophthalmoscopy (AOSLO) techniques (Sun et al., 2016) and OCT angiography (OCTA) imaging (Gao et al., 2017; Jain et al., 2016; Parodi et al., 2019) suggest that RPE cells degenerate before the CC, and that the CC does not degenerate independently of RPE loss (Parodi et al., 2019). Functional studies using OCT and psychophysical tests have demonstrated loss of photoreceptor function first, perhaps independently or in conjunction with RPE depigmentation (Aleman et al., 2017; Duncan et al., 2002; Jacobson et al., 2006). To date, few published reports have compared retinal function with structure using high-resolution retinal imaging (Morgan et al., 2018; Tuten et al., 2019). The use of high-resolution imaging approaches may provide insight into how cells are affected during retinal degeneration in patients with CHM.

Fundus autofluorescence images are commonly used to assess RPE structure in living eyes, including patients with CHM (Birtel et al., 2019). Short wavelength autofluorescence (SW-AF) signals from bisretinoid constituents are naturally exhibited by photoreceptor outer segments and RPE cells when excited by an external light source (Sparrow et al., 2012). When photoreceptor outer segments incompletely degrade due to disease, excess lipofuscin accumulates in RPE cells, which appear hyperfluorescent in AF images (Schmitz-Valckenberg al., 2008). SW-AF SLO imaging uses a confocal pinhole to image light from a single plane, reducing noise from structures other than the retina that may contain fluorophores (Sparrow al., 2018). Near-infrared autofluorescence (NIR-AF) images use 787 nm laser diode for excitation with a barrier filter allowing light >810 nm to pass, and images fluorophores that are most likely derived from melanin pigment (Weinberger al., 2006). NIR-AF imaging is more comfortable for patients and may pose less risk of RPE damage than SW-AF (Cideciyan al., 2007; Cideciyan et al., 2015). NIR-reflectance (NIR-REF) imaging has been shown to be strongly correlated with NIR-AF imaging and uses wavelengths similar to the light used to acquire infrared fundus images during OCT scans, which suggests that the sources of signals from OCT images may be similar to the sources of NIR-REF and NIR-AF images (Weinberger al., 2006).

Recent studies of CC perfusion using OCTA and SW-AF have shown normal CC flow until RPE loss occurred (Parodi et al., 2019), and more extensive RPE loss than CC nonperfusion, which in turn was larger than the area of retinal vascular nonperfusion (Jia et al., 2015). Recent publications have reported differences in NIR-AF with SW-AF images other inherited retinal degenerations including Stargardt disease and CHM patients (Duncker et al., 2014; Paavo et al., 2018). NIR-AF images demonstrate larger areas of RPE atrophy and correlate more closely with the ellipsoid zone (EZ) extent than SW-AF images in Stargardt disease patients (Duncker et al., 2014).

Signals from the RPE cell structure monolayer can also be visualized using OCT imaging; OCT is a non-invasive imaging technique used to image the fundus layers in cross-section (Huang

et al., 2014; Podoleanu et al., 2008). Swept-source OCT (SS-OCT) images use 1050 nm light to provide deeper penetration to visualize the RPE and choriocapillaris (Jia et al., 2015; Zhang et al., 2017; Zhang et al., 2018). When SS-OCT *en face* slabs are used to observe the RPE layer, the signal comes from RPE melanin (Greenstein et al., 2017). To clarify the relationship between outer retinal structure and function and extend prior studies (Morgan et al., 2018; Tuten et al., 2019), we compared multimodal high-resolution studies of photoreceptor, RPE and choroidal structure with photoreceptor function in patients with CHM.

4.3 Methods

4.3.1 Study design

Research procedures followed the tenets of the Declaration of Helsinki. Voluntary informed consent was obtained from all subjects. The study protocol was approved by the Institutional Review Boards of the University of California, San Francisco and the University of California, Berkeley.

4.3.2 Subjects

Twelve eyes of 6 CHM patients with average age of 37 ± 19.2 years and 6 eyes of 4 healthy subjects with normal eye examinations with average age of 33 ± 11.6 years were studied; there was no significant difference in the ages of patients and normal subjects (t-test, P = 0.35) (Table 4.1). The patients and subjects were from unrelated families, with the exception of patients 30025 and 10040 who were father and daughter (Syed et al., 2013), respectively. Patient 30025 was excluded from the cone spacing analyses due to poor image quality and retinal sensitivity analyses because the patient could not see the fixation target to perform micropermetry reliably. Five patients were male, and one patient (10040) was a symptomatic carrier female with 100% X-inactivation, previously described (Syed et al., 2013). Normal control subjects had no evidence of retinal degeneration on complete eye examination or fundus images and did not undergo genetic testing. Patients were excluded from the study if they had conditions that would affect imaging including nystagmus, cataract, and macular edema. Genetic testing was performed on patients through the Carver Nonprofit Genetic Testing Laboratory on a fee-for-service basis (40135), the eyeGENE research consortium (EyeGENE 2009; Blain et al., 2013; Brooks et al., 2008; Goetz et al., 2012) or using a next-generation sequencing panel through the My Retina Tracker® registry genetic testing study (NCT 02435940) (retinal dystrophy panel of 181 genes, Blueprint Genetics, San Francisco, CA, USA).

ID	Sex	Age	Diagnosis/Mutation	Eye	BCVA	Refractive Error
10040	F	36	*CHM* c.49+1G>A, splice site mutation, exon 1	OD	20/25	-2.00
				OS	20/25	-2.95
30025	M	75	*CHM* c.49+1G>A, splice site mutation, exon 1	OD	20/80	-1.50+0.25x180
				OS	20/80	-2.00+0.25x040
40028	M	22	*CHM* c.316 C>T, p.Gln106Stop	OD	20/25	-2.25+1.75x180
				OS	20/25	-1.25+1.50x170
40135	M	45	*CHM* IVS2+1 G>A, aberrant mRNA splicing	OD	20/30	-3.25
				OS	20/30	-3.25
40147	M	26	*CHM* c.1770+2T>A, splice donor variant	OD	20/25	-1.00+.025x005
				OS	20/20	-1.50+0.25x160
40166	M	18	*CHM* c.715 C>T, p.Arg239Stop	OD	20/32	-6.00+4.00x095
				OS	20/32	-6.00+4.00x080
10003	M	52	Normal	OS	20/16	0.00+0.50x180
40104	M	26	Normal	OD	20/16	plano
				OS	20/16	plano
40154	F	22	Normal	OD	20/16	+2.50
				OS	20/20	+1.50+0.05x152
40179	F	31	Normal	OD	20/20	+0.25+1.00x20

Table 4.1: Clinical characteristics of healthy normal subjects and patients with CHM; CHM, choroideremia; F, female; M, male; BCVA, best corrected visual acuity; OD, right eye; OS, left eye.

4.3.3 Fundus-guided microperimetry

Fundus-guided microperimetry using Macular Integrity Assessment software (MAIA, Centervue Inc., Fremont, CA) was used in this study to analyze macular sensitivity of patients with CHM. This instrument uses scanning laser ophthalmoscopy (SLO) with real-time fundus tracking at a rate of 25 frames/second using fundus landmarks as a reference for perimetry and has good repeatability (Chen et al., 2009). The MAIA uses a superluminescent diode of 850 nm and scans with 1024 x 1024 pixel sampling resolution over a 36 x 36 degree field of view. Goldman III (26 arcmin, 0.43°) stimuli were presented for 200 ms on a 1.27 cd/m^2 background with a dynamic range of 36 dB (Crossland et al., 2012; Dimopoulos et al., 2012). A standard 4-2 strategy with a custom grid pattern extending every 1° from the central fixation out to 10° in the 4 cardinal directions was used. In addition, the grid pattern covered every 1° within the central 6°.

4.3.4 Confocal and split detector AOSLO

We used a simultaneous confocal and non-confocal split detector imaging AOSLO system. Confocal imaging is an *in vivo*, non-invasive technique that records light emerging from the cone waveguide, comprised of scattered light from the IS/OS junction and the posterior tip of the outer segment (Miller et al., 1996; Roorda and Duncan 2015). Non-confocal split

detector AOSLO (Scoles et al., 2014) uses a reflective mask with an annulus in the image plane in place of a regular pinhole typically used for confocal detection. This method allows the confocal signal to be reflected into one detector, and then directs the multiply scattered, non-confocal light from opposing sides of the annular aperture into two separate detectors. The split detector signal is calculated as the difference between the two non-confocal detectors divided by their sum (Scoles et al., 2014). Non-confocal split detector AOSLO is a type of phase-contrast imaging and can be especially useful in distinguishing areas where cone inner segments remain but outer segments are not waveguiding (Scoles et al., 2014).

4.3.5 Cone spacing

Montages of AOSLO images were created as previously described (Duncan et al., 2007) and with automontaging software (Chen et al., 2016). To identify the preferred retinal locus (PRL), a 10 second video was recorded as the patient observed a small circular fixation target delivered through modulation of the AOSLO scanning raster, whose location was recorded in the AOSLO video (Poonja et al., 2005). The mean and standard deviation (SD) of locations of fixation points in both horizontal and vertical directions were registered using custom image analysis tools made using MATLAB (The MathWorks, Inc., Natick, MA). The PRL was used to define the foveal center for measures of eccentricity. Cone spacing measures were quantified using a density recovery profile method (Rodieck 1991) as described previously (Duncan et al., 2007). This method was chosen to estimate cone spacing since it allows for reliable estimates of cone spacing in mosaics where not all cones are clearly visible, and where cones are not closely packed into a hexagonal array. While other measures of cone spacing exist (like nearest neighbor distance or row-to-row spacing) (Cooper et al., 2016) we chose to use cone spacing as a conservative measure of cone preservation, albeit perhaps an insensitive measure of cone loss.

Cone spacing was measured by 2 independent graders within a standardized 0.1 degree^2 (42×42 pixel) box as described previously (Foote et al., 2018, Chapter 2.3 of this document). Cone spacing measures were made in regions with the clearest cone images that were as close as possible to the retinal locations where functional measures were acquired using the MAIA microperimetry, which were manually superimposed on AOSLO images (Adobe Illustrator; Adobe, Inc., San Jose, CA, USA). Average intraclass correlation coefficient ICC value for both patients and normal subjects between the 2 graders was 0.91. Because cone spacing varies predictably with eccentricity from the fovea (Chui et al., 2008; Curcio et al., 1990), Z-scores, or standard deviations from the normal mean at the location where the cone spacing was measured, were used to describe cone spacing and control for the effect of eccentricity on cone spacing measures.

4.3.6 Fundus Autofluorescence (FAF)

In this study, SW-AF images (i.e. FAF) were acquired using *in vivo* confocal scanning laser ophthalmoscopy (SLO) (Spectralis HRA+OCT; Heidelberg Engineering, Vista, CA) with 488 nm excitation and a 500 nm barrier filter to block reflected light and permit autofluorescent light from the fundus to pass through (Schmitz-Valckenberg al. 2008). Hyperfluorescent

areas representing areas of preserved RPE cells on SW-AF images were manually outlined using Photoshop CC (Adobe, San Jose, CA). The current study compared boundaries of preserved outer retina and RPE using SW-AF, and *en face* SS-OCT slab analyses (figure 4.1).

4.3.7 Swept-Source Optical Coherence Tomography and Angiography

A SS-OCT (PLEX Elite 9000, Carl Zeiss Meditec Inc., Dublin, CA) was used to visualize and semi-automatically identify borders of preserved RPE from *en face* slabs extending from the outer boundary of the outer plexiform layer (outer retina) to 8 μm beneath Bruch's membrane (Zhang et al., 2017). The SS-OCT has a swept source tunable laser centered between 1040-1060 nm which can scan up to 100,000 A-scans/second with an optical axial resolution of 6.3 μm (PLEX Elite 9000 User Manual 2016; Akman 2018).

SS-OCTA was used to visualize the CC *in vivo* from an *en face* slab extending from the outer boundary of Bruch's membrane to 20 μm beneath Bruch's membrane (Zhang et al., 2018). CC perfusion can be measured as flow voids (FV), defined as a percentage of the imaged region representing CC flow void with a reduction of pixel intensity (figure 4.2), one standard deviation below the mean CC flow from a normative database of 20 normal subjects aged 20-39 years old (Zhang et al., 2018). In figure 4.2, the black or blue contour represents the boundary of the preserved region (as defined by SW-AF or SS-OCT respectively) and the white contours indicate regions at 1 degree and two degrees inside and outside the boundary, respectively. In the innermost region 1 (delimited by the white contour 2 degrees inside the boundary) the flow void pixels are green; in the outermost region 6 (outside the outer white contour), the flow void pixels are black. In the other regions 2-5 delimited by the white contours and black boundary, the flow void pixels are colored in blue, yellow, red, and purple, respectively.

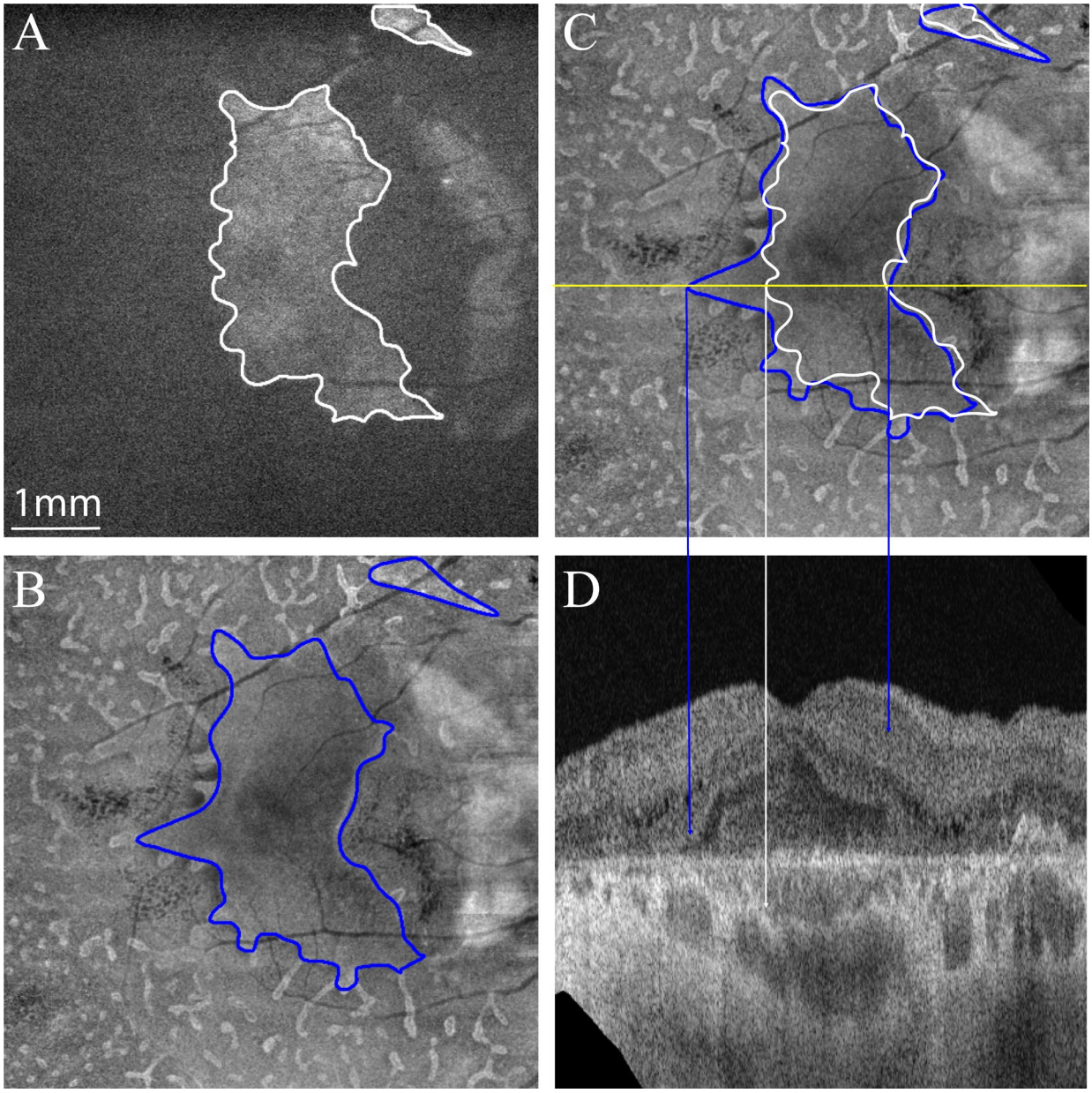

Figure 4.1. Outer retinal/retinal pigment epithelial (RPE) borders from the right eye of patient 40028. (A) Short-wavelength autofluorescence (SW-AF) image with the edge of preserved RPE manually outlined in white; (B) Swept source optical coherence tomography (SS-OCT) *en face* image of outer retina-RPE-choriocapillaris (CC) slab extending from the outer plexiform layer to 8 um beneath Bruch's membrane with the edge of the preserved RPE outlined in blue; (C) Outlines from (A) and (B) superimposed; the yellow horizontal line shows the area from which the B-scan shown in panel (D) is taken, white vertical lines correspond to the areas of preserved RPE based on SW-AF scans, while vertical blue lines show the area of preserved outer retina-RPE-choriocapillaris based on SS-OCT scans; (D) B-scan that corresponds to *en face* image in (C). Scale bar: 1mm (as estimated by PLEX Elite 9000, Carl Zeiss Meditec Inc.).

R1=4.12%
R2=5.12%
R3=9.05%
R4=14.6%
R5=25.7%
R6=34.8%

R1=3.79%
R2=4.77%
R3=12.3%
R4=18.5%
R5=28.2%
R6=34.4%

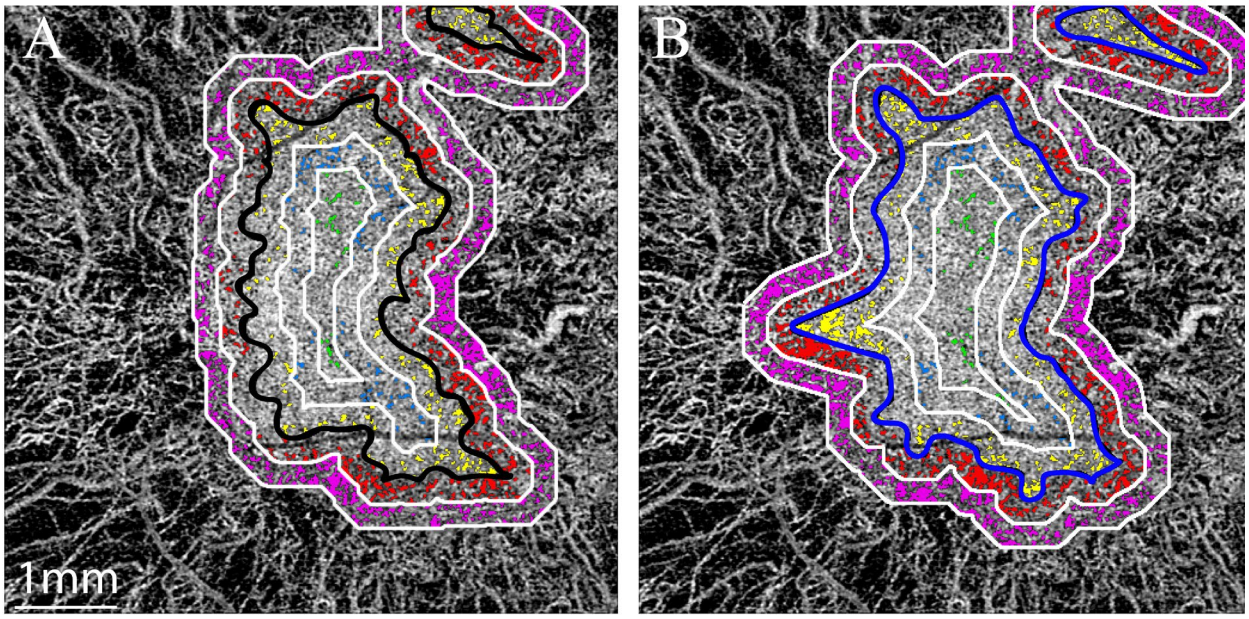

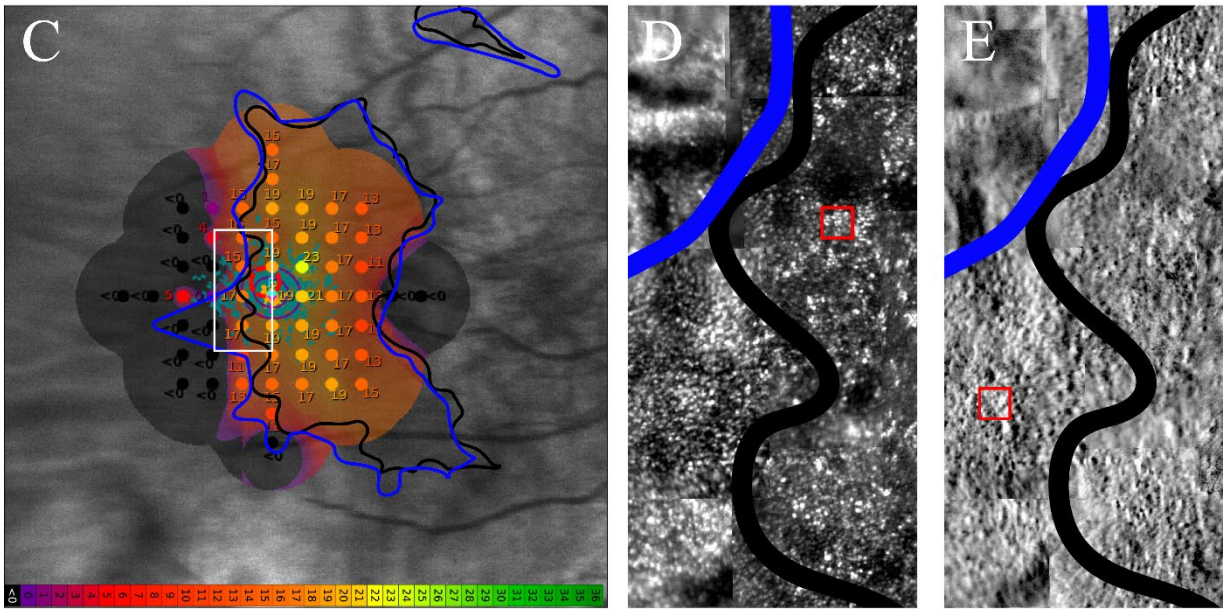

Figure 4.2. Multimodal images of structure and function from the right eye of patient 40028. (A) Swept source optical coherence tomography (SS-OCTA) choriocapillaris (CC) slab with percent flow void (% FV) shown in regions (R) 1-6 with SW-AF border outlined in black; (B) SS-OCTA CC slab with % FV shown in regions (R) 1-6 with SS-OCT border outlined in blue; (C) fundus-guided microperimetry retinal sensitivity image with SW-AF border in black and SS-OCT border in blue; the color coded bar shows the dynamic range, white box represents area in (D) and (E); (D) Confocal AOSLO image shows waveguiding cones with blue SS-OCT and black SW-AF borders superimposed; (E) Split detector AOSLO image shows cone inner segments, same lines superimposed as in (D). (D) and (E) show cones beyond the margin defined by short-wavelength autofluorescence (SW-AF). For (D) and (E) red boxes indicate select regions of interest (ROIs) where cone spacing is measured. Scale bar for (A)-(C): 1mm (as estimated by PLEX Elite 9000, Carl Zeiss Meditec Inc.).

4.3.8 Statistical methods

Descriptive statistics were calculated with means and standard deviations. Spearman correlation coefficients were calculated, with 95% confidence intervals (CIs) derived from bootstrap resampling at the patient level.

4.4 Results

Histological studies have demonstrated a strong relationship between eccentricity from the fovea and cone spacing (Chui et al., 2008; Curcio et al., 1990). In the present study, cone spacing was significantly correlated with eccentricity for patients ($\rho = 0.89$, 95% CI: 0.79 to 0.95) and normal subjects ($\rho = 0.97$, 95% CI: 0.95 to 0.99); figure 4.3A. To evaluate the relationship between cone spacing and visual function at the same locations where cones were measured, we compared cone spacing with retinal sensitivity and found a significant, negative correlation for patients ($\rho = -0.29$, 95% CI: -0.40 to -0.07) and normal subjects ($\rho = -0.15$, 95% CI: -0.44 to -0.009); figure 4.3B.

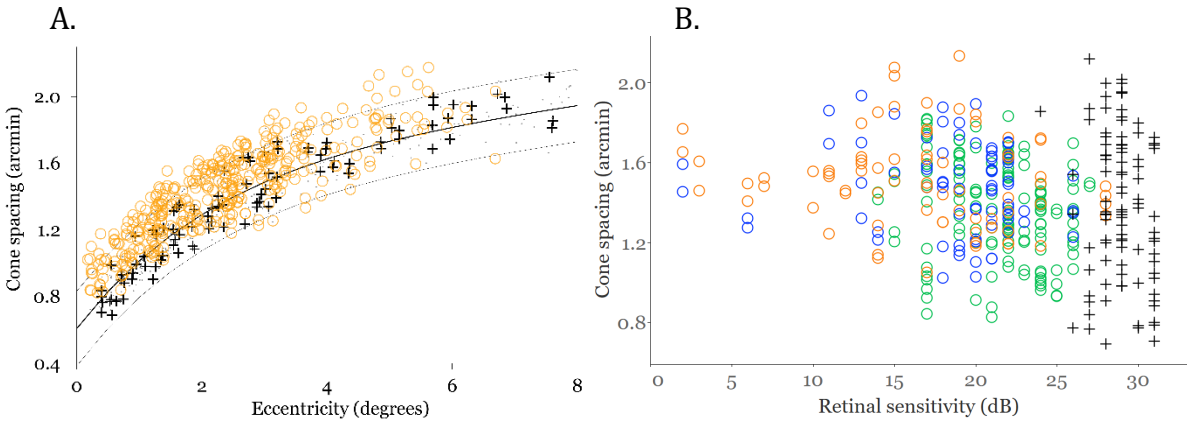

Figure 4.3. Relationship between cone spacing, eccentricity and retinal sensitivity. (A) Cone spacing measures were negatively correlated with eccentricity from the fovea. The small

black filled circles represent a normative dataset composed of 27 healthy controls (Chen et al., 2011). The dotted curved lines represent the 95% confidence interval of this normative dataset; the solid black line represents the mean. Normal subjects are shown as black crosses; patients as orange circles. (B) Cone spacing was negatively correlated with retinal sensitivity. Normal subjects are shown as black crosses, patients are circles. Measures that are more than 2 degrees (R1 on figure 4.1B) within the border of the preserved region as defined by the SS-OCT border are indicated by green circles; measures from -2° to -1° within the border are indicated by blue circles; measures from -1° to 0° within the border are indicated by orange circles.

We hypothesized that reduced CC perfusion was correlated with outer retinal atrophy. In this study, mean CC flow void was significantly increased within the region of preserved retinal structure at locations approaching and extending beyond the RPE margin, measured using both SS-OCT and SW-AF (SS-OCT: $\rho = 0.87$, 95% CI: 0.84 to 0.89; SW-AF: $\rho = 0.85$, 95% CI: 0.80 to 0.89; figure 4.4A). To control for the strong correlation between cone spacing and eccentricity, cone spacing was expressed as Z-scores, the number of standard deviations from the normal mean cone spacing at a given eccentricity. Normal cone spacing at each location was within -2 to +2 SD of the normal mean, with a Z-score between -2 and +2. Cone spacing expressed as Z-scores was not correlated with distance from the border of preserved outer retina (SS-OCT: $\rho = -0.06$, 95% CI: -0.51 to 0.17; SW-AF: $\rho = -0.04$, 95% CI: -0.38 to 0.17; figure 4.4B).

There were regions with visible cone inner and outer segments where cone spacing was measurable that extended beyond the RPE border as measured by SW-AF (figure 4.4B, blue box at +1°, and figure 4.2D-E), but no cones were evident beyond the border as measured from the SS-OCT slab. Retinal sensitivity was measurable, but reduced, 1-2 degrees beyond the margin of preserved outer retina/RPE/CC structure measured using both SW-AF and SS-OCT *en face* scans (figure 4.4C). Retinal sensitivity and distance to the RPE border were significantly, negatively correlated for patients as measured by SW-AF ($\rho = -0.89$, 95% CI: -0.91 to -0.87) and by SS-OCT ($\rho = -0.91$, 95% CI: -0.94 to -0.86; figure 4.4C). Retinal sensitivity was significantly, negatively correlated with percent CC flow void in eyes when either the SS-OCT or SW-AF borders were used to indicate RPE structure in patients (SS-OCT border: $\rho = -0.81$, 95% CI: -0.91 to -0.76; SW-AF: $\rho = -0.79$, 95% CI: -0.92 to -0.71; figure 4.4D) but not in normal subjects ($\rho = 0.37$, 95% CI: -0.86 to 1.00).

To examine the relationship between CC perfusion and cone survival, we compared CC flow voids with cone spacing expressed as Z-scores and retinal sensitivity at the region cone spacing was measured. Cone spacing was significantly, negatively correlated with percent CC flow voids for patients ($\rho = -0.29$, 95% CI: -0.60 to -0.11, figure 4.4E) but not normal subjects ($\rho = -0.19$, 95% CI: -0.50 to 3.5). Cone spacing expressed as Z-score was negatively correlated with retinal sensitivity for patients ($\rho = -0.35$, 95% CI: -0.54 to -0.18, figure 4.4F) and normal subjects ($\rho = -0.29$, 95% CI: -0.41 to -0.27).

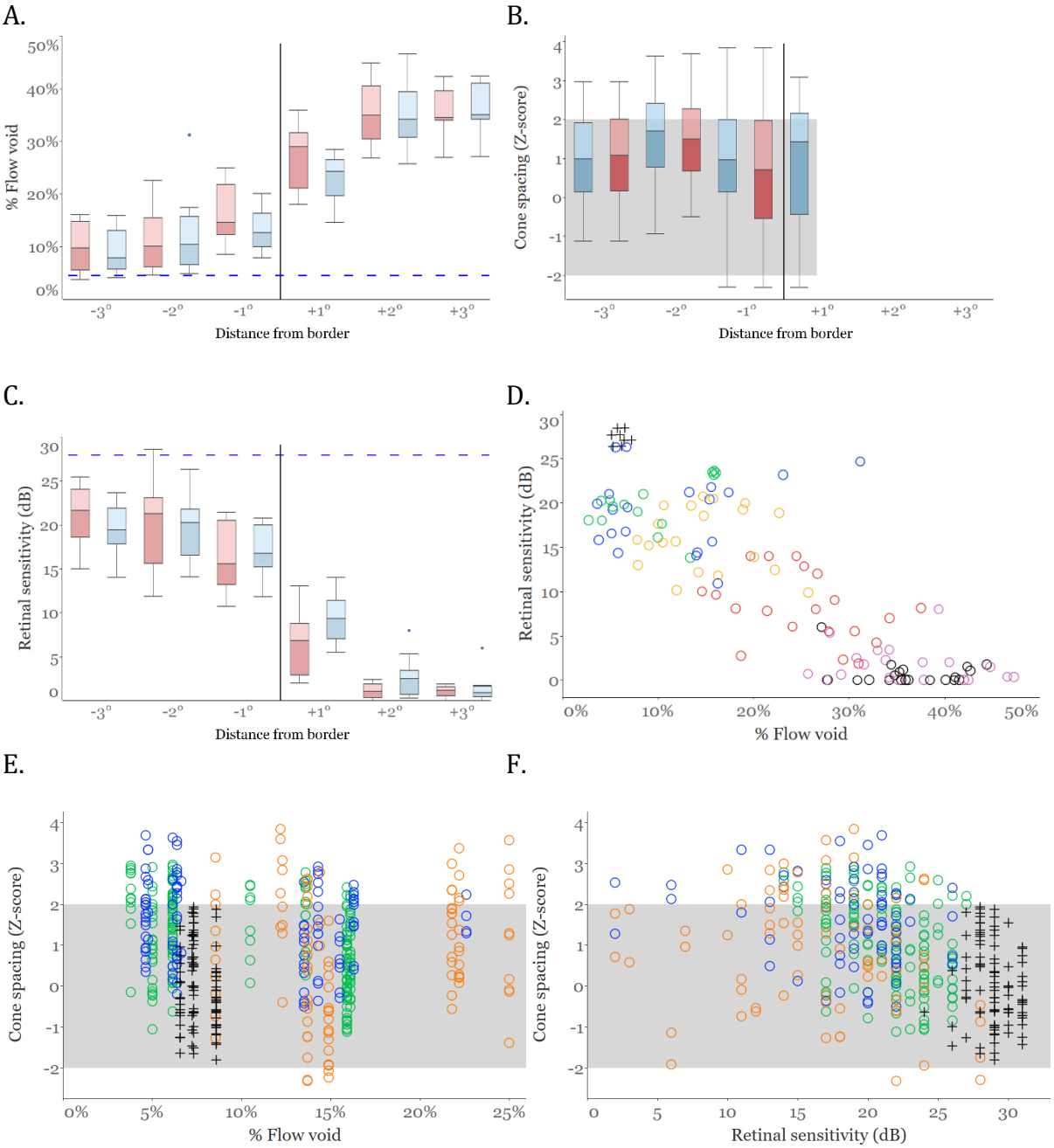

Figure 4.4. Relationship between function relative to the edge of preserved outer retina/RPE as well as function and percentage flow void. Mean choriocapillaris (CC) flow void (FV) percentages (A), cone spacing Z-score (B), and mean retinal sensitivity values (C) versus eccentricity from the edge of the preserved structure defined by the swept source optical coherence tomography (SS-OCT) outer retina-retinal pigment epithelium-choriocapillaris border (red boxes) and the short wavelength autofluorescence (SW-AF) border (blue boxes). The vertical solid black line demarcates the border measured by both SW-AF and SS-OCT slab. Horizontal dashed blue lines indicate normal mean % FV (A) and retinal sensitivity (C). Box plots indicate the middle 50% of the data, which is the middle two quartiles of the

distribution, the remaining 50% is represented by whiskers displaying all points within 1.5 times the interquartile range. The gray band shows the area within which cone spacing measures are normal (B). (D) Retinal sensitivity vs. % Flow void; (E) Cone spacing expressed as Z-score vs. % flow void; (F) Cone spacing expressed as Z-score vs. retinal sensitivity. Z-scores were used to describe cone spacing and control for the relationship between cone spacing and eccentricity (figure 3A). Normal subjects are shown as black crosses, patients as circles. Measures within 2 degrees of the border are indicated by green circles; measures from -2 to -1° inside the border are indicated by blue circles; measures from -1° to 0° inside to the border are indicated by orange circles; measures from 0° to +1° are indicated by red circles; measures from +1° to +2° are indicated by purple circles; measures from +2° to +3° are indicated by black circles.

Cone outer segment length might be affected by reduced CC perfusion, but no correlation was found between OS thickness and percent CC flow void in patients (ρ = -0.15, 95% CI: -0.42 to 0.22) or normal subjects (ρ = 0.52, 95% CI: -0.69 to 0.82) (figure 4.5A). OS thickness has been shown in prior work to correlate with retinal sensitivity in normal subjects and patients with retinitis pigmentosa (Rangaswamy et al., 2010); in the present study, OS thickness was not significantly correlated with retinal sensitivity in CHM patients (ρ = 0.22, 95% CI: -0.13 to 0.48) or normal subjects (ρ = 0.17, 95% CI: -0.02 to 0.37) (figure 4.5B). OS thickness was also not correlated with cone spacing expressed as Z-scores in CHM patients (ρ = 0.12, 95% CI: -0.45 to 0.28, figure 4.5C) but did show a significant, negative correlation for normal subjects (ρ = -0.39, 95% CI: -0.83 to -0.27).

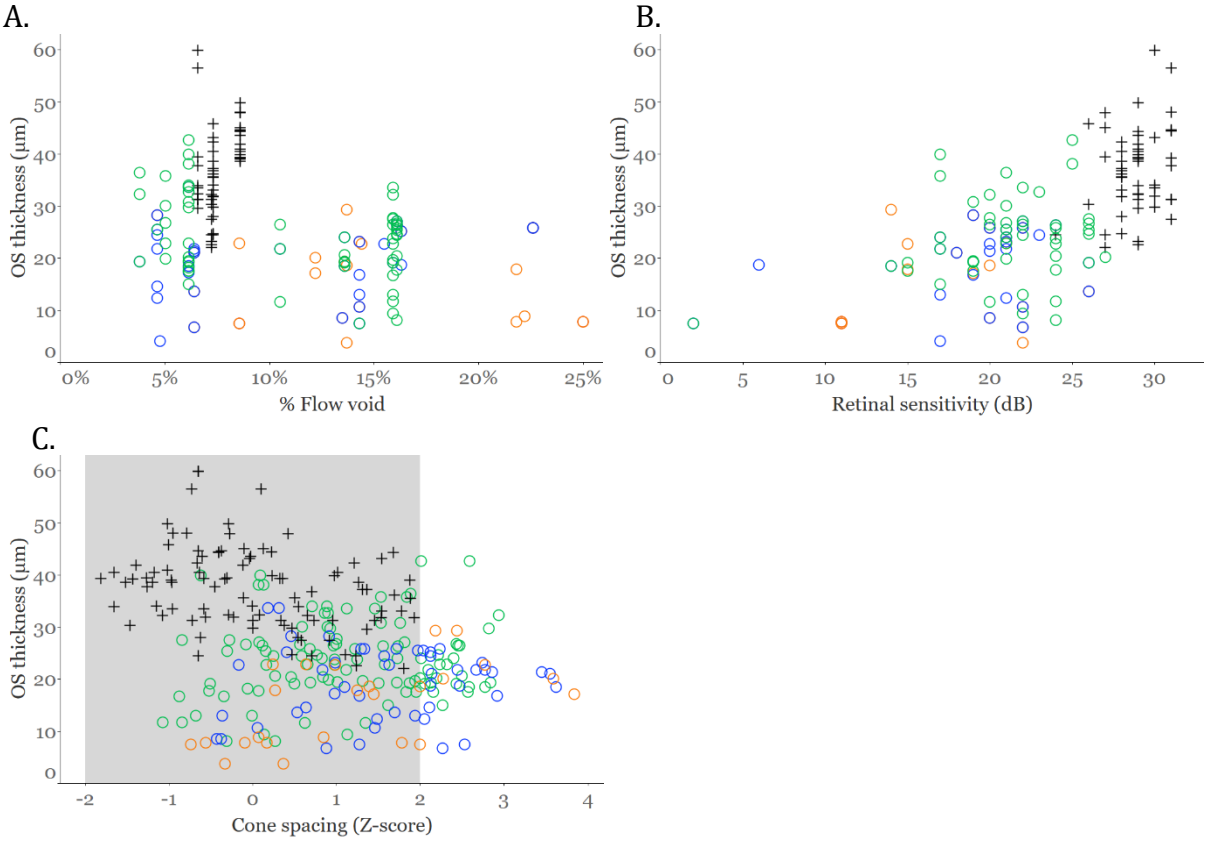

Figure 4.5. Relationship between outer segment (OS) thickness, percent flow void (FV), retinal sensitivity, and cone spacing. OS thickness and (A) % CC FV; (B) retinal sensitivity; (C) cone spacing Z-score. Normal subjects are shown as black crosses, patients as circles. All graphs show measures using the SS-OCT-derived outer retina-retinal pigment epithelial-choriocapillaris slab border. Measures within 2 degrees of the border are indicated by green circles; measures from -2° to -1° inside the border are indicated by blue circles; and measures from -1° inside to the border are indicated by orange circles. The gray band shows the Z-score range within which cone spacing measures are normal.

CC perfusion supplies the RPE and photoreceptor OS and IS with oxygen and nutrients; we studied the relationship between CC flow void and IS thickness, and found no significant correlation for patients (ρ = -0.08, 95% CI: -0.22 to 0.15) or normal subjects (ρ = 0.05, 95% CI: -0.31 to 0.19) (figure 4.6A). No correlation was seen for IS thickness vs. retinal sensitivity in patients (ρ = 0.08, 95% CI: -0.16 to 0.24) but showed a significant positive correlation for normal subjects (ρ = 0.13, 95% CI: 0.03 to 0.15) (figure 4.6B). IS thickness was not significantly correlated with cone spacing expressed as Z-scores in patients (ρ = -0.11, 95% CI: -0.36 to 0.12) but there was a significant, negative correlation among normal subjects (ρ = -0.42, 95% CI: -0.70 to -0.20) (figure 4.6C).

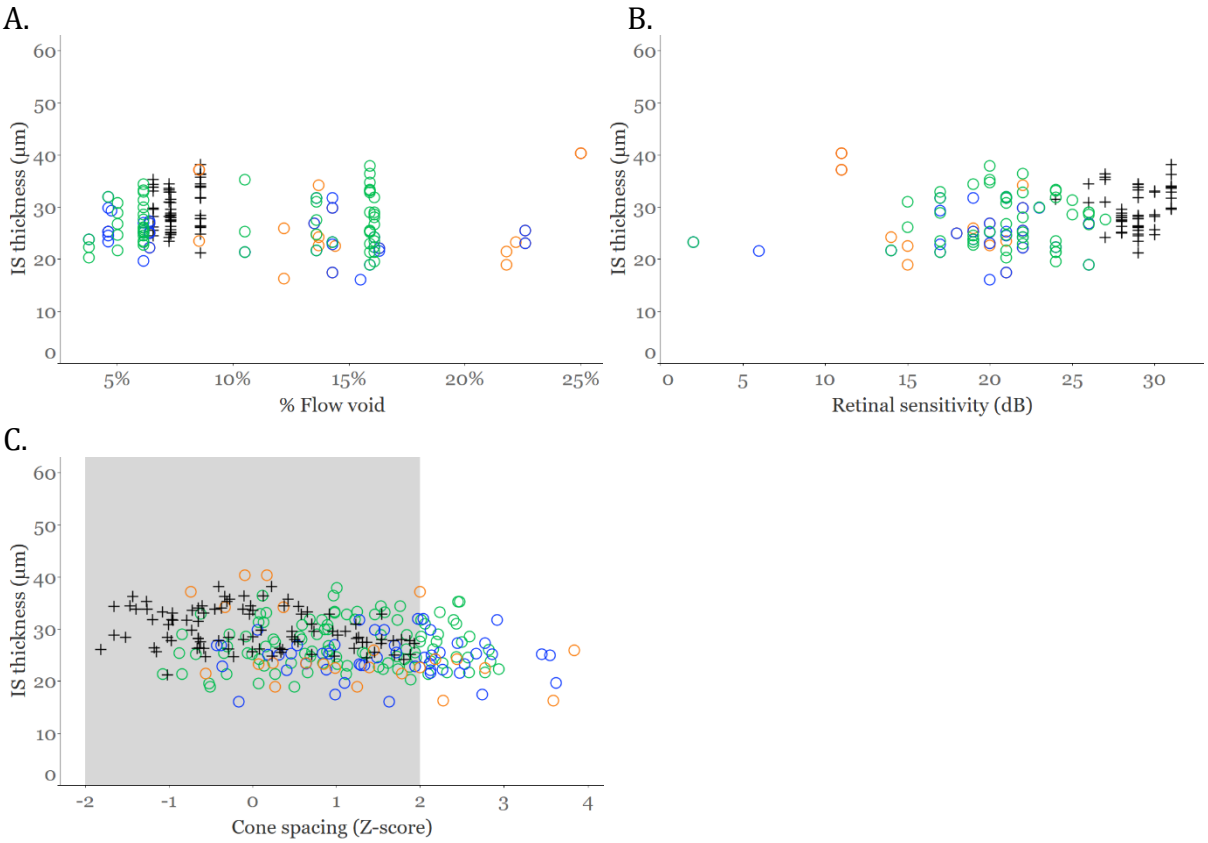

Figure 4.6. Relationship between inner segment (IS) thickness, percent flow void (FV), retinal sensitivity, and cone spacing. IS thickness and (A) % CC FV; (B) retinal sensitivity; (C) cone spacing Z-scores. Normal subjects are shown as black crosses, patients as circles. All

graphs show measures using the OCT outer retina-retinal pigment epithelial-choriocapillaris slab border. Measures within 2 degrees of the border are indicated by green circles; measures from -2° to -1° inside the border are indicated by blue circles; and measures from -1° inside to the border are indicated by orange circles. The gray band shows the area within which cone spacing measures are normal.

4.5 Discussion

Multimodal imaging demonstrated several findings that shed light on the mechanism of degeneration in patients with CHM. First, functional cones were observed beyond the border of remaining outer retinal and RPE as defined by SW-AF (figure 4.2D and E). There were regions where cone inner and outer segments were measurable beyond the RPE border as measured by SW-AF (figure 4.4B), but cone mosaics were never evident and cone spacing was not measurable beyond the margin defined by the SS-OCT slab. Cone spacing was not correlated with distance from the edge of the preserved RPE, indicating cone structure was preserved extending to the edge of atrophy (Figure 4.4B). The stimulus used to assess retinal function with fundus-guided microperimetry (Goldmann III, 26 arcmin, ~0.43 degrees) was large with respect to the size of individual photoreceptors, and it may overlap healthy photoreceptors that retain function. The use of fundus-guided microperimetry using high-speed fundus tracking and correction of stimulus delivery using AOSLO may refine the precision of stimulus delivery and provide additional insight into the function of cells that persist beyond the margin of SW-AF RPE borders (Morgan et al., 2018; Tuten et al., 2019). The persisting functional photoreceptors beyond the edge of SW-AF may affect clinical trials and treatments that are targeting preserved retinal structures based on SW-AF images. Photoreceptors may persist and be amenable to therapy in regions beyond the edge of preserved RPE defined by SW-AF and microperimetry, and could potentially show improved sensitivity in response to treatments since the inner segments and outer nuclear layer containing the nuclei persist in some areas.

The two modalities of SW-AF and SS-OCT reveal different features of degeneration in eyes with CHM which support other studies that found differences comparing separate RPE imaging methods (Paavo et al., 2018). A separate study showed that RPE preservation was greater when measured using the ellipsoid zone than using SW-AF in CHM patients (Hariri et al., 2017). Discrepancy between NIR-AF and SW-AF has also been reported in patients with Stargardt disease, in which the area of atrophy measured from NIR-AF images was greater than when imaged using SW-AF (Duncker et al., 2014). The cone structures seen extending beyond the SW-AF border suggest cones persist beyond areas with bisretinoid constituents in the outer segments and RPE cells. Cone structures beyond the edge of SW-AF included cone inner segments on split detector images, and outer segments seen on confocal AOSLO images (Figure 4.2D-E), and retinal sensitivity was measurable, although reduced, for +1° to +2° beyond the SW-AF border (figures 4.2C, 4.4C). The results may indicate that the outer segments extending beyond the SW-AF border do not contain bisretinoid constituents that normally exhibit SW-AF signal, but they may be capable of visual function. The measurable retinal sensitivity extending beyond the SW-AF margin (figures 4.2C, 4.4C) indicates there are outer segments and RPE cells in regions beyond the SW-AF margin,

although they may not exhibit normal SW-AF and demonstrate reduced sensitivity compared to regions located within the SW-AF margin.

Second, patients with CHM showed abnormal choriocapillaris perfusion, measured as flow voids, even within regions of preserved outer retinal and RPE structure (Figure 4.4A). The results suggest that the choriocapillaris is unhealthy before the RPE and outer retina degenerates. A range of alterations in CC has been reported in CHM patients (Gao et al., 2017; Jain et al., 2016; Kato et al., 2017) and CC perfusion decreases in conjunction with RPE loss measured by SW-AF (Jain et al., 2016). It is possible that cones are more dependent on the choriocapillaris than the RPE due to the putative contribution that Muller cells have on the cone visual cycle, requiring less support from the RPE (Wolf 2004). In patients with CHM, both cone spacing and retinal sensitivity correlated with CC flow void, and cone spacing significantly correlated with retinal sensitivity. The correlation between cone spacing, sensitivity and flow void suggests that sensitivity was abnormal in areas of reduced CC perfusion. The lack of a strong correlation between cone spacing and retinal sensitivity may indicate that cones are present but show reduced function. This is consistent with prior reports suggesting abnormal photoreceptor function precedes RPE loss (Aleman et al., 2017; Duncan et al., 2002), and also with the observation of visible cone inner and outer segments with reduced sensitivity extending beyond the margin of RPE as measured by SW-AF in the present study. Another explanation for the lack of correlation could be variability in subjective sensitivity measures in patients with CHM.

Third, OS thickness was not correlated with CC flow void (figure 4.5A), retinal sensitivity (figure 4.5B), or cone spacing (figure 4.5C) in CHM patients. This differs from prior reports demonstrating a correlation between OS thickness and retinal sensitivity in patients with retinitis pigmentosa (Hariri et al., 2017), perhaps because retinitis pigmentosa is often caused by mutations that are expressed primarily in photoreceptors and degeneration occurs first in the OS, then IS, then ONL (Milam et al., 1998). Unlike retinitis pigmentosa, CHM shows early thinning of RPE cells in regions with normal OS thickness (Lazow et al., 2011), and cone spacing was not correlated with distance from the margin of atrophy in the present study, suggesting OS length may be preserved despite reduced retinal sensitivity in patients with CHM. In normal subjects OS thickness, IS thickness and cone spacing were negatively correlated (figure 4.6C), and IS thickness correlated positively with retinal sensitivity (figure 4.6B), likely reflecting greater sensitivities near the fovea where inner segments are longest and cone spacing is least in normal eyes. Patients did not show a similar correlation perhaps because in some patients with inherited retinal degeneration cones have abnormal function before they degenerate and lose the inner segments, indicating that retinal sensitivity may be a more sensitive measure than cone spacing.

The present study is limited by the small number of patients and the cross-sectional nature of the report. Larger numbers of patients may reveal clearer correlations between photoreceptor, RPE and CC structure and function. To more clearly understand the mechanism of disease progression, patients will need to be monitored with high resolution retinal imaging approaches such as those described in the present study longitudinally over several years.

4.6 Summary

The use of multimodal, non-invasive imaging may provide better understanding of the sequence of degeneration in eyes with CHM. Future studies are necessary to examine longitudinal data and degeneration using multimodal techniques, including those used here. While microperimetry can provide a measure of macular sensitivity, AOSLO can visualize photoreceptor morphology. SW-AF as well as SS-OCT can provide signals from RPE structure, and SS-OCTA can display CC perfusion. Greater understanding of degeneration and disease progression is crucial to advance the development of novel therapies for this relentless, sight-threatening disease.

4.7 Acknowledgements

The labor revealed in this chapter is currently under review for publication. This chapter reflects a collaborative effort. Dr. Jacque Duncan (Department of Ophthalmology, University of California, San Francisco) dedicated instrumental contributions to the conception, design, implementation, analysis, and interpretation of this study. Dr. Austin Roorda (School of Optometry, University of California, Berkeley) provided vital support in the presentation and exposition of the work in this study. The work that went into this project would not have been possible without our collaboration with the Wang lab (Department of Bioengineering, University of Washington, Seattle, Washington) including co-authors Dr. Ruikang K. Wang, Dr. Hao Zhou, and Dr. Qinqin Zhang whose efforts in assisting with the SS-OCTA flow void data analysis provided instrumental contributions to this work. Dr. Nicolas Bensaid is credited with getting the confocal and nonconfocal, split detector AOSLO system up and running. Co-author Nicholas Rinella assisted with data collection, Janette Tang assisted with cone counting, and Dr. Travis Porco is thanked for his assistance with the data analysis. Pavan Tiruveedhula is recognized for the implementation and technical knowledge and support of the hardware and software systems of the AOSLO system. Appreciation is given to these collaborators for their contributions as well as permission to include the work in this chapter. This work was first presented at the 2018 Association for Research in Vision and Ophthalmology (Honolulu, Hawaii) conference in poster format, for which the author was grateful to receive a National Eye Institute Travel Grant.

CHAPTER 5: Structure and function in retinitis pigmentosa patients with mutations in *RHO* vs. *RPGR*

5.1 Abstract

Purpose: To study differences in cone structure and function in patients with retinitis pigmentosa (RP) due to mutations in rhodopsin (*RHO)*, expressed in rod outer segments, and patients with mutations in *RPGR,* expressed in the connecting cilium of rods and cones.

Methods: 4 eyes with *RHO* mutations, 5 with *RPGR* mutations, and 4 normal eyes were studied. Cone structure was studied with confocal and split detector adaptive optics scanning laser ophthalmoscopy (AOSLO) and spectral domain optical coherence tomography (OCT). Sensitivity was measured using AOSLO microperimetry (AOMP) and two-color fundus-guided scotopic-Macular Integrity Assessment (S-MAIA) microperimetry. Cone density was measured as close as possible to each test location. The ratio of macular sensitivity/density was compared between groups using Wilcoxon rank sum tests.

Results: Macular sensitivity per cone density in patients with *RPGR* mutations, measured as AOMP sensitivity/density ratio, was significantly lower than normal ($P<0.001$) and lower than patients with *RHO* mutations ($P<0.015$), while patients with *RHO* mutations were similar to normal ($P>0.9$). Similarly, S-MAIA sensitivity/density in *RPGR* patients was significantly lower than normal ($P<0.001$) and lower than *RHO* patients ($P=0.017$), but *RHO* patients were not different from normal ($P=0.10$).

Conclusions: Retinal sensitivity per cone density was lower in patients with *RPGR* mutations than normal and lower than patients with *RHO* mutations, perhaps because cones express *RPGR* and degenerate primarily, while cones in eyes with *RHO* mutations die secondarily. High-resolution microperimetry can provide insight into mechanisms of cone degeneration in patients with different forms of RP.

5.2 Introduction

Retinitis pigmentosa (RP) refers to a heterogeneous group of inherited diseases caused by mutations in at least 87 genes (https://www.omim.org/phenotypicSeries/PS268000) causing progressive, relentless vision loss due to retinal degeneration. Some of the first symptoms patients with RP notice are night blindness and peripheral visual field loss. As the disease progresses, patients also experience reduced visual acuity and eventual blindness because not only rod, but also cone, photoreceptor cells die. RP is the leading cause of hereditary blindness in developed countries, and its worldwide prevalence is 1:4,000, although this may be an underestimation for individual populations (Zhang 2016).

RP is most commonly inherited three ways; autosomal dominant (30%–40% cases), autosomal recessive (50%–60% cases), or X-linked (5%–15% cases), although mitochondrial inheritance also occurs (Zhang 2016). Mutations in the genes most commonly associated with RP include RP GTPase regulator (*RPGR*; 10–20% of cases), rhodopsin (*RHO*; 8–10% of cases) and usherin (*USH2A*; ~3% of cases) (Wright et al., 2010; Hartong et al., 2006; Breuer et al., 2002; Briscoe et al., 2004). Mutations in these genes typically cause rod, then cone, photoreceptor loss. For patients with *RHO* mutations, night blindness occurs around 10 years of age, onset of visual field loss is about age 20, and patients are severely visually impaired around age 50-60 (Tee et al., 2016). For patients with *RPGR* mutations, there is a similar onset of night blindness, but visual field loss onset is evident earlier, at around age 10, and significant visual impairment occurs around age 30-40 (Wright et al., 2010).

The mechanism of degeneration responsible for these 2 forms of RP is different. Rhodopsin localizes to the outer segments of rods and *RHO* mutations often cause protein misfolding and retention in the endoplasmic reticulum, leading to cellular stress and eventual cell death (Wright et al., 2010). In patients with *RHO* mutations, even though rhodopsin is expressed in rods only, the cones eventually also die, perhaps due to intercellular connections (Ripps 2002) or loss of neurotrophic factors produced by rods such as rod-derived cone viability factor (Leveillard et al., 2004). *RPGR* is localized to the connecting cilium of both rods and cones. The connecting cilium is crucial for regulating the flow of proteins from the inner to the outer segments, and *RPGR* mutations affect intracellular protein trafficking which compromises photoreceptor function and survival (Wright et al., 2010).

The current study tests the hypothesis that macular cone structure and function are significantly different in patients with mutations in *RHO* compared to patients with mutations in *RPGR* at similar stages of disease progression evaluated with OCT imaging. The goal of this study was to compare cone structure and function in patients with *RHO* mutations and patients with *RPGR* mutations using high-resolution measures of photoreceptor structure and function.

5.3 Methods

5.3.1 Study design

Research procedures followed the tenets of the Declaration of Helsinki. Informed consent was obtained from all subjects. The study protocol was approved by the institutional review boards of the University of California, San Francisco and the University of California, Berkeley.

Patients with RP due to mutations in *RHO* or *RPGR* were compared to age-similar normal subjects. Subjects were excluded if they had conditions that could affect imaging including unsteady fixation, cataract, amblyopia, and foveal cystoid macular edema. Genetic testing was performed on patients with X-linked RP and autosomal dominant RP through the eyeGENE research consortium (Sullivan et al., 2013) or using a next-generation sequencing

panel testing between 181-266 genes associated with retinal dystrophy through the genetic testing study of My Retina Tracker ®, an online registry for patients with inherited retinal degenerations (NCT02435940).

Table 5.1. Clinical characteristics of healthy normal subjects and patients with retinitis pigmentosa (RP). *RHO*, Rhodopsin; *RPGR*, RP GTPase regulator; OD, right eye; OS, left eye; M, male; F, female; BCVA, best corrected visual acuity; DS, diopter sphere.

Diagnosis	ID	Eye	Sex	Age	Mutation	Effect on Protein	Axial Length (mm)	BCVA	Refractive Error
Normal	10003	OS	M	52	None	None	23.28	20/16	0.00+0.50x180
Normal	40104	OS	M	26	None	None	24.23	20/16	plano
Normal	40154	OS	F	23	None	None	22.19	20/20	+1.50+0.05x152
Normal	40179	OD	F	31	None	None	27.72	20/20	+0.25+1.00x20
RHO	30019	OD	F	46	*RHO* c.152G>T	p.Gly51Val	25.17	20/20	-1.00+0.75x180
RHO	40095	OS	M	36	*RHO* c.810C>A	p.Ser270Arg	23.13	20/16	-1.50+0.75x095
RHO	40167	OD	F	41	*RHO* c.512C>G	p.Pro171Arg	26.46	20/25	-8.50+1.75x087
RHO	40183	OS	M	42	*RHO* c.68C>A	p.Pro23His	23.42	20/16	-0.25 DS
RPGR	40015	OD	M	25	*RPGR* ORF15 frameshift c.2426_2427del	p.Glu809GlyfsX25	24.58	20/40	-5.50+1.75x132
RPGR	40049	OS	M	26	*RPGR* c.1245+2T>C	exon 10 splice donor site mutation	24.26	20/40	1.75+1.50x140
RPGR	40064	OS	M	24	*RPGR* c.1243_1244delAG	p.Arg415Glyfs*37	22.69	20/16	-7.50+1.50x050
RPGR	40080	OS	M	35	*RPGR* c.28+5G>A	splice donor site mutation 5bp from exon-intron boundary	23.4	20/16	-3.50+0.25x130
RPGR	40159	OD	M	27	*RPGR* ORF15 c.2442_2445del	p.Gly817Lysfs*2	23.95	20/25	-5.50 DS

5.3.2 Clinical examination

Refractive error and best-corrected visual acuity (BCVA) were measured according to the Early Treatment of Diabetic Retinopathy Study (ETDRS) protocol (Ferris et al., 1982) using a standard illuminated eye chart. Axial length was measured using partial coherence interferometry (IOL Master; Carl Zeiss Meditec, Dublin, CA, USA).

5.3.3 Structural measures

5.3.3.1 Spectral Domain Optical Coherence Tomography

Spectral-domain optical coherence tomography (SD-OCT, Spectralis HRA+OCT system; Heidelberg Engineering, Vista, CA, USA) images were acquired including 15, 20 or 30 degree horizontal and vertical cross section B-scans through the fovea. Manual segmentation was performed using custom software to measure outer segment and inner segment (OS and IS) thickness lengths (Hood et al., 2011; Birch et al., 2011; Hood et al., 2009; Wen et al., 2012; Wen et al., 2011; Aizawa et al., 2009). The OS thickness was measured from the OS-RPE band

to the IS/OS junction, and the IS thickness was between the IS/OS band and the external limiting membrane. An example of a segmented OCT B-scan using this method for a patient eye with retinal degeneration can be found in previous work (Foote et al., 2019, figure 3.5 in this document).

5.3.3.2 Adaptive optics scanning laser ophthalmoscopy (AOSLO)

A non-invasive, high resolution AOSLO imaging system (Scoles et al., 2014) was used to acquire simultaneous confocal and non-confocal images. The confocal (Duncan et al., 2007; Talcott et al., 2011; Foote et al., 2019) and also non-confocal system design has been described previously (Scoles et al., 2014). The benefit of a combined confocal and non-confocal AOSLO system is that it allows for imaging and recording confocal light reflected from both the waveguiding cones from light scatter originating in the IS/OS and OS/RPE junction (Miller et al., 1996; Roorda et al., 2015) and non-confocal multiply scattered light from inner segments (Scoles et al., 2014) at the same location simultaneously. Non-confocal split detection capacity allows the scattered light from cone inner segments to be observed even in cones where the outer segments are not waveguiding (Scoles et al., 2014).

5.3.3.3 Cone density analysis

Regions of interest (ROIs) were identified using AOSLO images and selected based on areas with unambiguous cones closest to the locations tested with fundus-guided microperimetry as possible. Cone density was measured using custom software as previously described (Cooper et al., 2016). Specifically, the software computed bound cone density using Voronoi tessellation analysis for metric calculations at each ROI. Density was thereby defined as a ratio of number of bound Voronoi cells to the total area of the bound Voronoi cells (Cooper et al., 2016). This method has previously been used to characterize cones in RP patients (Sun et al., 2016). ROI locations were measured as eccentricity in degrees from the preferred retinal locus (PRL). The PRL was identified with a recorded 10 second video of the patient observing a target created by modulating the scanning raster of the AOSLO as described previously (Foote et al., 2018, section 2.3 in this document). Correlations between cone density, IS and OS thickness, and AOMP and S-MAIA sensitivity were assessed with Spearman correlation coefficients using bootstrap analyses clustered by person.

5.3.4 Functional measures

5.3.5.1 Adaptive optics microperimetry

To assess cone function, stimuli were delivered via AOSLO by modulating the scanning light source in a technique called adaptive optics microperimetry (AOMP) (figure 5.1). A combination of high speed fundus tracking with an infrared beam and stimulus delivery in real time was used to measure sensitivity at select locations with the AOSLO system. This approach allowed for imaging and delivering light stimuli to small groups of cone photoreceptors in order to test localized regions in the retina and measure sensitivity thresholds. AOMP has a delivery error of 0.89 arcmin; this is less than the cone-to-cone spacing at all eccentricities beyond 1 degree and is approximately 5.5 times better than

tracking errors of standard fundus-guided microperimeters (Tuten et al., 2012). A wavelength of 543 nm was chosen to measure cone photoreceptor sensitivity thresholds since it was equally sensed by both long- and medium-wavelength-sensitive cones (Harmening et al., 2014). The tests were made against a background light comprised of the AOSLO imaging wavelength of 840 nm, the wavefront sensing wavelength of 910 nm, and a small amount of 543 nm light which leaked through the acousto-optic modulator that was used to modulate the stimulus power. Stimuli were presented over a dynamic range of 0 – 1 arbitrary units (au) on a 1000-step linear scale (30 dB dynamic range) above a fixed background. Stimuli were presented over 6 frames for an approximate duration of 200 msec. The highest intensity for the 543 nm stimulus was 1 au = ~3.5 log Trolands (Td), and the total background luminance was ~1.65 log Td. The background intensity was greater than rod saturation which ensured that the sensitivity tests were mediated by only cones. A stimulus 0.5 times as large as a Goldmann I (3.45 arcmin, ~0.05°) stimulus was used, with 30 trials tested twice at each test location using a yes-no adaptive (QUEST) staircase algorithm thresholding procedure (Watson et al., 1983). The retina was tested at approximately 2° intervals and the temporal meridian was chosen to minimize blood vessel interaction.

5.3.5.2 Clinical microperimetry

A fundus-guided, two-color scotopic-macular integrity assessment microperimeter (S-MAIA, Centervue Inc., Fremont, CA) was used to analyze macular sensitivity of patients with RP. The S-MAIA used a 627 nm red stimulus to assess cone function, and a 505 nm cyan stimulus to assess rod function (Pfau et al., 2017). This technique has been established to be reliable at testing cone and rod function in patients with retinal degeneration (Pfau et al., 2017). The MAIA system performs real-time fundus tracking at 25 frames/second with a scanning laser ophthalmoscope (SLO) that images with an 850nm superluminescent diode scanned over a 36 x 36 degree field of view and sampled with 1024 x 1024 pixel resolution. The pupils were dilated and the patient was dark adapted for at least 30 minutes prior to microperimetry. A Goldman III (26 arcmin, 0.43°) stimulus using a standard 4-2 threshold strategy was presented for a duration of 200 ms on a 0 cd/m^2 luminance background with a dynamic range of 36 dB (Crossland, 2012, Dimopoulos, 2016). A custom grid pattern was made with stimuli every 1° from the central fixation to 10° in the four cardinal directions and also included a 1° grid over the central 6°. The central stimulus at 0° eccentricity was excluded from analysis for all conditions and all subjects and patients due to interference with the fixation target (645 nm ring with 1° diameter), which patients reported partially obscured the central stimulus and whose bleaching effects resulted in exclusion of the central stimulus in other studies as well (Pfau et al., 2017). The range of sensitivity was represented by a decibel (dB) scale; 0 dB representing the brightest stimulus, hence, a score of 0 indicates that the patient did not see it and the location had poor sensitivity. Conversely, a response of a 36 dB stimulus indicates the patient saw the dimmest stimulus and therefore that area of the retina had excellent sensitivity. A retinal sensitivity map was registered to an infrared image of the retina. The spectral sensitivity difference (cyan-red) was calculated at each point; sensitivity was rod-mediated function at locations where cyan-red was ≥ 0.

A.

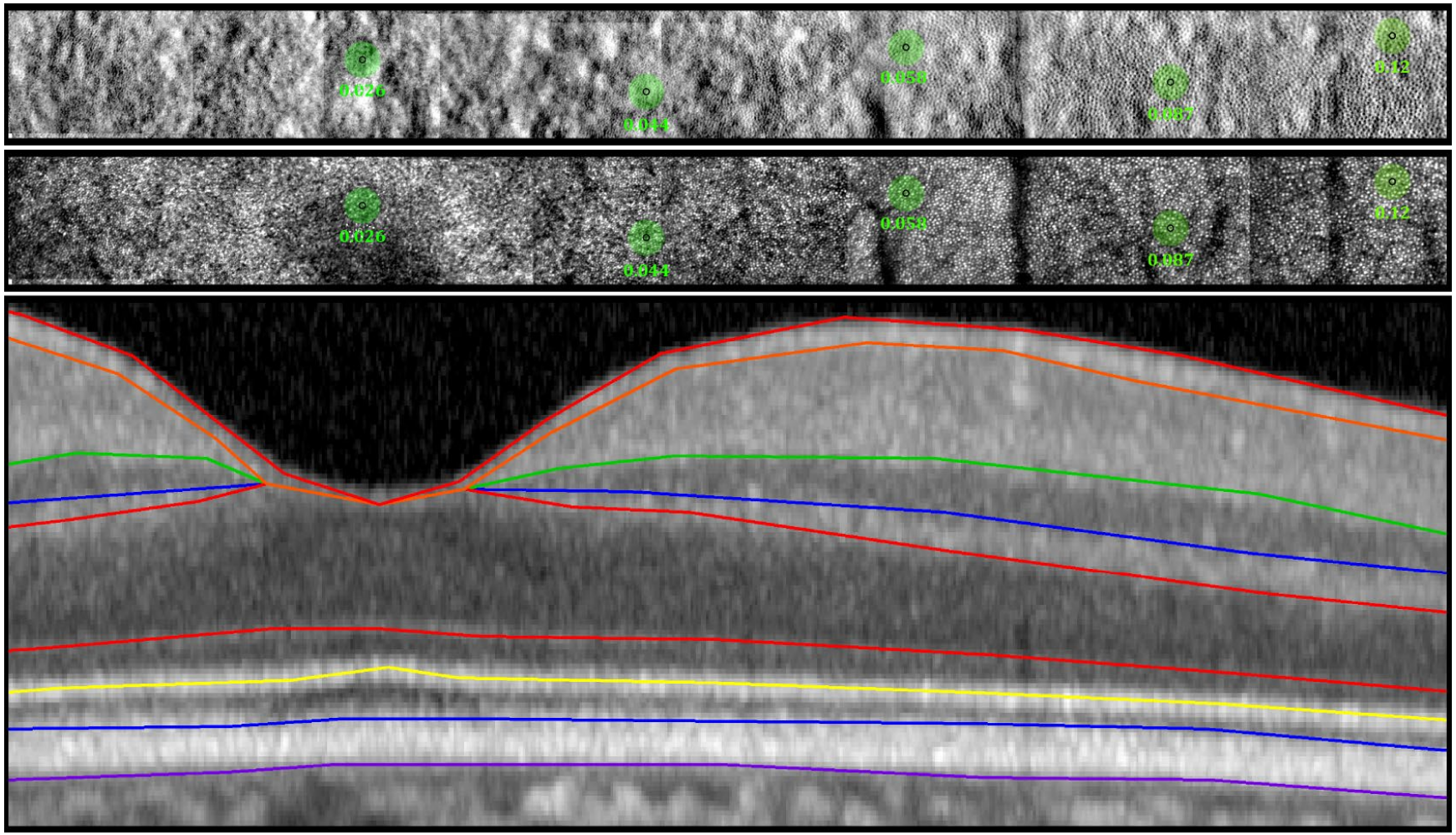

B.

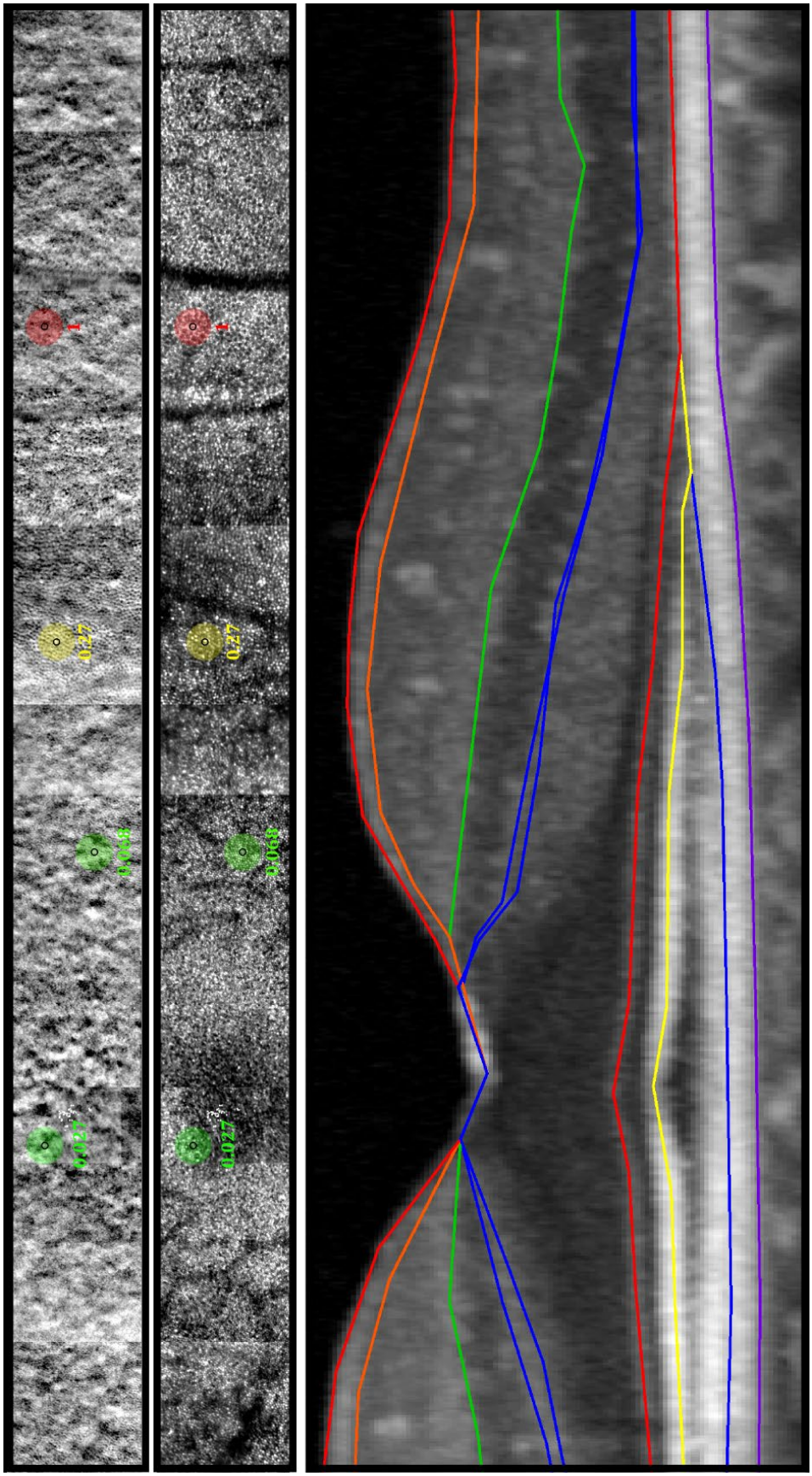

C.

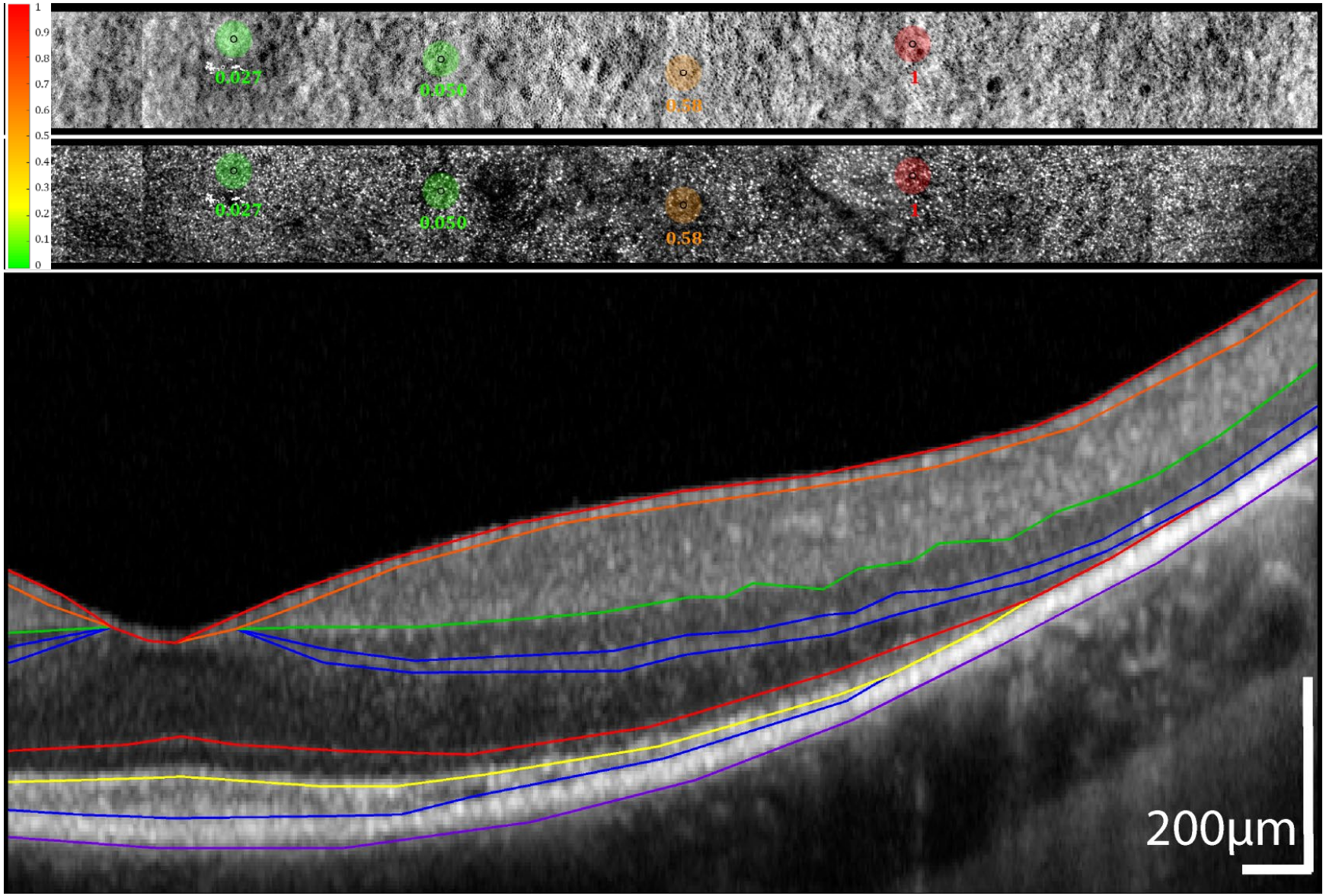

Figure 5.1. AOSLO split detector and confocal images showing AOMP test locations overlaid and OCT B-scans beneath each AOSLO/AOMP image. Images are from a normal (40154) subject (A), a patient (40095) with a *RHO* mutation (B), and a patient (40064) with a *RPGR* mutation (C). Retinal sensitivity values in color-coded circles are shaded from green (normal) to red (stimulus not seen) based on the sensitivity measured at each location; color scale bar at left of panel; scale bar: 200μm. The inner black circle represents the actual stimulus size, and the bigger colored circle is 10 times larger to increase visibility for demonstration.

5.3.5 Statistical analysis

Wilcoxon rank sum tests were used to compare the ratio of AOMP and MAIA sensitivity/cone density between normal, *RHO* and *RPGR* patients. *P* values reflect clustering by patient. Spearman correlations were calculated to determine the correlation of difference between cyan and red sensitivities and eccentricity for each group (figure 5.5A).

5.4 Results

One eye from each of four patients with mutations in *RHO* (2 female, 2 male; mean age 41.3 ± 3.8 years), five patients with mutations in *RPGR* (all male; mean age 27.3 ± 4.5 years), and four healthy subjects with normal eye examinations (2 female, 2 male; mean age 32.9 ± 13.2 years), all from unrelated families, were recruited for the study. Normal subjects and patients with *RHO* mutations were not significantly different in age (P=0.27), and normal subjects were not significantly different in age from patients with *RPGR* mutations (P=0.40), but patients with *RHO* mutations were slightly, but significantly, older than patients with *RPGR* mutations (P=0.002). Characteristics of the patients are shown in Table 5.1.

Figure 5.1 showcases AOSLO split detector and confocal images detailing AOMP test locations overlaid and OCT B-scans below each image. Three examples from each group are presented in Figure 5.1; (A) a normal subject, (B) a patient with a *RHO* mutation, and (C) a patient with a *RPGR* mutation. The normal subject presents with normal sensitivity values as indicated by the green color-coded circles, while the patients both display decreasing sensitivity, indicated by warmer color-coded circles, as their outer and inner segment bands decrease farther away from the fovea.

Figure 5.2 shows an example of split detector AOSLO images at similar locations in a patient with a *RHO* mutation (left panel) and a patient with a mutation in the *RPGR* gene (right panel). The region tested using AOMP is shown with a small black circle near the region of interest where cones were counted. At eccentricities where these 2 patients showed similar cone densities, with slightly higher density values and at a location 2.5 degrees closer to the PRL in the patient with a mutation in *RPGR*, the threshold was higher (indicating lower sensitivity) in the eye from the patient with the *RPGR* mutation. The results suggest that at a given cone density, the cones were less sensitive in patients with mutations in *RPGR* compared to patients with mutations in *RHO.*

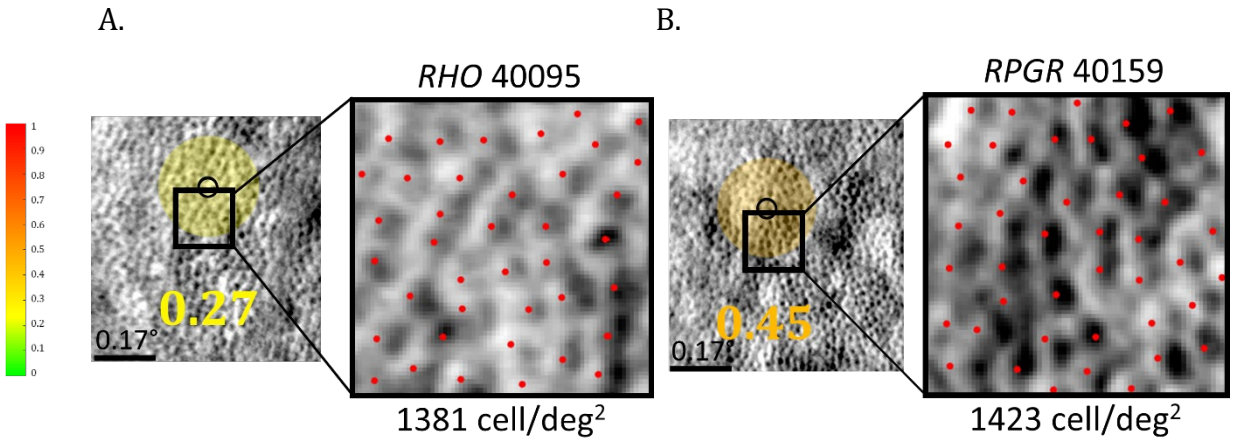

Figure 5.2. Adaptive optics scanning laser ophthalmoscopy (AOSLO) split detection image with AO microperimetry (AOMP) overlaid. AOMP sensitivity-threshold values superimposed as color-coded circle, black circle indicating actual size of stimulus, region of interest (ROI) outlined with black box, and magnified view of ROI with red marks indicating positions of cones used to assess cone density. (A) image from patient 40095 with *RHO* mutation, ROI at 3.6 degrees eccentricity; (B) image from patient 40159 with *RPGR* mutation, ROI at 1.1 degrees eccentricity. Retinal sensitivity-threshold values in color-coded circles are shaded from green (normal) to red (stimulus not seen) based on the thresholds measured at each location; color scale bar at left of panel; scale bar: 0.17 degrees.

We analyzed the sensitivity per cone by dividing the sensitivity measured with AOMP or MAIA by cone density at each ROI where sensitivity was tested and cones could be unambiguously identified and quantified. Figure 5.3A shows AOMP sensitivity divided by density at each location for normal controls, patients with *RHO* mutations and patients with *RPGR* mutations. If cone sensitivity was simply proportional to cone density, then the ratio of sensitivity to density would be constant at all locations and also between the three groups. However, if the cone dysfunction preceded structural evidence of cone loss in some patients, sensitivity would be lower at a given density.

Figure 5.3 shows lower cone sensitivity per cone in the patients with *RPGR* mutations compared to both normal subjects and compared to patients with *RHO* mutations. Sensitivity of cones in patients with *RHO* mutations was not significantly lower than normal eyes when measured using AOMP ($P>0.9$) or S-MAIA ($P>0.10$). However, sensitivity of *RPGR* cones was significantly lower than normal when measured using both AOMP ($P<0.001$) and S-MAIA ($P<0.001$), and was also lower than in cones in patients with *RHO* mutations when measured using AOMP ($P=0.0015$) and S-MAIA ($P=0.017$).

A.

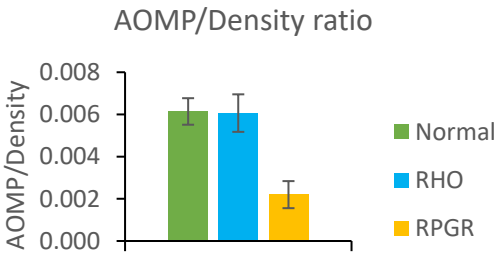

B.

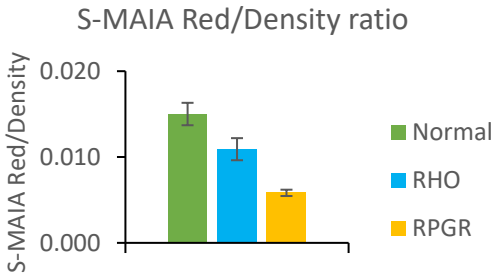

Figure 5.3. Ratio of retinal cone sensitivity to cone density. (A) AOMP/cone density ratio; (B) S-MAIA red/cone density ratio. Normal subjects are shown with green bars, patients with *RHO* mutations are shown with blue bars, patients with *RPGR* mutations are shown with orange bars. Error bars indicate the standard error of the mean. The number of measurements represented by each bar depended on the number of locations at which it was possible to compute density and perform AOMP, thus for (A), 20 measurements comprise normal, 13 comprise *RHO*, and 11 comprise *RPGR* and for (B), 32 measurements comprise normal, 20 comprise *RHO*, and 12 comprise *RPGR*.

To determine if patients with *RPGR* mutations showed lower sensitivity/density ratios because the cone outer segments were shorter than patients with *RHO* mutations, sensitivity per OS and IS thicknesses were examined. AOMP:OS thickness was not significantly different from normal in patients with *RHO* mutations (P=0.39) or *RPGR* mutations (P=0.79), and there was no difference between patients with *RHO* and *RPGR* mutations (P=0.47), but AOMP:IS thickness was significantly different from normal in patients with *RHO* mutations (P=0.04) and *RPGR* mutations (P=0.0024), and patients with *RHO* mutations were significantly different from those with *RPGR* mutations (P=0.0004). Sensitivity/IS thickness and OS thickness was slightly greater in the patients with *RHO* mutations than normal subjects (Figure 5.4), and significantly lower in the patients with *RPGR* mutations than both patients with *RHO* mutations and normal subjects for IS thickness. However, sensitivity/IS was significantly greater for patients with *RHO* mutations than normal, and significantly lower for patients with *RPGR* mutations than *RHO* mutations.

A.

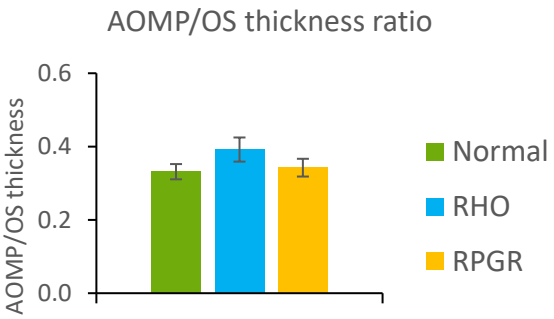

B.

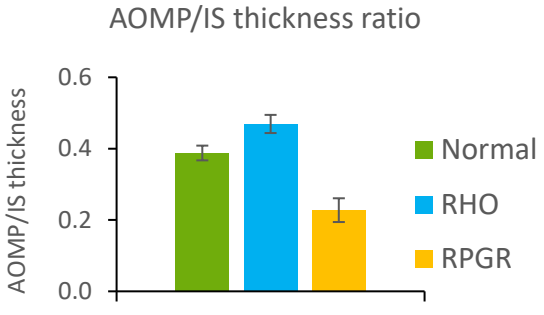

Figure 5.4. Ratio of retinal sensitivity to outer retinal thickness. (A) AOMP / OS thickness; (B) AOMP / IS thickness. Normal subjects are shown as green bars, patients with *RHO* mutations are blue, patients with *RPGR* mutations are orange.

How did cone spacing correlate with macular rod function? Scotopic MAIA was performed with both cyan and red stimuli, and the difference in sensitivity between the cyan and red stimuli was calculated to determine which cell type mediated sensitivity at different locations. Studies using other dark-adapted perimetry systems comparing responses to cyan – red stimuli have suggested rod mediation with spectral sensitivity difference values greater than approximately 5 dB (Bennett et al., 2017; Jacobson et al., 1986). While prior studies using the S-MAIA (Pfau et al., 2017) do not specify an exact dB value that demonstrates sensitivity is mediated by rod or cone function, the maximum measurable cyan – red difference with MAIA microperimetry is lower than predicted; this could be due to a small dynamic range (Pfau et al., 2017). Negative values of the cyan – red difference suggest that rods are more dysfunctional than cones, whereas positive values suggest cone dysfunction (Pfau et al., 2017).

The ratio of rod sensitivity to cone density in patients with *RHO* mutations was significantly lower than normal eyes (P=0.004); rod sensitivity/cone density of *RPGR* cones was also significantly lower than normal (P<0.001), but was not statistically significantly lower than in patients with *RHO* mutations (P=0.15) (Figure 5.5A). Figure 5.5B shows the correlation between the difference in sensitivity between the cyan and red stimuli and retinal eccentricity. Normal subjects and patients with *RHO* mutations showed similar correlations (r =0.71 and 0.70, respectively) with eccentricity, while the correlation between rod function and eccentricity was significantly lower in patients with *RPGR* mutations (r = 0.43). Patients with *RHO* mutations showed considerably more negative values throughout, indicating cone function mediated sensitivity at most locations tested. Patients with *RPGR* mutations however, showed higher values at most locations, indicating both rod and cone dysfunction (Pfau et al., 2017) (Figure 5.5B).

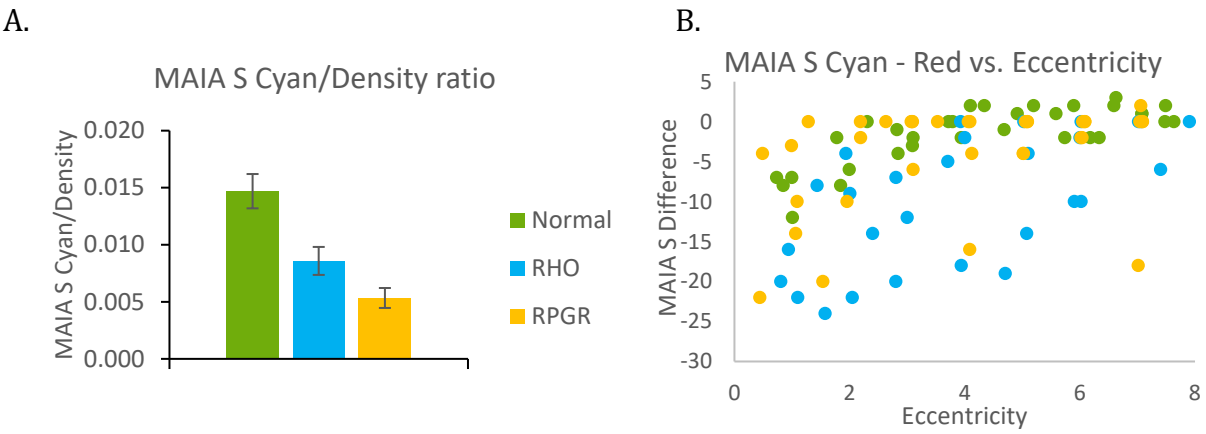

Figure 5.5. Ratio of retinal sensitivity to a cyan stimulus over cone density, and comparison of cyan vs. red sensitivity. (A) S-MAIA cyan/cone density ratio; (B) S-MAIA difference

between cyan and red vs. eccentricity. Normal subjects are shown as green bars or circles, patients with *RHO* mutations are blue, patients with *RPGR* mutations are orange.

We analyzed the relationship between IS and OS thickness and cone density to determine if there were some difference in progressive loss of photoreceptor structure in each of the 3 groups. OS thickness per cone density in patients with *RHO* mutations was not significantly shorter than normal eyes (P=0.48) (Figure 5.6). However, OS thickness per cone density in patients with *RPGR* mutations was significantly lower than normal (P<0.001) and was also lower than patients with *RHO* mutations (P=0.032). IS thickness per cone density was significantly lower than normal in both patients with *RHO* mutations (P=0.013) and *RPGR* mutations (P=0.002), but there was no statistically significant difference between the two patient groups (P=0.42).

A.

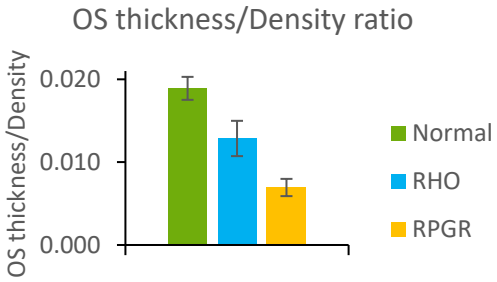

B.

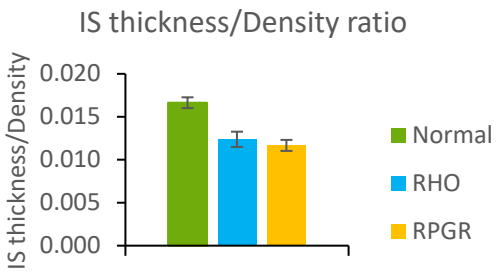

Figure 5.6. Ratio of retinal thicknesses to cone density. (A) Outer segment (OS) thickness/density ratio; (B) Inner segment (IS) thickness/density ratio. Normal subjects are shown as green bars, patients with *RHO* mutations are blue, patients with *RPGR* mutations are orange. Error bars indicate the standard error of the mean. The number of measurements represented by each bar depended on the number of locations at which it was possible to compute cone density, thus for both graphs, 36 measurements comprise normal, 23 comprise *RHO*, and 14 comprise *RPGR*.

5.5 Discussion

High-resolution retinal imaging demonstrated significant differences in the structure and function of cones and function of rods in patients with *RHO* mutations as well as patients with *RPGR* mutations. Patients with *RHO* mutations showed more sensitive cones and rods than patients with *RPGR* mutations. These trends observed are likely a result of the differing mechanisms of disease between the two groups.

Patients in the two groups that were included in the study were in stages of disease progression which retained well-preserved macular outer retinal structure. For patients with *RHO* mutations, patients included had the Class B phenotype, which progress more slowly than patients with the Class A phenotype (Sung et al., 1993; Cideciyan et al., 2005). Patients with *RPGR* mutations, who typically express more severe clinical manifestations than the Class B phenotype patients with *RHO* mutations, were enrolled at earlier stages of

disease progression to include patients with preserved macular photoreceptors (Wang et al., 2005). Thus, in this study, patients with *RHO* mutations were significantly older than the patients with *RPGR* mutations, which is a result of the increased rate of disease progression in *RPGR*.

Patients with mutations in *RHO* showed better cone function compared to patients with mutations in *RPGR* and showed greater cone sensitivity in regions with similar cone density (Figure 5.3). This suggests that while the cones might appear to show similarly preserved structure, function was reduced to a greater extent in eyes with *RPGR* mutations than patients with *RHO* mutations. Furthermore, in patients with mutations in *RPGR*, outer segments were shorter at a given cone density (Figure 5.6), which likely contributed to reduced sensitivities in patients with *RPGR* mutations. Patients with mutations in *RHO* had better cone sensitivity, likely due to the mechanism of degeneration in *RHO*-mediated RP, in which rods are affected primarily.

Given that MAIA is a readily available system for clinical use, it is encouraging that when compared with the custom built, high-resolution cone-targeted AOMP method, results showed similar evidence of reduced sensitivity per cone density in eyes with *RPGR*-related RP. Although AOMP showed slightly more statistically significant results in the present study, MAIA showed the same trends in the sensitivity to density ratio comparisons (Figure 5.3). Similarly, in prior studies of patients with retinal degenerations, AOSLO-mediated acuity measures were not significantly better than ETDRS acuity in patients with retinal degenerations, perhaps because acuity was limited by reduced cone densities near the fovea (Pfau et al., 2017). Until AOMP becomes widely available, the MAIA could be considered comparable for studies concerned with analyzing function in inherited retinal degeneration. However, if precise stimulus localization is required for disease assessment, AOMP can be useful to provide exact placement of stimuli on particular retinal areas on interest.

To compare rod with cone function and survival in patients with *RHO* mutations and patients with *RPGR* mutations, we also assessed ratios of rod sensitivity per cone density (figure 5.5A) and saw that normal subjects had significantly higher rod sensitivity/cone density than either patients with *RHO* or *RPGR* mutations. Patients with *RHO* mutations had less rod sensitivity than normal subjects and greater loss of rod sensitivity with preserved cone function, corresponding to greater macular sensitivity/cone density than patients with *RPGR* mutations.

To further elucidate any putative relationships between the two patient groups, we compared performance of cone and rod function for each patient and found that the majority of patients with *RHO* mutations had macular sensitivity mediated by cone function at locations where rod function was diminished. However, the majority of patients with *RPGR* mutations exhibited reduced cone and rod function with some regions demonstrating rod-mediated function and other locations showing cone-mediated function in the macula (figure 5.5B).

Because cones are more densely packed in the fovea, with rod density greatest at 12 degrees eccentricity (Curcio et al., 1990), we would expect macular function to be mediated by cones

closer to the fovea, and to show mixed mediation or mediation by rods at locations further away from the fovea. In this study, normal subjects showed negative spectral sensitivity difference values closer to the fovea, where cones mediated sensitivity, and positive values at greater distances from the fovea, where sensitivity was mixed (cones perceive red stimuli and rods perceive blue stimuli) (Figure 5.5B). Patients with *RHO* mutations showed considerably more negative values throughout the macula, and showed a correlation with eccentricity similar to normal subjects, indicating that cones mediated macular function at the locations tested in both *RHO*-mediated RP and normal subjects. Patients with *RPGR* mutations, however, showed a much lower correlation between function and eccentricity with higher differences, indicating both rods and cones were abnormal and were contributing to perception in the macula, which could reflect the inherent difference in degeneration due to expression of *RPGR* in both rods and cones.

Photoreceptor degeneration in RP patients affects outer segments followed by inner segments (Gao et al., 2002), which could explain why the IS thickness/density plot (Figure 5.6A) shows less drastic differences between patients with *RHO* mutations and patients with *RPGR* mutations than the OS thickness/density plot (Figure 5.6B). Figure 5.6B also suggests that sensitivity is proportional to OS thickness. Patients with *RPGR* mutations have shorter outer segments for a given density (Figure 5.4A) and correspondingly lower sensitivity (Figure 5.3A)

5.6 Conclusion

In conclusion, cones in patients with *RHO* mutations remain more sensitive than cones in patients with *RPGR* mutations (Figures 5.2-5.4). This is likely because cones express *RPGR*, not *RHO*, and degenerate intrinsically in patients with *RPGR* mutations, and because outer segments are generally shorter in patients with *RPGR* mutations (Figure 5.6), since sensitivity per OS thickness was not significantly different among the 3 groups. The observation that *RPGR*-related RP patients showed lower sensitivity per IS length as well as per cone density may reflect the fact that cone spacing is measured from AOSLO images where cone inner segments are visible to quantify. Patients with *RHO* mutations had higher measurable cone sensitivity compared to patients with *RPGR* mutations, probably because both rods and cones express *RPGR* and are affected in patients with *RPGR* mutations, causing earlier degeneration of both rod and cone function. Prior studies have shown enhanced rod bipolar function in rat eyes with transgenic P23H *RHO* mutations that compensate for some of the rod loss (Aleman et al., 2008; Chrysostomou et al., 2009). We observed slightly greater sensitivity/IS thickness and OS thickness in the *RHO* patients than normal (Figure 5.4) which could in part be explained by this phenomenon whereby patients with RP due to *RHO* mutations demonstrate improved sensitivity which is mediated by increased bipolar cell function that produces improved sensitivity per cone density.

The present study has many limitations, including the small number of subjects assessed with each genetic form of RP studied. In addition, the study is cross-sectional and inter-individual variation in cone density near the fovea could contribute to differences in cone density observed between the groups. Longitudinal studies with greater numbers of patients

who have RP associated with mutations in *RHO* and *RPGR* would provide a more comprehensive assessment of the relationships reported. In addition, future studies should compare structure and function of rods in addition to cones in eyes with RP since this is primarily a rod degenerative disease. To test rod function with AOMP, the AOSLO system would need to be adapted for rod functional measurement. With a modified scotopic AOSLO, one could elucidate pressing research questions such as how rods are affected in the macula of RP patients who retain central cones; or the threshold of rod loss before which cone spacing becomes abnormal; and, whether rod loss is different in eyes with RP caused by mutations expressed only in rods compared to mutations expressed in rods and cones. A deeper understanding of rod loss in patients with RP is essential to advance developments of therapies for such a relentless, progressive disease affecting all photoreceptors.

AOSLO and AOMP as part of a multimodal approach are vital to understanding relationships between structure and function and genotype/phenotype variations. This study provides a foundation for investigating RP disease progression as well as a measurement for potential treatment reactions using AOSLO imaging techniques. The high resolution measures used here to visualize structure and measure function have the capacity to deliver specific, precise, objective, and sensitive measures of health and survival of cone photoreceptors. Thus, this approach may facilitate improved understanding of disease mechanism in different forms of retinal degeneration. Furthermore, the present study highlights fundamental differences in retinal structure and function in patients with RP due to different genetic mutations. The results support the need for natural history trials of genetically-characterized patients with RP to identify the most sensitive outcome measures of disease progression in patients with different genetic forms of RP. High resolution measures of retinal structure and function may also accelerate development of novel treatments for retinal degenerative diseases, which currently have no cure and extremely limited treatments due largely to previous low resolution and insensitive clinical instrumentation.

5.7 Acknowledgements

This chapter is on its way to be submitted for publication. Dr. Jacque Duncan (Department of Ophthalmology, University of California, San Francisco) provided support to the conception, design, implementation, and analysis of this study. Dr. Austin Roorda (School of Optometry, University of California, Berkeley) also provided contributions in design, analysis, and interpretation of this study. Co-authors Jessica Wong and Ethan Bensinger contributed to the data collection, and co-author Alexandra Boehm contributed to the experimental setup. Dr. Travis Porco is thanked for his help with analyses. The work in this study would not be possible without technical AOSLO system support from Pavan Tiruveedhula. Much appreciation is given to these collaborators for their contributions as well as permission to include the work in this chapter. This work was first presented at the 2019 Association for Research in Vision and Ophthalmology (Vancouver, British Columbia) conference, during which the author was grateful for the opportunity to present it as a talk.

References

Acton JH, Greenberg JP, Greenstein VC, Marsiglia M, Tabacaru M, Smith RT, Tsang SH. Evaluation of multimodal imaging in carriers of X-linked retinitis pigmentosa. Experimental eye research. 2013 Aug 1;113:41-8.

Aizawa S, Mitamura Y, Baba T, Hagiwara A, Ogata K, Yamamoto S. Correlation between visual function and photoreceptor inner/outer segment junction in patients with retinitis pigmentosa. Eye. 2009 Feb;23(2):304.

Akeo K, Hiida Y, Saga M, Inoue R, Oguchi Y. Correlation between contrast sensitivity and visual acuity in retinitis pigmentosa patients. Ophthalmologica. 2002;216(3):185-91.

Akman A. Optical coherence tomography: basics and technical aspects. In: Akman A, Bayer A, Nouri-Mahdavi K (eds), Optical coherence tomography in glaucoma: a practical guide. Cham, Switzerland: Springer International Publishing AG; 2018:7-12.

Aleman TS, Cideciyan AV, Sumaroka A, Windsor EA, Herrera W, White DA, Kaushal S, Naidu A, Roman AJ, Schwartz SB, Stone EM. Retinal laminar architecture in human retinitis pigmentosa caused by Rhodopsin gene mutations. Investigative ophthalmology & visual science. 2008 Apr 1;49(4):1580-90.

Aleman TS, Han G, Serrano LW, Fuerst NM, Charlson ES, Pearson DJ, Chung DC, Traband A, Pan W, Ying GS, Bennett J. Natural history of the central structural abnormalities in choroideremia: a prospective cross-sectional study. Ophthalmology. 2017 Mar 1;124(3):359-73.

Aleman TS, LaVail MM, Montemayor R, Ying GS, Maguire MM, Laties AM, Jacobson SG, Cideciyan AV. Augmented rod bipolar cell function in partial receptor loss: an ERG study in P23H rhodopsin transgenic and aging normal rats. Vision research. 2001 Sep 1;41(21):2779-97.

Alexander KR, Hutman LP, Fishman GA. Dark-adapted foveal thresholds and visual acuity in retinitis pigmentosa. Archives of Ophthalmology. 1986 Mar 1;104(3):390-4.

Arathorn DW, Yang Q, Vogel CR, Zhang Y, Tiruveedhula P, Roorda A. Retinally stabilized cone-targeted stimulus delivery. Optics express. 2007 Oct 17;15(21):13731-44.

Arditi A, Cagenello R. On the statistical reliability of letter-chart visual acuity measurements. Investigative ophthalmology & visual science. 1993 Jan 1;34(1):120-9.

Bailey IL, Lovie JE. New design principles for visual acuity letter charts. American journal of optometry and physiological optics. 1976 Nov;53(11):740-5.

Bailey JE, Lakshminarayanan V, Enoch JM. The Stiles-Crawford function in an aphakic subject with retinitis pigmentosa. Clinical vision sciences. 1991;6(2):165-70.

Parodi MB, Arrigo A, MacLaren RE, Aragona E, Toto L, Mastropasqua R, Manitto MP, Bandello F. Vascular alterations revealed with optical coherence tomography angiography in patients with choroideremia. Retina. 2019 Jun 1;39(6):1200-5.

Battu R, Khanna A, Hegde B, Berendschot TT, Grover S, Schouten JS. Correlation of structure and function of the macula in patients with retinitis pigmentosa. Eye. 2015 Jul;29(7):895.

Beckers JM. Adaptive optics for astronomy: principles, performance, and applications. Annual review of astronomy and astrophysics. 1993 Sep;31(1):13-62.

Bennett J, Wellman J, Marshall KA, McCague S, Ashtari M, DiStefano-Pappas J, Elci OU, Chung DC, Sun J, Wright JF, Cross DR. Safety and durability of effect of contralateral-eye administration of AAV2 gene therapy in patients with childhood-onset blindness caused by RPE65 mutations: a follow-on phase 1 trial. The Lancet. 2016 Aug 13;388(10045):661-72.

Bennett LD, Klein M, Locke KG, Kiser K, Birch DG. Dark-adapted chromatic perimetry for measuring rod visual fields in patients with retinitis pigmentosa. Translational vision science & technology. 2017 Jul 1;6(4):15.

Berson EL, Rosner B, Sandberg MA, Hayes KC, Nicholson BW, Weigel-DiFranco C, Willett W. A randomized trial of vitamin A and vitamin E supplementation for retinitis pigmentosa. Archives of ophthalmology. 1993 Jun 1;111(6):761-72.

Berson EL, Rosner B, Sandberg MA, Weigel-DiFranco C, Moser A, Brockhurst RJ, Hayes KC, Johnson CA, Anderson EJ, Gaudio AR, Willett WC. Clinical trial of docosahexaenoic acid in patients with retinitis pigmentosa receiving vitamin a treatment. Archives of ophthalmology. 2004 Sep 1;122(9):1297-305.

Birch DG, Locke KG, Felius J, Klein M, Wheaton DK, Hoffman DR, Hood DC. Rates of decline in regions of the visual field defined by frequency-domain optical coherence tomography in patients with RPGR-mediated X-linked retinitis pigmentosa. Ophthalmology. 2015 Apr 1;122(4):833-9.

Birch DG, Locke KG, Wen Y, Locke KI, Hoffman DR, Hood DC. Spectral-domain optical coherence tomography measures of outer segment layer progression in patients with X-linked retinitis pigmentosa. JAMA ophthalmology. 2013 Sep 1;131(9):1143-50.

Birch DG, Sandberg MA, Berson EL. The Stiles-Crawford effect in retinitis pigmentosa. Investigative ophthalmology & visual science. 1982 Feb 1;22(2):157-64.

Birch DG, Wen Y, Locke K, Hood DC. Rod sensitivity, cone sensitivity, and photoreceptor layer thickness in retinal degenerative diseases. Investigative ophthalmology & visual science. 2011 Sep 1;52(10):7141-7.

Birtel J, Salvetti AP, Jolly JK, Xue K, Gliem M, Müller PL, Holz FG, MacLaren RE, Issa PC. Near-Infrared Autofluorescence in Choroideremia: Anatomic and Functional Correlations. American journal of ophthalmology. 2019 Mar 1;199:19-27.

Biswas P, Duncan JL, Maranhao B, Kozak I, Branham K, Gabriel L, Lin JH, Barteselli G, Navani M, Suk J, Parke M. Genetic analysis of 10 pedigrees with inherited retinal degeneration by exome sequencing and phenotype-genotype association. Physiological genomics. 2017 Jan 27;49(4):216-29.

Blain D, Goetz KE, Ayyagari R, Tumminia SJ. eyeGENE®: a vision community resource facilitating patient care and paving the path for research through molecular diagnostic testing. Clinical genetics. 2013 Aug;84(2):190-7.

Bowmaker JK, Dartnall H. Visual pigments of rods and cones in a human retina. The Journal of physiology. 1980 Jan 1;298(1):501-11.

Bravo-Gil N, González-del Pozo M, Martín-Sánchez M, Méndez-Vidal C, Rodríguez-de La Rúa E, Borrego S, Antiñolo G. Unravelling the genetic basis of simplex Retinitis Pigmentosa cases. Scientific reports. 2017 Feb 3;7:41937.

Breuer DK, Yashar BM, Filippova E, Hiriyanna S, Lyons RH, Mears AJ, Asaye B, Acar C, Vervoort R, Wright AF, Musarella MA. A comprehensive mutation analysis of RP2 and RPGR in a North American cohort of families with X-linked retinitis pigmentosa. The American Journal of Human Genetics. 2002 Jun 1;70(6):1545-54.

Briscoe AD, Gaur C, Kumar S. The spectrum of human rhodopsin disease mutations through the lens of interspecific variation. Gene 2004;332:107-118.

Brooks BP, MacDonald IM, Tumminia SJ, Smaoui N, Blain D, Nezhuvingal AA, Sieving PA. Genomics in the era of molecular ophthalmology: reflections on the National Ophthalmic Disease Genotyping Network (eyeGENE). Archives of ophthalmology. 2008 Mar 1;126(3):424-5.

Bruce KS, Harmening WM, Langston BR, Tuten WS, Roorda A, Sincich LC. Normal perceptual sensitivity arising from weakly reflective cone photoreceptors. Investigative ophthalmology & visual science. 2015 Jul 1;56(8):4431-8.

Cai X, Conley SM, Naash MI. RPE65: role in the visual cycle, human retinal disease, and gene therapy. Ophthalmic genetics. 2009 Jan 1;30(2):57-62.

Carrigan M, Duignan E, Malone CP, Stephenson K, Saad T, McDermott C, Green A, Keegan D, Humphries P, Kenna PF, Farrar GJ. Panel-based population next-generation sequencing for inherited retinal degenerations. Scientific reports. 2016 Sep 14;6:33248.

Chen FK, Patel PJ, Xing W, Bunce C, Egan C, Tufail AT, Coffey PJ, Rubin GS, Da Cruz L. Test–retest variability of microperimetry using the Nidek MP1 in patients with macular disease. Investigative ophthalmology & visual science. 2009 Jul 1;50(7):3464-72.

Chen M, Cooper RF, Han GK, Gee J, Brainard DH, Morgan JI. Multi-modal automatic montaging of adaptive optics retinal images. Biomedical optics express. 2016 Dec 1;7(12):4899.

Chen Y, Ratnam K, Sundquist SM, Lujan B, Ayyagari R, Gudiseva VH, Roorda A, Duncan JL. Cone photoreceptor abnormalities correlate with vision loss in patients with Stargardt disease. Investigative ophthalmology & visual science. 2011 May 1;52(6):3281-92.

Choi SS, Doble N, Hardy JL, Jones SM, Keltner JL, Olivier SS, Werner JS. In vivo imaging of the photoreceptor mosaic in retinal dystrophies and correlations with visual function. Investigative ophthalmology & visual science. 2006 May 1;47(5):2080-92.

Chrysostomou V, Stone J, Valter K. Life history of cones in the rhodopsin-mutant P23H-3 rat: evidence of long-term survival. Investigative ophthalmology & visual science. 2009 May 1;50(5):2407-16.

Chui TY, Song H, Burns SA. Adaptive-optics imaging of human cone photoreceptor distribution. Journal of the Optical Society of America. A, Optics, image science, and vision. 2008 Dec;25(12):3021.

Chui TY, Song H, Clark CA, Papay JA, Burns SA, Elsner AE. Cone photoreceptor packing density and the outer nuclear layer thickness in healthy subjects. Investigative ophthalmology & visual science. 2012 Jun 1;53(7):3545-53.

Cideciyan AV, Aleman TS, Boye SL, Schwartz SB, Kaushal S, Roman AJ, Pang JJ, Sumaroka A, Windsor EA, Wilson JM, Flotte TR. Human gene therapy for RPE65 isomerase deficiency activates the retinoid cycle of vision but with slow rod kinetics. Proceedings of the National Academy of Sciences. 2008 Sep 30;105(39):15112-7.

Cideciyan AV, Swider M, Aleman TS, Roman MI, Sumaroka A, Schwartz SB, Stone EM, Jacobson SG. Reduced-illuminance autofluorescence imaging in ABCA4-associated retinal degenerations. JOSA A. 2007 May 1;24(5):1457-67.

Cideciyan AV, Swider M, Jacobson SG. Autofluorescence imaging with near-infrared excitation: normalization by reflectance to reduce signal from choroidal fluorophores. Investigative ophthalmology & visual science. 2015 May 1;56(5):3393-406.

Consugar MB, Navarro-Gomez D, Place EM, Bujakowska KM, Sousa ME, Fonseca-Kelly ZD, Taub DG, Janessian M, Wang DY, Au ED, Sims KB. Panel-based genetic diagnostic testing for inherited eye diseases is highly accurate and reproducible, and more sensitive for variant detection, than exome sequencing. Genetics in Medicine. 2015 Apr;17(4):253.

Cooper RF, Wilk MA, Tarima S, Carroll J. Evaluating descriptive metrics of the human cone mosaic. Investigative ophthalmology & visual science. 2016 Jun 1;57(7):2992-3001.

Coussa RG, Traboulsi EI. Choroideremia: a review of general findings and pathogenesis. Ophthalmic genetics. 2012 Jun 1;33(2):57-65.

Cremers F, Boon C, Bujakowska K, Zeitz C. Special issue introduction: inherited retinal disease: novel candidate genes, genotype–phenotype correlations, and inheritance models. 2018: 215.

Cremers FP, van de Pol DJ, van Kerkhoff LP, Wieringa B, Ropers HH. Cloning of a gene that is rearranged in patients with choroideremia. Nature. 1990 Oct;347(6294):674.

Crossland MD, Jackson ML, Seiple WH. Microperimetry: a review of fundus related perimetry. Optometry Reports 2012;2:2.

Curcio CA, Sloan KR, Kalina RE, Hendrickson AE. Human photoreceptor topography. Journal of comparative neurology. 1990 Feb 22;292(4):497-523.

Dimopoulos IS, Tseng C, MacDonald IM. Microperimetry as an outcome measure in choroideremia trials: reproducibility and beyond. Investigative ophthalmology & visual science. 2016 Aug 1;57(10):4151-61.

Duncan JL, Aleman TS, Gardner LM, De Castro E, Marks DA, Emmons JM, Bieber ML, Steinberg JD, Bennett J, Stone EM, MacDonald IM. Macular pigment and lutein supplementation in choroideremia. Experimental eye research. 2002 Mar 1;74(3):371-81.

Duncan JL, Talcott KE, Ratnam K, Sundquist SM, Lucero AS, Day S, Zhang Y, Roorda A. Cone structure in retinal degeneration associated with mutations in the peripherin/RDS gene. Investigative ophthalmology & visual science. 2011 Mar 1;52(3):1557-66.

Duncan JL, Zhang Y, Gandhi J, Nakanishi C, Othman M, Branham KE, Swaroop A, Roorda A. High-resolution imaging with adaptive optics in patients with inherited retinal degeneration. Investigative ophthalmology & visual science. 2007 Jul 1;48(7):3283-91.

Duncan JL, Pierce EA, Laster AM, Daiger SP, Birch DG, Ash JD, Iannaccone A, Flannery JG, Sahel JA, Zack DJ, Zarbin MA. Inherited retinal degenerations: current landscape and knowledge gaps. Translational vision science & technology. 2018 Jul 1;7(4):6.

Duncker T, Greenberg JP, Ramachandran R, Hood DC, Smith RT, Hirose T, Woods RL, Tsang SH, Delori FC, Sparrow JR. Quantitative fundus autofluorescence and optical coherence tomography in best vitelliform macular dystrophy. Investigative ophthalmology & visual science. 2014 Mar 1;55(3):1471-82.

Duong TT, Vasireddy V, Ramachandran P, Herrera PS, Leo L, Merkel C, Bennett J, Mills JA. Use of induced pluripotent stem cell models to probe the pathogenesis of choroideremia and to develop a potential treatment. Stem cell research. 2018 Mar 1;27:140-50.

Edwards TL, Jolly JK, Groppe M, Barnard AR, Cottriall CL, Tolmachova T, Black GC, Webster AR, Lotery AJ, Holder GE, Xue K. Visual acuity after retinal gene therapy for choroideremia. New England Journal of Medicine. 2016 May 19;374(20):1996-8.

EyeGENE--National Ophthalmic Disease Genotyping Network. Insight 2009;34:27.

Ferris III FL, Kassoff A, Bresnick GH, Bailey I. New visual acuity charts for clinical research. American journal of ophthalmology. 1982 Jul 1;94(1):91-6.

Fishman GA, Gilbert LD, Anderson RJ, Marmor MF, Weleber RG, Viana MA. Effect of methazolamide on chronic macular edema in patients with retinitis pigmentosa. Ophthalmology 1994;101:687-693.

Fishman GA, Jacobson SG, Alexander KR, Cideciyan AV, Birch DG, Weleber RG, Hood DC. Outcome measures and their application in clinical trials for retinal degenerative diseases: outline, review, and perspective. Retina. 2005 Sep 1;25(6):772-7.

Foote KG, De la Huerta I, Gustafson K, Baldwin A, Zayit-Soudry S, Rinella N, Porco TC, Roorda A, Duncan JL. Cone spacing correlates with retinal thickness and microperimetry in patients with inherited retinal degenerations. Investigative ophthalmology & visual science. 2019 Mar 1;60(4):1234-43.

Foote KG, Loumou P, Griffin S, Qin J, Ratnam K, Porco TC, Roorda A, Duncan JL. Relationship between foveal cone structure and visual acuity measured with adaptive optics scanning laser ophthalmoscopy in retinal degeneration. Investigative ophthalmology & visual science. 2018 Jul 2;59(8):3385-93.

Gao B, Wenzel A, Grimm C, Vavricka SR, Benke D, Meier PJ, Reme CE. Localization of organic anion transport protein 2 in the apical region of rat retinal pigment epithelium. Investigative ophthalmology & visual science. 2002 Feb 1;43(2):510-4.

Gao SS, Jia Y, Zhang M, Su JP, Liu G, Hwang TS, Bailey ST, Huang D. Optical coherence tomography angiography. Investigative ophthalmology & visual science. 2016 Jul 1;57(9):OCT27-36.

Gao SS, Patel RC, Jain N, Zhang M, Weleber RG, Huang D, Pennesi ME, Jia Y. Choriocapillaris evaluation in choroideremia using optical coherence tomography angiography. Biomedical optics express. 2017 Jan 1;8(1):48-56.

García-Pérez MA. Forced-choice staircases with fixed step sizes: asymptotic and small-sample properties. Vision research. 1998 Jun 1;38(12):1861-81.

Geller AM, Sieving PA, Green DG. Effect on grating identification of sampling with degenerate arrays. JOSA A. 1992 Mar 1;9(3):472-7.

Goetz KE, Reeves MJ, Tumminia SJ, Brooks BP. eyeGENE (R): a novel approach to combine clinical testing and researching genetic ocular disease. Current opinion in ophthalmology. 2012 Sep;23(5):355.

Greenstein VC, Nunez J, Lee W, Schuerch K, Fortune B, Tsang SH, Allikmets R, Sparrow JR, Hood DC. A comparison of en face optical coherence tomography and fundus autofluorescence in Stargardt disease. Investigative ophthalmology & visual science. 2017 Oct 1;58(12):5227-36.

Grover S, Fishman GA, Gilbert LD, Anderson RJ. Reproducibility of visual acuity measurements in patients with retinitis pigmentosa. Retina 1997;17:33-37.

Grunwald JE, Maguire AM, Dupont J. Retinal hemodynamics in retinitis pigmentosa. American journal of ophthalmology. 1996 Oct 1;122(4):502-8.

Hariri AH, Velaga SB, Girach A, Ip MS, Le PV, Lam BL, Fischer MD, Sankila EM, Pennesi ME, Holz FG, MacLaren RE. Measurement and reproducibility of preserved ellipsoid zone area and preserved retinal pigment epithelium area in eyes with choroideremia. American journal of ophthalmology. 2017 Jul 1;179:110-7.

Harmening WM, Tuten WS, Roorda A, Sincich LC. Mapping the perceptual grain of the human retina. Journal of Neuroscience. 2014 Apr 16;34(16):5667-77.

Hartong DT, Berson EL, Dryja TP. Retinitis pigmentosa. Lancet 2006;368:1795-1809.

Helmholtz HV. Helmholtz's Treatise on Physiological Optics: Translated from the 3d German Ed. Optical Society of America; 1924.

Hirota M, Morimoto T, Kanda H, Lohmann TK, Miyagawa S, Endo T, Miyoshi T, Fujikado T. Relationships between spatial contrast sensitivity and parafoveal cone density in normal subjects and patients with retinal degeneration. Ophthalmic Surgery, Lasers and Imaging Retina. 2017 Feb 14;48(2):106-13.

Hohman TC. Hereditary retinal dystrophy. Handbook of Experimental Pharmacology 2017;242:337–367.

Hood DC, Cho J, Raza AS, Dale EA, Wang M. Reliability of a computer-aided manual procedure for segmenting optical coherence tomography scans. Optometry and vision science: official publication of the American Academy of Optometry. 2011 Jan;88(1):113.

Hood DC, Lazow MA, Locke KG, Greenstein VC, Birch DG. The transition zone between healthy and diseased retina in patients with retinitis pigmentosa. Investigative ophthalmology & visual science. 2011 Jan 1;52(1):101-8.

Hood DC, Lin CE, Lazow MA, Locke KG, Zhang X, Birch DG. Thickness of receptor and post-receptor retinal layers in patients with retinitis pigmentosa measured with frequency-domain optical coherence tomography. Investigative ophthalmology & visual science. 2009 May 1;50(5):2328-36.

Hood DC, Ramachandran R, Holopigian K, Lazow M, Birch DG, Greenstein VC. Method for deriving visual field boundaries from OCT scans of patients with retinitis pigmentosa. Biomedical optics express. 2011 May 1;2(5):1106-14.

Huang Y, Zhang Q, Thorell MR, An L, Durbin MK, Laron M, Sharma U, Gregori G, Rosenfeld PJ, Wang RK. Swept-source OCT angiography of the retinal vasculature using intensity differentiation-based optical microangiography algorithms. Ophthalmic Surgery, Lasers and Imaging Retina. 2014 Sep 22;45(5):382-9.

Hwang YH, Kim SW, Kim YY, Na JH, Kim HK, Sohn YH. Optic nerve head, retinal nerve fiber layer, and macular thickness measurements in young patients with retinitis pigmentosa. Current eye research. 2012 Oct 1;37(10):914-20.

Jacobson SG, Cideciyan AV, Ratnakaram R, Heon E, Schwartz SB, Roman AJ, Peden MC, Aleman TS, Boye SL, Sumaroka A, Conlon TJ. Gene therapy for leber congenital amaurosis caused by RPE65 mutations: safety and efficacy in 15 children and adults followed up to 3 years. Archives of ophthalmology. 2012 Jan 9;130(1):9-24.

Jacobson SG, Cideciyan AV, Sumaroka A, Aleman TS, Schwartz SB, Windsor EA, Roman AJ, Stone EM, MacDonald IM. Remodeling of the human retina in choroideremia: rab escort protein 1 (REP-1) mutations. Investigative ophthalmology & visual science. 2006 Sep 1;47(9):4113-20.

Jacobson SG, Voigt WJ, Parel JM, Apathy PP, Nghiem-Phu L, Myers SW, Patella VM. Automated light-and dark-adapted perimetry for evaluating retinitis pigmentosa. Ophthalmology. 1986 Dec 1;93(12):1604-11.

Jain N, Jia Y, Gao SS, Zhang X, Weleber RG, Huang D, Pennesi ME. Optical coherence tomography angiography in choroideremia: correlating choriocapillaris loss with overlying degeneration. JAMA ophthalmology. 2016 Jun 1;134(6):697-702.

Jia Y, Bailey ST, Hwang TS, McClintic SM, Gao SS, Pennesi ME, Flaxel CJ, Lauer AK, Wilson DJ, Hornegger J, Fujimoto JG. Quantitative optical coherence tomography angiography of vascular abnormalities in the living human eye. Proceedings of the National Academy of Sciences. 2015 May 5;112(18):E2395-402.

Jolly JK, Edwards TL, Moules J, Groppe M, Downes SM, MacLaren RE. A qualitative and quantitative assessment of fundus autofluorescence patterns in patients with choroideremia. Investigative ophthalmology & visual science. 2016 Aug 1;57(10):4498-503.

Kato M, Maruko I, Koizumi H, Iida T. Optical coherence tomography angiography and fundus autofluorescence in the eyes with choroideremia. BMJ case reports. 2017 Jan 6;2017:bcr2016217682.

Kim LS, McAnany JJ, Alexander KR, Fishman GA. Intersession repeatability of Humphrey perimetry measurements in patients with retinitis pigmentosa. Investigative ophthalmology & visual science. 2007 Oct 1;48(10):4720-4.

Kolb H. Gross anatomy of the eye. In Webvision: The Organization of the Retina and Visual System [Internet] 2007 May 1. University of Utah Health Sciences Center. Available from: https://www.ncbi.nlm.nih.gov/books/NBK11534/.

Kolb H. Photoreceptors. InWebvision: The Organization of the Retina and Visual System [Internet] 2012 Feb 28. University of Utah Health Sciences Center. Available from: https://www.ncbi.nlm.nih.gov/books/NBK11522/

Lamb TD. Why rods and cones? Eye. 2016 Feb;30(2):179.

Lazow MA, Hood DC, Ramachandran R, Burke TR, Wang YZ, Greenstein VC, Birch DG. Transition zones between healthy and diseased retina in choroideremia (CHM) and Stargardt disease (STGD) as compared to retinitis pigmentosa (RP). Investigative ophthalmology & visual science. 2011 Dec 1;52(13):9581-90.

Léveillard T, Mohand-Saïd S, Lorentz O, Hicks D, Fintz AC, Clérin E, Simonutti M, Forster V, Cavusoglu N, Chalmel F, Dollé P. Identification and characterization of rod-derived cone viability factor. Nature genetics. 2004 Jul;36(7):755.

Liang J, Williams DR. Aberrations and retinal image quality of the normal human eye. JOSA A. 1997 Nov 1;14(11):2873-83.

Lindberg CR, Fishman GA, Anderson RJ, Vasquez V. Contrast sensitivity in retinitis pigmentosa. British Journal of Ophthalmology. 1981 Dec 1;65(12):855-8.

Litts KM, Cooper RF, Duncan JL, Carroll J. Photoreceptor-based biomarkers in AOSLO retinal imaging. Investigative ophthalmology & visual science. 2017 May 1;58(6):BIO255-67.

MacDonald IM, Hume S, Chan S, Seabra MC. Choroideremia. InGeneReviews ® 2015 Feb 26. University of Washington, Seattle. Available at: www.ncbi.nlm.nih.gov/books/NBK1337

MacLaren RE, Groppe M, Barnard AR, Cottriall CL, Tolmachova T, Seymour L, Clark KR, During MJ, Cremers FP, Black GC, Lotery AJ. Retinal gene therapy in patients with choroideremia: initial findings from a phase 1/2 clinical trial. The Lancet. 2014 Mar 29;383(9923):1129-37.

Makiyama Y, Ooto S, Hangai M, Takayama K, Uji A, Oishi A, Ogino K, Nakagawa S, Yoshimura N. Macular cone abnormalities in retinitis pigmentosa with preserved central vision using adaptive optics scanning laser ophthalmoscopy. PLoS One. 2013 Nov 19;8(11):e79447.

Marcos S, Sawides L, Gambra E, Dorronsoro C. Influence of adaptive-optics ocular aberration correction on visual acuity at different luminances and contrast polarities. Journal of vision. 2008 Oct 1;8(13):1.

McLaughlin ME, Sandberg MA, Berson EL, Dryja TP. Recessive mutations in the gene encoding the β–subunit of rod phosphodiesterase in patients with retinitis pigmentosa. Nature genetics. 1993 Jun;4(2):130.

Menghini M, Lujan BJ, Zayit-Soudry S, Syed R, Porco TC, Bayabo K, Carroll J, Roorda A, Duncan JL. Correlation of outer nuclear layer thickness with cone density values in patients with retinitis pigmentosa and healthy subjects. Investigative ophthalmology & visual science. 2014 1;56(1):372-81.

Milam AH, Li ZY, Fariss RN. Histopathology of the human retina in retinitis pigmentosa. Progress in retinal and eye research. 1998 Apr;17(2):175-205.

Miller DT, Williams DR, Morris GM, Liang J. Images of cone photoreceptors in the living human eye. Vision research. 1996 Apr 1;36(8):1067-79.

Morgan JI, Han G, Klinman E, Maguire WM, Chung DC, Maguire AM, Bennett J. High-resolution adaptive optics retinal imaging of cellular structure in choroideremia. Investigative ophthalmology & visual science. 2014 Oct 1;55(10):6381-97.

Morgan JI, Tuten WS, Cooper RF, Han GK, Young G, Bennett J, Maguire AM, Aleman TS, Brainard DH. Cellular-scale assessment of visual function in Choroideremia. Investigative Ophthalmology & Visual Science. 2018 Jul 13;59(9):1151-.

Paavo M, Lee W, Sengillo J, Tsang SH, Sparrow JR. Near-infrared Autofluoresence Imaging in Choroideremia. Investigative Ophthalmology & Visual Science. 2018 Jul 13;59(9):4664.

Padnick-Silver L, Derwent JJ, iuliano E, Narfström K, Linsenmeier RA. Retinal oxygenation and oxygen metabolism in Abyssinian cats with a hereditary retinal degeneration. Investigative ophthalmology & visual science. 2006 Aug 1;47(8):3683-9.

Penn JS, Li S, Naash MI. Ambient hypoxia reverses retinal vascular attenuation in a transgenic mouse model of autosomal dominant retinitis pigmentosa. Investigative ophthalmology & visual science. 2000 Nov 1;41(12):4007-13.

Pfau M, Lindner M, Fleckenstein M, Finger RP, Rubin GS, Harmening WM, Morales MU, Holz FG, Schmitz-Valckenberg S. Test-retest reliability of scotopic and mesopic fundus-controlled perimetry using a modified MAIA (macular integrity assessment) in normal eyes. Ophthalmologica. 2017;237(1):42-54.

Pfau M, Lindner M, Müller PL, Birtel J, Finger RP, Harmening WM, Fleckenstein M, Holz FG, Schmitz-Valckenberg S. Effective dynamic range and retest reliability of dark-adapted two-color fundus-controlled perimetry in patients with macular diseases. Investigative ophthalmology & visual science. 2017 May 1;58(6):BIO158-67.

PLEX Elite 9000 User Manual. Instructions for Use. Dublin, CA, USA: Carl Zeiss Meditec; 2016.

Podoleanu AG, Rosen RB. Combinations of techniques in imaging the retina with high resolution. Progress in retinal and eye research. 2008 Jul 1;27(4):464-99.

Poonja S, Patel S, Henry L, Roorda A. Dynamic visual stimulus presentation in an adaptive optics scanning laser ophthalmoscope. Journal of refractive surgery. 2005 Sep 2;21(5):S575-80.

Rajagopalan AS, Shahidi M, Alexander KR, Fishman GA, Zelkha R. Higher-order wavefront aberrations in retinitis pigmentosa. Optometry and vision science. 2005 Jul 1;82(7):623-8.

Rangaswamy NV, Patel HM, Locke KG, Hood DC, Birch DG. A comparison of visual field sensitivity to photoreceptor thickness in retinitis pigmentosa. Investigative ophthalmology & visual science. 2010 Aug 1;51(8):4213-9.

Ratnam K, Carroll J, Porco TC, Duncan JL, Roorda A. Relationship between foveal cone structure and clinical measures of visual function in patients with inherited retinal degenerations. Investigative ophthalmology & visual science. 2013 Aug 1;54(8):5836-47.

Ratnam K, Domdei N, Harmening WM, Roorda A. Benefits of retinal image motion at the limits of spatial vision. Journal of vision. 2017 Jan 1;17(1):30.

Ratnam K, Västinsalo H, Roorda A, Sankila EM, Duncan JL. Cone structure in patients with Usher syndrome type III and mutations in the Clarin 1 gene. JAMA ophthalmology. 2013 Jan 1;131(1):67-74.

Ripps H. Cell death in retinitis pigmentosa: gap junctions and the 'bystander'effect. Experimental eye research. 2002 Mar 1;74(3):327-36.

Robson AG, Michaelides M, Saihan Z, Bird AC, Webster AR, Moore AT, Fitzke FW, Holder GE. Functional characteristics of patients with retinal dystrophy that manifest abnormal parafoveal annuli of high density fundus autofluorescence; a review and update. Documenta Ophthalmologica. 2008 Mar 1;116(2):79-89.

Rodieck RW. The density recovery profile: a method for the analysis of points in the plane applicable to retinal studies. Visual neuroscience. 1991 Feb;6(2):95-111.

Roorda A, Duncan JL. Adaptive optics ophthalmoscopy. Annual review of vision science. 2015 Nov 24;1:19-50.

Roorda A, Romero-Borja F, Donnelly III WJ, Queener H, Hebert TJ, Campbell MC. Adaptive optics scanning laser ophthalmoscopy. Optics express. 2002 May 6;10(9):405-12.

Ross DF, Fishman GA, Gilbert LD, Anderson RJ. Variability of visual field measurements in normal subjects and patients with retinitis pigmentosa. Archives of Ophthalmology. 1984 Jul 1;102(7):1004-10.

Rossi EA, Roorda A. Is visual resolution after adaptive optics correction susceptible to perceptual learning?. Journal of vision. 2010 Oct 1;10(12):11.

Rossi EA, Roorda A. The relationship between visual resolution and cone spacing in the human fovea. Nature neuroscience. 2010 Feb;13(2):156.

Rossi EA, Weiser P, Tarrant J, Roorda A. Visual performance in emmetropia and low myopia after correction of high-order aberrations. Journal of vision. 2007 May 1;7(8):1-.

Rucci M, Iovin R, Poletti M, Santini F. Miniature eye movements enhance fine spatial detail. Nature 2007;447:851-854.

Russell S, Bennett J, Wellman JA, Chung DC, Yu ZF, Tillman A, Wittes J, Pappas J, Elci O, McCague S, Cross D. Efficacy and safety of voretigene neparvovec (AAV2-hRPE65v2) in patients with RPE65-mediated inherited retinal dystrophy: a randomised, controlled, open-label, phase 3 trial. The Lancet. 2017 Aug 26;390(10097):849-60.

Sandberg MA, Rosner B, Weigel-DiFranco C, McGee TL, Dryja TP, Berson EL. Disease course in patients with autosomal recessive retinitis pigmentosa due to the USH2A gene. Investigative ophthalmology & visual science. 2008 Dec 1;49(12):5532-9.

Sahel JA, Marazova K, Audo I. Clinical characteristics and current therapies for inherited retinal degenerations. Cold Spring Harbor perspectives in medicine. 2015 Feb 1;5(2):a017111.

Schmidt BP, Boehm AE, Foote KG, Roorda A. The spectral identity of foveal cones is preserved in hue perception. Journal of vision. 2018 Oct 1;18(11):19.

Schmitz-Valckenberg S, Holz FG, Bird AC, Spaide RF. Fundus autofluorescence imaging: review and perspectives. Retina. 2008 Mar 1;28(3):385-409.

Scoles D, Sulai YN, Cooper RF, Higgins BP, Johnson RD, Carroll J, Dubra A, Stepien KE. Photoreceptor inner segment morphology in best vitelliform macular dystrophy. Retina (Philadelphia, Pa.). 2017 Apr;37(4):741.

Scoles D, Sulai YN, Langlo CS, Fishman GA, Curcio CA, Carroll J, Dubra A. In vivo imaging of human cone photoreceptor inner segments. Investigative ophthalmology & visual science. 2014 Jul 1;55(7):4244-51.

Seiple W, Clemens CJ, Greenstein VC, Carr RE, Holopigian K. Test–retest reliability of the multifocal electroretinogram and humphrey visual fields in patients with retinitis pigmentosa. Documenta ophthalmologica. 2004 Nov 1;109(3):255-72.

Sparrow JR, Gregory-Roberts E, Yamamoto K, Blonska A, Ghosh SK, Ueda K, Zhou J. The bisretinoids of retinal pigment epithelium. Progress in retinal and eye research. 2012 Mar 1;31(2):121-35.

Sparrow JR. Light Come Shining: Fundus Autofluorescence. Journal of pediatric ophthalmology and strabismus. 2018 Sep 20;55(5):285-6.

Springer C, Bultmann S, Volcker HE, Rohrschneider K. Fundus perimetry with the Micro Perimeter 1 in normal individuals: comparison with conventional threshold perimetry. Ophthalmology 2005;112:848-854.

Stone JL, Barlow WE, Humayun MS, de Juan E, Milam AH. Morphometric analysis of macular photoreceptors and ganglion cells in retinas with retinitis pigmentosa. Archives of Ophthalmology. 1992 Nov 1;110(11):1634-9.

Sullivan LS, Bowne SJ, Reeves MJ, Blain D, Goetz K, NDifor V, Vitez S, Wang X, Tumminia SJ, Daiger SP. Prevalence of mutations in eyeGENE probands with a diagnosis of autosomal dominant retinitis pigmentosa. Investigative ophthalmology & visual science. 2013 Sep 1;54(9):6255-61.

Sun LW, Johnson RD, Langlo CS, Cooper RF, Razeen MM, Russillo MC, Dubra A, Connor TB, Han DP, Pennesi ME, Kay CN. Assessing photoreceptor structure in retinitis pigmentosa and Usher syndrome. Investigative ophthalmology & visual science. 2016 May 1;57(6):2428-42.

Sun LW, Johnson RD, Williams V, Summerfelt P, Dubra A, Weinberg DV, Stepien KE, Fishman GA, Carroll J. Multimodal imaging of photoreceptor structure in choroideremia. PloS one. 2016 Dec 9;11(12):e0167526.

Sundaram V, Wilde C, Aboshiha J, Cowing J, Han C, Langlo CS, Chana R, Davidson AE, Sergouniotis PI, Bainbridge JW, Ali RR. Retinal structure and function in achromatopsia: implications for gene therapy. Ophthalmology. 2014 Jan 1;121(1):234-45.

Sung CH, Davenport CM, Nathans J. Rhodopsin mutations responsible for autosomal dominant retinitis pigmentosa. Clustering of functional classes along the polypeptide chain. Journal of Biological Chemistry. 1993 Dec 15;268(35):26645-9.

Syed R, Sundquist SM, Ratnam K, Zayit-Soudry S, Zhang Y, Crawford JB, MacDonald IM, Godara P, Rha J, Carroll J, Roorda A. High-resolution images of retinal structure in patients with choroideremia. Investigative ophthalmology & visual science. 2013 Feb 1;54(2):950-61.

Szamier RB. Ultrastructure of the preretinal membrane in retinitis pigmentosa. Investigative ophthalmology & visual science. 1981 Aug 1;21(2):227-36.

Talcott KE, Ratnam K, Sundquist SM, Lucero AS, Lujan BJ, Tao W, Porco TC, Roorda A, Duncan JL. Longitudinal study of cone photoreceptors during retinal degeneration and in response to ciliary neurotrophic factor treatment. Investigative ophthalmology & visual science. 2011 Apr 1;52(5):2219-26.

Tee JJ, Smith AJ, Hardcastle AJ, Michaelides M. RPGR-associated retinopathy: clinical features, molecular genetics, animal models and therapeutic options. British Journal of Ophthalmology. 2016 Aug 1;100(8):1022-7.

Tu JH, Foote KG, Lujan BJ, Ratnam K, Qin J, Gorin MB, Cunningham Jr ET, Tuten WS, Duncan JL, Roorda A. Dysflective cones: visual function and cone reflectivity in long-term follow-up of acute bilateral foveolitis. American journal of ophthalmology case reports. 2017 Sep 1;7:14-9.

Tucker BA, Scheetz TE, Mullins RF, DeLuca AP, Hoffmann JM, Johnston RM, Jacobson SG, Sheffield VC, Stone EM. Exome sequencing and analysis of induced pluripotent stem cells identify the cilia-related gene male germ cell-associated kinase (MAK) as a cause of retinitis pigmentosa. Proceedings of the National Academy of Sciences. 2011 Aug 23;108(34):E569-76.

Tuten WS, Tiruveedhula P, Roorda A. Adaptive optics scanning laser ophthalmoscope-based microperimetry. Optometry and Vision Science. 2012 May;89(5):563.

Tuten WS, Vergilio GK, Young GJ, Bennett J, Maguire AM, Aleman TS, Brainard DH, Morgan JI. Visual function at the atrophic border in choroideremia assessed with adaptive optics microperimetry. Ophthalmology Retina. 2019 May 8.

Vanden Bosch ME, Wall M. Visual acuity scored by the letter-by-letter or probit methods has lower retest variability than the line assignment method. Eye. 1997 May;11(3):411.

Verbakel SK, van Huet RA, Boon CJ, den Hollander AI, Collin RW, Klaver CC, Hoyng CB, Roepman R, Klevering BJ. Non-syndromic retinitis pigmentosa. Progress in Retinal and Eye Research. 2018 Sep 1;66:157-86.

Wang DY, Chan WM, Tam PO, Baum L, Lam DS, Chong KK, Fan BJ, Pang CP. Gene mutations in retinitis pigmentosa and their clinical implications. Clinica Chimica Acta. 2005 Jan 1;351(1-2):5-16.

Wang F, Wang H, Tuan HF, Nguyen DH, Sun V, Keser V, Bowne SJ, Sullivan LS, Luo H, Zhao L, Wang X. Next generation sequencing-based molecular diagnosis of retinitis pigmentosa: identification of a novel genotype-phenotype correlation and clinical refinements. Human genetics. 2014 Mar 1;133(3):331-45.

Wang Q, Tuten WS, Lujan BJ, Holland J, Bernstein PS, Schwartz SD, Duncan JL, Roorda A. Adaptive optics microperimetry and OCT images show preserved function and recovery of cone visibility in macular telangiectasia type 2 retinal lesions. Investigative ophthalmology & visual science. 2015 Feb 1;56(2):778-86.

Watson AB, Pelli DG. QUEST: A Bayesian adaptive psychometric method. Perception & psychophysics. 1983 Mar 1;33(2):113-20.

Weinberger AW, Lappas A, Kirschkamp T, Mazinani BA, Huth JK, Mohammadi B, Walter P. Fundus near infrared fluorescence correlates with fundus near infrared reflectance. Investigative ophthalmology & visual science. 2006 Jul 1;47(7):3098-108.

Weleber RG, Pennesi ME, Wilson DJ, Kaushal S, Erker LR, Jensen L, McBride MT, Flotte TR, Humphries M, Calcedo R, Hauswirth WW. Results at 2 years after gene therapy for RPE65-deficient Leber congenital amaurosis and severe early-childhood–onset retinal dystrophy. Ophthalmology. 2016 Jul 1;123(7):1606-20.

Wen Y, Klein M, Hood DC, Birch DG. Relationships among multifocal electroretinogram amplitude, visual field sensitivity, and SD-OCT receptor layer thicknesses in patients with retinitis pigmentosa. Investigative ophthalmology & visual science. 2012 Feb 1;53(2):833-40.

Wen Y, Locke KG, Klein M, Bowne SJ, Sullivan LS, Ray JW, Daiger SP, Birch DG, Hughbanks-Wheaton DK. Phenotypic characterization of 3 families with autosomal dominant retinitis pigmentosa due to mutations in KLHL7. Archives of ophthalmology. 2011 Nov 10;129(11):1475-82.

Wilk MA, McAllister JT, Cooper RF, Dubis AM, Patitucci TN, Summerfelt P, Anderson JL, Stepien KE, Costakos DM, Connor TB, Wirostko WJ. Relationship between foveal cone specialization and pit morphology in albinism. Investigative ophthalmology & visual science. 2014 Jul 1;55(7):4186-98.

Wilk MA, Wilk BM, Langlo CS, Cooper RF, Carroll J. Evaluating outer segment length as a surrogate measure of peak foveal cone density. Vision research. 2017 Jan 1;130:57-66.

Wolf G. The visual cycle of the cone photoreceptors of the retina. Nutrition reviews. 2004 Jul 1;62(7):283.

Wolfing JI, Chung M, Carroll J, Roorda A, Williams DR. High-resolution retinal imaging of cone–rod dystrophy. Ophthalmology. 2006 Jun 1;113(6):1014-9.

Wolkstein M, Atkin A, Bodis-Wollner I. Contrast sensitivity in retinal disease. Ophthalmology. 1980 Nov 1;87(11):1140-9.

Wong EN, Mackey DA, Morgan WH, Chen FK. Inter-device comparison of retinal sensitivity measurements: the CenterVue MAIA and the Nidek MP-1. Clinical & experimental ophthalmology. 2016 Jan;44(1):15-23.

Wright AF, Chakarova CF, El-Aziz MM, Bhattacharya SS. Photoreceptor degeneration: genetic and mechanistic dissection of a complex trait. Nature Reviews Genetics. 2010 Apr;11(4):273. y Cajal, SR. The structure of the retina. Translated by SA Thorpe and M. Glickstein. CC Thomas, Springfield, Illinois. 1972. (https://nei.nih.gov/intramural/lrcmb/LRCMB_image)

Yoon GY, Williams DR. Visual performance after correcting the monochromatic and chromatic aberrations of the eye. JOSA A. 2002 Feb 1;19(2):266-75.

Yu DY, Cringle SJ. Retinal degeneration and local oxygen metabolism. Experimental eye research. 2005 Jun 1;80(6):745-51.

Zayit-Soudry S, Sippl-Swezey N, Porco TC, Lynch SK, Syed R, Ratnam K, Menghini M, Roorda AJ, Duncan JL. Repeatability of cone spacing measures in eyes with inherited retinal degenerations. Investigative ophthalmology & visual science. 2015 Sep 1;56(10):6179-89.

Zhang AY, Mysore N, Vali H, Koenekoop J, Cao SN, Li S, Ren H, Keser V, Lopez-Solache I, Siddiqui SN, Khan A. Choroideremia is a systemic disease with lymphocyte crystals and plasma lipid and RBC membrane abnormalities. Investigative ophthalmology & visual science. 2015 Dec 1;56(13):8158-65.

Zhang Y, Roorda A. Evaluating the lateral resolution of the adaptive optics scanning laser ophthalmoscope. Journal of biomedical optics. 2006 Jan;11(1):014002.

Zhang Q, Chen CL, Chu Z, Zheng F, Miller A, Roisman L, de Oliveira Dias JR, Yehoshua Z, Schaal KB, Feuer W, Gregori G. Automated quantitation of choroidal neovascularization: a comparison study between spectral-domain and swept-source OCT angiograms. Investigative ophthalmology & visual science. 2017 Mar 1;58(3):1506-13.

Zhang Q, Zheng F, Motulsky EH, Gregori G, Chu Z, Chen CL, Li C, De Sisternes L, Durbin M, Rosenfeld PJ, Wang RK. A novel strategy for quantifying choriocapillaris flow voids using swept-source OCT angiography. Investigative ophthalmology & visual science. 2018 Jan 1;59(1):203-11.

Zhang Q. Retinitis pigmentosa: progress and perspective. The Asia-Pacific Journal of Ophthalmology. 2016 Jul 1;5(4):265-71.